Wegener Center for Climate and Global Change
University of Graz

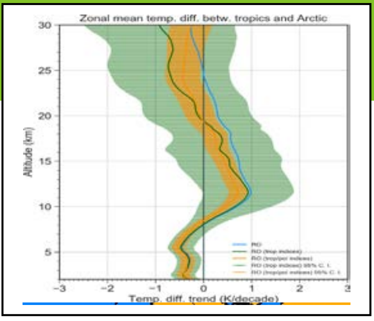

**Scientific Report No. 82-2019**

# Arctic amplification in atmospheric observations – Equator-to-pole gradients and their connection to storm tracks

Patrick Peter

June 2019

The **Wegener Center for Climate and Global Change** combines as an interdisciplinary, internationally oriented research institute the competences of the University of Graz in the research area “Climate, Environmental and Global Change”. It brings together, in a dedicated building close to the University central campus, research teams and scientists from fields such as geo- and climate physics, meteorology, economics, geography, and regional sciences. At the same time close links exist and are further developed with many cooperation partners, both nationally and internationally. The research interests extend from monitoring, analysis, modeling and prediction of climate and environmental change via climate impact research to the analysis of the human dimensions of these changes, i.e, the role of humans in causing and being effected by climate and environmental change as well as in adaptation and mitigation. (more informationen at www.wegcenter.at)

The present report is the result of a Master thesis work completed in June 2019. The work was funded by the Austrian Science Fund (FWF) under research grant P27724-NBL (VERTICLIM project).

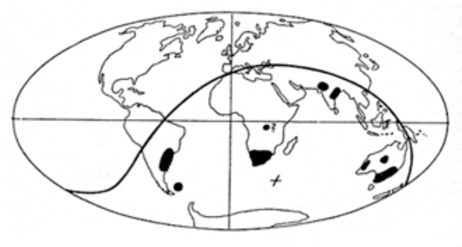

**Alfred Wegener** (1880–1930), after whom the Wegener Center is named, was founding holder of the University of Graz Geophysics Chair (1924-1930). In his work in the fields of geophysics, meteorology, and climatology he was a brilliant scientist and scholar, thinking and acting in an interdisciplinary way, far ahead of his time with this style. The way of his ground-breaking research on continental drift is a shining role model – his sketch on the relations of continents based on traces of an ice age about 300 million years ago (left) as basis for the Wegener Center Logo is thus a continuous encouragement to explore equally innovative ways:
*paths emerge in that we walk them* (Motto of the Wegener Center).

Wegener Center Verlag • Graz, Austria
© 2019 All Rights Reserved.
Selected use of individual figures, tables or parts of text is permitted for non-commercial purposes, provided this report is correctly and clearly cited as the source. Publisher contact for any interests beyond such use: wegcenter@uni-graz.at.

ISBN 978-3-9504717-1-7

June 2019

*Contact: MSc BSc Patrick Peter*
*p.peter@elab.co.at*

Wegener Center for Climate and Global Change
University of Graz
Brandhofgasse 5
A-8010 Graz, Austria
www.wegcenter.at

Master thesis
to obtain the degree Master of Sciences
at the University of Graz

# Arctic amplification in atmospheric observations – Equator-to-pole gradients and their connection to storm tracks

PETER Patrick, BSc

April 11, 2019

Supervisor
**Assoc. Prof. Mag. Dr. Andrea K. Steiner**
University of Graz, Austria

Co-Supervisor
**Mag. Dr. Florian Ladstädter**
Wegener Center for Climate and Global Change, Austria

# Abstract

Temperature changes in the Arctic region are crucial for the Earth's climate system. They affect the temperature gradient between the Equator and the Arctic region and subsequently influence the cyclone paths in the middle latitudes. This has a strong impact on the weather conditions in Europe and North America and could lead to more extreme weather events across the northern hemisphere.

To investigate these temperature changes and their consequences, Equator-to-pole temperature gradients as well as temperature differences and trends between the tropical area and the Arctic region are evaluated. As many storms move across the Atlantic, this region is investigated separately. In addition, two exemplary storm cases are explored. All results are based on atmospheric profiles from GPS Radio Occultation (RO) observations from 2001 to 2017. Atmospheric analyses and reanalyses are used for comparison. The high vertical resolution of the RO data offers a great advantage, as it allows the representation of vertical resolved trends from the troposphere up to the mid stratosphere.

In the lower troposphere, the temperature difference between the tropics and the Arctic decreases up to $-0.5\,\mathrm{K}$ per decade, while it increases above by up to $1\,\mathrm{K}$ per decade near $12\,\mathrm{km}$ altitude. In the lower stratosphere the temperature difference decreases up to $-0.4\,\mathrm{K}$ per decade at about $25\,\mathrm{km}$.

In the Atlantic region, the temperature difference is near zero in the lower troposphere. It increases above $8\,\mathrm{km}$ and decreases in the lower stratosphere with a maximum of $-1.5\,\mathrm{K}$ per decade. Overall, the temperature changes are found to be larger in the Arctic region than in the tropics.

With the current RO satellite constellations, it is found challenging to detect storm paths of small, fast moving storm systems. However, for large storm systems requiring less spatial-temporal resolution, the precise vertical geolocation with RO can provide additional information on the storm track on isentropic surfaces.

# Zusammenfassung

Temperaturänderungen in der Arktis sind für das Klimasystem der Erde von entscheidender Bedeutung. Sie beeinflussen den Temperaturunterschied zwischen der Arktis und dem Äquator und haben in weiterer Folge auch einen Einfluss auf die Stürme in mittleren Breiten. Eine Veränderung der Sturmbahnen wiederum kann Auswirkungen auf das Klima in Europa und Nordamerika haben und zu Wetterextremen in der Nordhemisphäre führen.

Um diese Temperaturänderungen und ihre Folgen besser beurteilen zu können werden sowohl Temperaturgradienten vom Äquator zu den Polen als auch die Temperaturunterschiede und Trends zwischen der tropischen und der arktischen Region genauer untersucht. Da viele Sturmbahnen über den Atlantik verlaufen, wird diese Region separat behandelt. Weiters werden zwei Sturmereignisse explizit betrachtet. Alle Ergebnisse basieren auf atmosphärischen Profilen von GPS Radio Okkultationsbeobachtungen zwischen 2001 und 2017. Zum Vergleich werden atmosphärische Analysen und Reanalysen verwendet. Die hohe vertikale Auflösung der Radio Okkultationsdaten ist von großem Vorteil, da sie die Darstellung vertikal aufgelöster Trends von der Troposphäre bis zur mittleren Stratosphäre ermöglicht.

In der unteren Troposphäre nimmt der Temperaturunterschied zwischen den Tropen und der Arktis um bis zu $-0.5\,\mathrm{K}$ pro Dekade ab, während er in der Nähe von $12\,\mathrm{km}$ bis zu $1\,\mathrm{K}$ pro Dekade ansteigt. In der unteren Stratosphäre bei etwa $25\,\mathrm{km}$ Höhe nimmt die Temperaturdifferenz mit ungefähr $-0.4\,\mathrm{K}$ pro Dekade ab.

In der Atlantikregion ist der Temperaturunterschied in der unteren Troposphäre nahe Null. Über $8\,\mathrm{km}$ wird der Temperaturunterschied größer, in der unteren Stratosphäre nimmt er jedoch mit einem Maximum von $-1.5\,\mathrm{K}$ pro Dekade wieder ab. Insgesamt sind die Temperaturschwankungen in der Arktis stärker als in den Tropen.

Mit den derzeitigen RO-Satellitenkonstellationen ist es schwierig, Sturmbahnen von kleinen, sich schnell bewegenden Sturmsystemen zu erkennen. Bei großen Sturmsystemen, die eine geringere zeitliche und räumliche Auflösung erfordern, kann die genaue vertikale Geolokalisierung mit RO zusätzliche Informationen über den Sturmverlauf auf isentropischen Oberflächen liefern.

# Acknowledgments

First and foremost, I would like to thank my supervisor Assoc. Prof. Mag. Dr. Andrea Steiner for giving me the opportunity to write this thesis at the Wegener Center for Climate and Global Change (WEGC) and for her time and valuable advice during the work.

Sincere thanks to Florian Ladstädter for his time and expertise whenever needed and for the thankless task of proofreading this thesis. He was a constant source of motivation and I really appreciate that he puts so much time and effort into sharing his knowledge.

I particularly thank all the people at the WEGC especially those in the ARSCliSys research group for their support and assistance. A special thanks to Hallgeir Wilhelmsen for various programming tips and some inspiring discussions. Further thanks go to Lukas Brunner who provided the LaTeX framework used for this thesis. Honest thanks to my office-mates Veronika, Matthias, Christoph and Martin for the enjoyable and fun work atmosphere.

The WEGC institute provided an excellent infrastructure to make this thesis possible and I also want to express my gratitude for the financial support. I extend my thanks to UCAR (Boulder, CO, USA) and ECMWF (Reading, UK) who generously provided the data used in this thesis. This work was written using the free software LaTeX and all programming and most of the plots in this thesis were done with the free and open source software Python. I hereby acknowledge all the contributors to these software packages.

I want to take this opportunity to also acknowledge four important friends in my life. Sincere thanks to Christoph Kreiner, Hannes Schwingenschlögl, Michael Hehenberger and Reinhard Steiner for the great time we spent together and for some exciting trips we made. You guys inspire me every day.

Most of all, I would like to express sincere thanks to my family. Apart from their financial support these past years, they have always encouraged me to choose my own path, never pushing me unduly, but rather reminding me to do what is best for me. Thank you all so very much for your patience of all the choices I made in life, allowing me to be the most well-rounded person I can be. Finally, I thank my girlfriend Tabea for always being there for me and supporting in everything I do.

# Contents

**1. Introduction 1**

**2. Characteristics of the Earth's atmosphere 5**
- 2.1. Vertical structure . . . . . . . . . . . . . . . . . . . . . . . . . . . 5
- 2.2. Arctic amplification . . . . . . . . . . . . . . . . . . . . . . . . . . 7
- 2.3. Storm tracks . . . . . . . . . . . . . . . . . . . . . . . . . . . . . 9
  - 2.3.1. What determines cyclones . . . . . . . . . . . . . . . . . . . . 9
  - 2.3.2. A closer look on baroclinic instability . . . . . . . . . . . . 11
  - 2.3.3. Parameters that define storm paths . . . . . . . . . . . . . . 13
- 2.4. Atmospheric variability . . . . . . . . . . . . . . . . . . . . . . . 15
  - 2.4.1. The Quasi-Biennial Oscillation . . . . . . . . . . . . . . . . . 15
  - 2.4.2. El Niño-Southern Oscillation . . . . . . . . . . . . . . . . . . 17
  - 2.4.3. Sudden Stratospheric Warming events . . . . . . . . . . . . . 20
- 2.5. Vertical coordinates . . . . . . . . . . . . . . . . . . . . . . . . . 22

**3. Data sets 25**
- 3.1. Radio Occultation data . . . . . . . . . . . . . . . . . . . . . . . . 25
- 3.2. Model data . . . . . . . . . . . . . . . . . . . . . . . . . . . . . . 28
  - 3.2.1. ECMWF analyses . . . . . . . . . . . . . . . . . . . . . . . . 29
  - 3.2.2. ERA-Interim . . . . . . . . . . . . . . . . . . . . . . . . . . . 29
- 3.3. Data preprocessing . . . . . . . . . . . . . . . . . . . . . . . . . . 29
  - 3.3.1. Sampling error correction . . . . . . . . . . . . . . . . . . . . 30
  - 3.3.2. Preparation for the temperature difference calculation . . . . 30
  - 3.3.3. Preparation for storm analysis . . . . . . . . . . . . . . . . . 30

**4. Methods 33**
- 4.1. The Equator to pole temperature gradient . . . . . . . . . . . . . . 33
- 4.2. Area average differencing method . . . . . . . . . . . . . . . . . . . 33
- 4.3. Isentropic surfaces . . . . . . . . . . . . . . . . . . . . . . . . . . 34
- 4.4. Multiple linear regression . . . . . . . . . . . . . . . . . . . . . . 35
  - 4.4.1. Generalized least squares model with auto regression . . . . . 35
  - 4.4.2. Regression including atmospheric variability indices . . . . . 37

**5. Results 39**
- 5.1. Vertical resolved gradients and differences between the tropics and the Arctic . . . . . . . . . . . . . . . . . . . . . . . . . . . . . . . 39
  - 5.1.1. Equator-to-pole temperature gradients . . . . . . . . . . . . . 39
  - 5.1.2. Temperature anomaly differences over time (2002-2017) . . . 43

5.2. Vertically resolved trends . . . . . . . . . . . . . . . . . . . . . . . . . 46
  5.2.1. Zonal mean temperature trends . . . . . . . . . . . . . . . . . . 46
  5.2.2. Temperature trends and difference trends in the Atlantic region 49
  5.2.3. Seasonal temperature trends . . . . . . . . . . . . . . . . . . . 53
  5.2.4. Trend in geopotential height . . . . . . . . . . . . . . . . . . . 54
5.3. Two examples of storm tracking with Radio Occultation . . . . . . . 61
  5.3.1. Extra-tropical cyclone Klaus . . . . . . . . . . . . . . . . . . . 61
  5.3.2. Tropical cyclone Haiyan . . . . . . . . . . . . . . . . . . . . . . 62

**6. Summary and conclusion** **67**

**Acronyms** **71**

**List of Figures** **73**

**Bibliography** **77**

**A. Temperature anomaly differences for ECMWF and ERAI** **91**

**B. Error analysis** **99**

**C. Storm tracks in ECMWF analyses in 6-hourly resolution** **119**

# 1. Introduction

The average global temperatures from 2000–2009 were about 0.6 °C higher than they were in the time period from 1951–1980. The Earth's north polar region, however, was about 2 °C warmer – a phenomenon known as Arctic amplification (Hansen et al. 2010; Cohen et al. 2014). The loss of sea ice is the main reason why the temperature has increased about twice as fast at the North Pole compared to other areas on the globe. Arctic amplification is connected to many weather steering phenomena in the mid-latitudes such as the jet stream and therefore has a massive impact on the Earth's climate system. Recent studies found that polar amplification has weakened the Equator-to-pole temperature gradient near the surface, while the temperature difference at higher altitudes has strengthened (Allen and Sherwood 2008; Harvey et al. 2014). The consequences of this variation are more noticeable each year. In winter 2018 the temperature at the North Pole was near the freezing point while strong frost was all over Northern Eurasia (Fig. 1.1). The polar vortex was completely disrupted, resulting in a massive Sudden Stratospheric Warming (SSW) event. The instability was amplified by ice reduction in the Barents-Kara-Sea, mostly caused by Arctic amplification (Kretschmer et al. 2016).

The climate change response of storm tracks has been the focus of a large number of studies in recent years and many climatologists think that the different warming rates of the North Pole and the Equator could have a significant impact on some types of cyclones (Yin 2005; Bengtsson et al. 2005; Ulbrich et al. 2009; Catto et al. 2011; Zappa et al. 2013). While storm path changes are relatively small on a global scale, regional changes can be much more substantial. Extra-tropical cyclones, for example, harvest energy from the atmosphere as warm and cold air masses interact along the polar front. When the temperature difference between the tropics and the poles decreases, there may be less energy for these storms to absorb. This could weaken the cyclones or make them less frequent (Schneider et al. 2010; Zappa et al. 2013; Woollings et al. 2016). However, there are still significant discrepancies in the predictions of current climate models on how the storm tracks will react to climate change (Harvey et al. 2014). While a poleward shift of the mid-latitude storm tracks in response to anthropogenic greenhouse-gas increase has been diagnosed in most of the future simulations, there are considerable regional variations from this. In particular the response in the North Atlantic instead often resembles a strengthening and extending of the path farther east on the southern flank towards Europe (Yin 2005; Ulbrich et al. 2009; IPCC 2014). Therefore, we can expect a rise in storminess across Europe (Pinto et al. 2007). In order to increase confidence in climate change projections, it is necessary to better understand the physical mechanism leading to

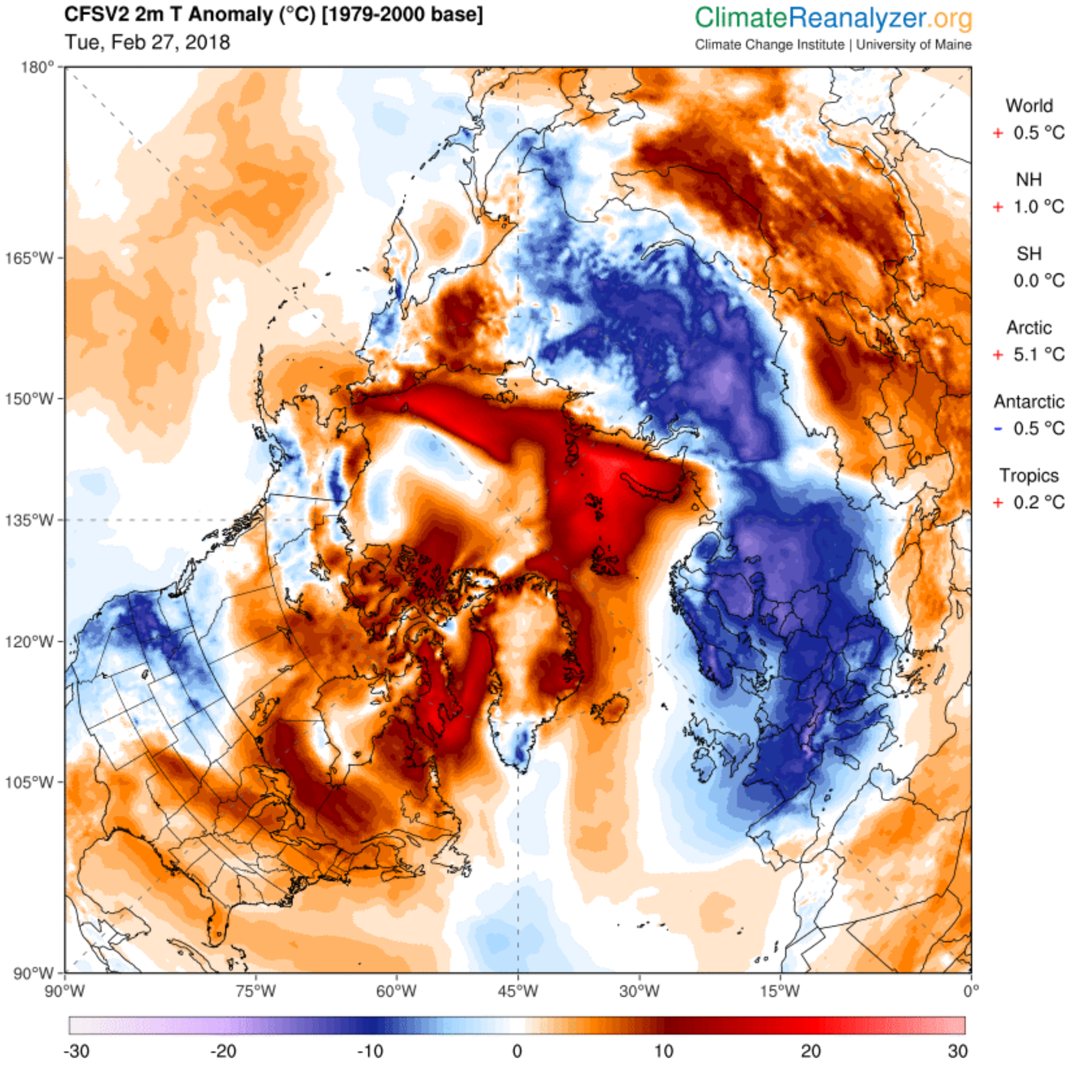
CFSV2 2m T Anomaly (°C) [1979-2000 base]
Tue, Feb 27, 2018
ClimateReanalyzer.org
Climate Change Institute | University of Maine
World
+ 0.5 °C
NH
+ 1.0 °C
SH
0.0 °C
Arctic
+ 5.1 °C
Antarctic
- 0.5 °C
Tropics
+ 0.2 °C
180°
165°W
150°W
135°W
120°W
105°W
90°W
90°W
75°W
60°W
45°W
30°W
15°W
0°
-30
-20
-10
0
10
20
30

**Figure 1.1.:** Temperature anomaly in the northern hemisphere on 27 February 2018. Image taken from the Climate Reanalyzer provided by the Climate Change Institute, University of Maine, USA (https://ClimateReanalyzer.org, last visit on Dec. 18, 2018).

changes in the storm tracks and why the projections vary between certain models (Lehmann et al. 2014).

This study aims to contribute to the understanding of changes in Equator-to-pole gradients and the storm track responses to Arctic amplification and climate change. To this goal, I analyzed Radio Occultation (RO) temperature data and compared them to other data sets. I calculated the temperature trends for the polar and tropical regions from 2001 to 2017 and the difference between these two latitude bands. In contrast to previous studies where the Equator-to-pole temperature gradient was only calculated for model data with specific altitude levels, the data in this study are from observations and the temperature difference trend is computed continuously from 2 km up to 30 km. In addition to the global view, I analyzed the Atlantic region separately as some specific anomalies can be found there. Investigations on seasonal trends and geopotential height trends provide further information about the Equator-to-pole gradient.

To calculate the temperature trends, a multiple regression approach is used, taking the natural variability into account. Commonly, the natural variation is described by indices of the main modes of variability, like the Quasi-Biennial Oscillation (QBO) or the El Niño–Southern Oscillation (ENSO), that do not cover the vertical details. For this work, I use new atmospheric variability proxies constructed directly from Global Navigation Satellite System (GNSS) RO temperature measurements of high vertical resolution. These indices are generated by an Empirical Orthogonal Functions (EOF) analysis and were first utilized by Wilhelmsen et al. (2018). In addition to Wilhelmsen et al. (2018) I calculated indices for the polar region and applied them to the regression. Through the removed natural variability, the uncertainties are reduced significantly and the trend estimate becomes more robust.

The number of available RO profiles is limiting the temporal and spatial resolution of the analysis in this work. Thus, it is not possible to entirely resolve particular storm tracks with RO data. To picture the problems, two extreme storm events in 2009 and 2011 are investigated. By working on daily resolved isentropic and pressure surfaces, strong "slow" storms can be identified. However, fast moving storms are hard to detect. So, this study also demonstrates the limits of the currently provided RO data resolution and should give information on the required number of RO profiles to reliably capture more storm events.

My thesis is organized in the following way. Basic characteristics of the Earth's Atmosphere are presented in the second chapter. This includes a description of the vertical structure as well as an overview on natural variability and Arctic amplification. Furthermore, the dynamics of storms are explained. Chapter three describes the GNSS RO data sets as well as the model data that are used for comparison. The fourth chapter is concerned with the methods and mathematical basis for the trend analysis used for this study followed by the results presented in chapter five. A summary and conclusions are given in Chapter six.

# 2. Characteristics of the Earth's atmosphere

> "Impacts on natural and human systems from global warming have already been observed (high confidence). Many land and ocean ecosystems and some of the services they provide have already changed due to global warming (high confidence)." (IPCC 2018).

## 2.1. Vertical structure

Until Kepler's laws of planetary motion were published in the early 17th century, most physicists pictured the movement of planets through rotating spheres. Today we know that this does not match the facts at all, but we still use the term "sphere" for another natural phenomenon – to describe the different vertical layers formed by the thin envelope of gases held through gravity on Earth. The boundaries between these layers are known as "pauses" (Dreyer 1906; Brasseur and Solomon 2005). The spheres are often divided by their different physical properties including thermal characteristics, chemical composition, electrical attributes, or density.

In the literature two common classifications are used to describe the vertical structure of the Earth's atmosphere. The distribution of gases divides the atmosphere into a well-mixed homogeneous part and a heterogeneous part, which is not uniformly mixed but separated according to the atomic weight of each occurring gas. Beside this classification into homosphere and heterosphere there is also the categorization by the vertical temperature gradient, which leads into four major layers known as the troposphere, stratosphere, mesosphere, and thermosphere (Fig. 2.1). Interactions between different atmospheric gases and radiant energy from Sun and Earth drive significant fluctuations in the vertical temperature profile (Brasseur and Solomon 2005).

**Troposphere:** The troposphere encompasses the bottom layer of the atmosphere, from the surface to the tropopause at about 12 km in the global mean. It contains the bulk of the atmospheric mass and is primarily heated by radiant energy exchanges from the underlying surface. At Mean Sea Level (MSL) the averaged surface temperature is about 288 K, decreasing with height at an average rate of $6.5\,\mathrm{K\,km^{-1}}$, termed as the normal lapse rate. The top of the troposphere, known as the tropopause, has a nearly isothermal layer, with a lapse rate less than $2\,\mathrm{K\,km^{-1}}$. The tropopause occurs above the Equator at around 17 km (Highwood and Hoskins 1998) and at 8 km over the poles. The flow of energy is dominated by the water vapor circulation and nearly all cloud and weather phenomena are restricted to this layer (Aguado and Burt 2006).

**Stratosphere:** Beyond the tropopause, the temperature gradient reverses, mainly caused by the absorption of solar Ultraviolet (UV) radiation through ozone molecules. The layer where this reversal can be identified is called stratosphere. The temperature profile creates very stable atmospheric conditions, with hardly any vertical motion. A Sudden Stratospheric Warming (SSW) event can destroy these robust layering which results in a downward shift of the stratopause. The upper limit of the stratosphere terminates at approximately 50 km with a mean temperature of 270 K, marking the transition zone between the stratosphere and the much colder mesosphere (Marshall and Plumb 2008).

**Mesosphere:** Due to the lower ozone density, the temperatures in the mesosphere decrease rapidly with height. This layer is cooled by radiative emission from $CO_2$ and the mean temperature at the mesopause at 80 km is about 180 K. The temperatures in the mesopause can cool down to less than 150 K in the polar summer, which marks the lowest temperature in the atmosphere (Plane 2003). This can even cause ice clouds to form in the polar region. Further up, nitrogen oxides are being ionized by Lyman alpha hydrogen radiation. Those are responsible for a part of the ionosphere, the D layer, which is only present during the day.

**Thermosphere:** The energy budget of the upper atmosphere is primarily balanced by the heating of gas due to the absorption of solar extreme UV and X-ray radiation. Additional important factors are heat transport due to conduction and convection and heat loss due to Infrared (IR) emission (Bates 1959). Above the mesopause, extreme UV radiation is absorbed and a part of its energy goes into heat, leading to a positive temperature gradient. This region is called thermosphere. While convection is the main heat transport process in the lower thermosphere, heat is transferred through conduction into the upper thermosphere, forming an isothermal region. Kinetic temperatures between 500 K and 2000 K can be found in this layer, causing an ionization of neutral gases which can be perceived as a phenomenon called aurora. The homopause level occurs in the thermospheric region where the eddy diffusion coefficient is equal to the molecular diffusion coefficient. Depending on the solar activity, the thermopause is located between 250 km and 500 km (Stewart 1968; Mohanakumar 2008).

The region above the thermosphere is called exosphere. The air in the exosphere is very thin and particles can easily reach the escape velocity. There is no clear-cut upper boundary where the exosphere finally fades away into space. Different definitions place the top of the exosphere somewhere between 100 000 km and 190 000 km above the Earth's surface (Bauer and Lammer 2004).

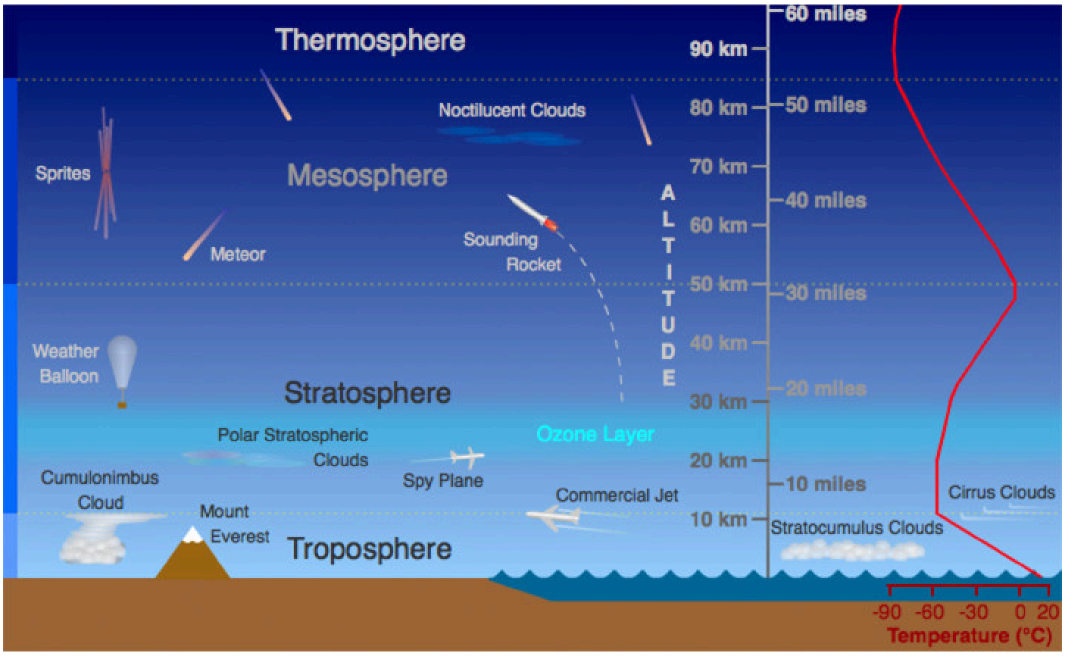
Thermosphere
90 km
60 miles
80 km
50 miles
Noctilucent Clouds
Sprites
Mesosphere
70 km
40 miles
ALTITUDE
60 km
Sounding Rocket
Meteor
50 km
30 miles
Weather Balloon
40 km
Stratosphere
20 miles
30 km
Polar Stratospheric Clouds
Ozone Layer
20 km
Spy Plane
10 miles
Cumulonimbus Cloud
Commercial Jet
Cirrus Clouds
Mount Everest
10 km
Stratocumulus Clouds
Troposphere
-90 -60 -30 0 20
Temperature (°C)

**Figure 2.1.:** Structure of the Earth's atmosphere as a function of temperature. Figure taken from University Corporation for Atmospheric Research, UCAR (https://scied.ucar.edu/atmosphere-layers, last visit on Oct 20, 2018).

## 2.2. Arctic amplification

Since the mid-20th century, temperatures have increased two to three times faster in the Arctic region than in the mid-latitudes, a phenomenon known as Arctic amplification. Polar amplification takes place in all seasons, but is strongest in autumn and winter (Perlwitz et al. 2015; IPCC 2018). Dramatic melting of Arctic sea ice and reduced spring snow cover are the results of this warming, especially after the year 2000. Even climate models have not predicted the fast-changing pace in this area. Recent studies linked Arctic amplification to changes in storm tracks, the jet stream, and planetary waves and their associated energy production (Fig. 2.2). Due to the relatively short length of observations and the overall poor sample size in the Arctic region it is difficult to develop predictions on how this area will change in the future (Cohen et al. 2014).

There is a general agreement that sea ice loss caused the warming of the Arctic through ice-albedo feedbacks (Screen and Simmonds 2010; Cohen et al. 2014). When the reflective and bright ice melts, it transforms into darker ocean water; this amplifies the warming trend as open water has a much lower albedo than ice, so more sunlight is absorbed at the ocean's surface. So losing sea ice is a key factor as it reduces the Earth's total albedo significantly (Screen and Simmonds 2010). When the air cools to temperatures lower than the ocean surface during autumn, the absorbed heat from the ocean is released into the atmosphere via radiative and turbulent fluxes,

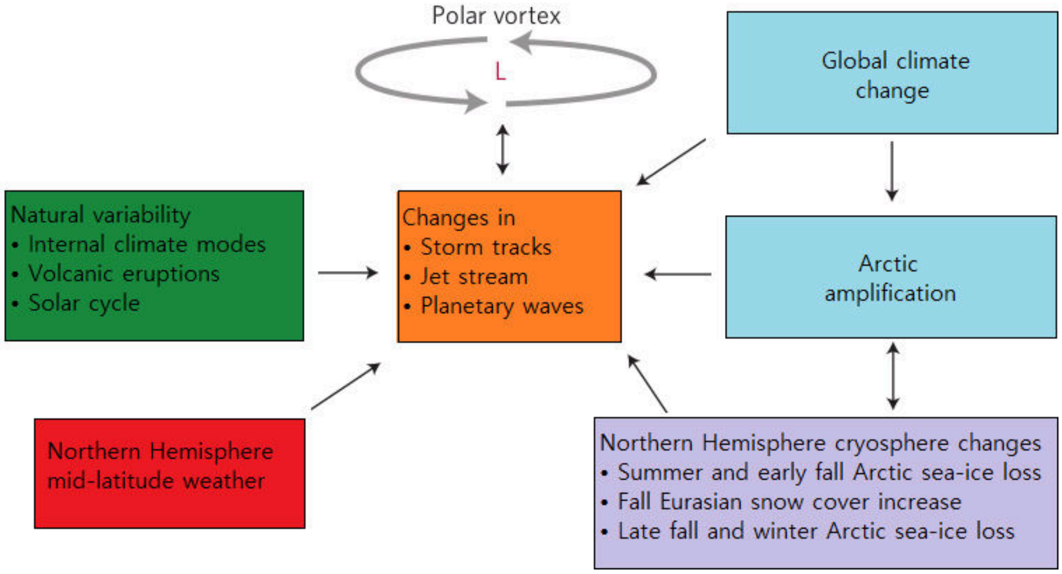
Polar vortex
L
Global climate change
Natural variability
• Internal climate modes
• Volcanic eruptions
• Solar cycle
Changes in
• Storm tracks
• Jet stream
• Planetary waves
Arctic amplification
Northern Hemisphere mid-latitude weather
Northern Hemisphere cryosphere changes
• Summer and early fall Arctic sea-ice loss
• Fall Eurasian snow cover increase
• Late fall and winter Arctic sea-ice loss

**Figure 2.2.:** Northern hemispheric mid-latitude weather cycle showing the influence of Arctic amplification on storm tracks, the jet stream, planetary waves and the cryosphere. Adapted from Cohen et al. (2014).

strongly warming the lower Arctic troposphere and slowing sea ice formation. As a result, the winter sea ice becomes thinner and easier to melt, this in turn increases the fraction of open water in this season further (Serreze and Barry 2011).

But amplification is also observed in models with no ice or snow through a strengthening in poleward heat transport and changes in the local net radiation balance (Alexeev et al. 2005). Variation in atmospheric and oceanic circulation, increasing cloud cover and anthropogenic soot in the Arctic environment are connected to polar amplification too (IPCC 2013).

In addition to these local drivers, Arctic temperature variation is also sensitive to changes of heat and moisture transport from lower latitudes towards the poles. Thunderstorms occur more often in the tropics, transporting heat from the surface to higher altitude levels where global wind patterns carry it polewards, creating a near constant heat flow away from the tropics. This process dampens warming near the Equator and contributes to Arctic amplification (Genio 2011). Additionally, a lot more water vapor is being transported towards the polar region by the jet stream. As water vapor is a greenhouse gas that traps heat in the atmosphere and can also condense as clouds that trap even more heat, it also plays an important part regarding the polar amplification (Francis and Vavrus 2015).

A direct connection between Arctic amplification and changes in speed and structure of the jet stream is still under investigation. As the polar amplification has weakened the temperature gradient near the surface, the temperature difference at higher altitudes has strengthened (Allen and Sherwood 2008). Further evidence from models suggests that cryospheric anomalies are key drivers of mid-latitude weather extremes as they alter the stratospheric vortex, storm tracks, and the jet stream (Cohen et al. 2014).

## 2.3. Storm tracks

Mid-latitude cyclones and anticyclones, also known as eddies, mainly occur in certain regions, labeled as storm tracks. They are statistically most common in North America, the North Pacific, and the Southern Oceans, as well as in the Mediterranean Sea. The European climate is strongly influenced by the storms which track across the Atlantic Ocean. Many high-impact weather experiences like strong winds and precipitation are associated with these intense cyclones. Overall, the storm tracks are very important components of the global climate system as they transport heat, momentum and moisture (Pinto et al. 2007; Woollings 2010; Shaw et al. 2016; Woollings et al. 2016). The intensity and location of storm tracks vary seasonally. The Atlantic storm track, for example, is much weaker and slightly further poleward in summer than in the other seasons (Trenberth and Stepaniak 2003; Woollings et al. 2014). The subtropical cyclogenesis (cyclone formation) in the North Atlantic peaks in September and October. The Fourth Assessment Report (AR4) models predict that the storm tracks will shift polewards in the future (Yin 2005; Barnes and Polvani 2013; Mbengue and Schneider 2017).

### 2.3.1. What determines cyclones

Cyclones are often defined as the region surrounding a local minimum in sea level pressure (Shaw et al. 2016). Mobile, extratropical cyclones play an important role in determining local weather conditions and have a strong connection to precipitation, clouds and radiation. Through their strong influence on vertical and horizontal exchange of heat, water vapor and momentum, they also have a primary role in the general circulation of the atmosphere (Bengtsson et al. 2005).

While extratropical cyclones or frontal cyclones contain frontal systems, tropical cyclones do not. Frontal cyclones are large traveling atmospheric vortices (rotating air), up to 2000 km in diameter, that form along linear bands of temperature gradients with significant vertical wind shear anywhere within the extratropical regions of the Earth (usually between 30° and 60° latitude from the Equator). An intense cyclone in the middle to high latitudes may have a surface pressure of only 970 hPa compared to an average sea-level pressure of 1013 hPa. Circulation around an area of low pressure is on the northern hemisphere counterclockwise and results in cold air moving southwards (Lynch and Cassano 2006).

The cyclone development is described in Fig. 2.3 in detail. In the initial state, two different fronts slowly move along each other, forming a boundary with a strong horizontal temperature gradient. Cyclonic evolution is initiated as a disturbance along the front which distorts the front into a wavelike configuration, visible in Fig. 2.3(a) and Fig. 2.3(b). As the pressure continues to decrease within the disturbance, the

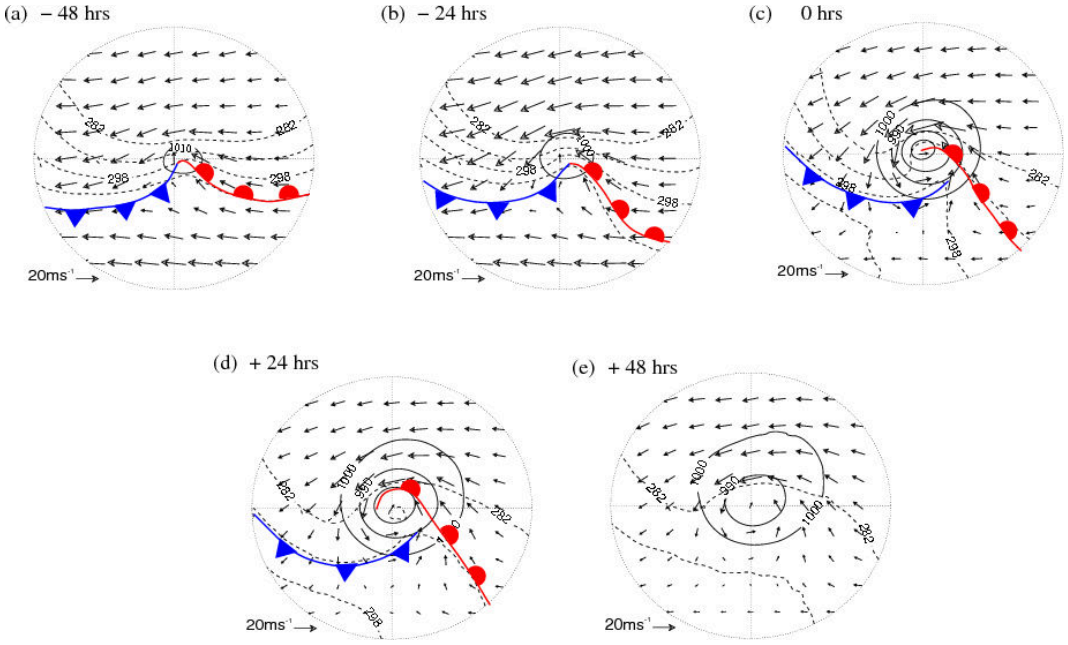

**Figure 2.3.:** Evolution of a cyclone on a 925 hPa wind field, dashed lines indicate the potential temperature at 282, 290 and 298 K. (a) 48 and (b) 24 h before the intensity maximum. (c) at the time of the intensity maximum. (d) 24 and (e) 48 h after the intensity maximum. Reprinted from Dacre et al. (2012).

cyclonic circulation and the system relative wind speeds around the center increase. This forces equatorward and poleward movements of cold and warm air. The cyclone continues to intensify, moving cold dense air rapidly equatorward, while the warm and less dense air streams in a northerly direction. At the maximum intensity, the lowest central pressure occurs, and the strong pressure differences result in peak wind speeds (Fig. 2.3(c)). The separation of the cyclone from the warm air toward the Equator can lead to a storm decay and a dissipation in a process called cyclolysis (Schemm and Sprenger 2015). During the first 24 hours of the decaying process the central pressure increases and the pressure gradients decrease leading to lower wind speeds (Fig. 2.3(d)). At the end of his lifecycle, the central pressure continues to rise and the frontal gradients weaken further (Fig. 2.3(e)) (Dacre et al. 2012). Additionally, to the development of cyclonic circulation in the atmosphere, tropical cyclones often transform into extratropical cyclones at the end of their tropical existence as they move toward higher latitudes. During a transition, the cyclone connects with a nearby front, ending in an increased size of the system and a weaker core. Usually the cyclone does not become subtropical during this transition (Hart and Evans 2001).

Tropical cyclones in comparison to frontal cyclones have little to no temperature differences across the storms surface. Their winds are derived out of the release energy from cloud formation and are strongest near the surface while extratropical cyclones have their strongest winds near the tropopause at 12 km. These differences occur because the "core" of a tropical cyclone is warmer than the environment in the troposphere whereas extratropical cyclones have their "warm-core" above the tropopause.

A circulation system goes through a series of stages until it intensifies and becomes a mature tropical cyclone. At the start, a tropical disturbance with loosely organized cumulonimbus clouds shows weak circulation. The storm is classified as a tropical depression once the wind speed increases to $36\,\mathrm{km\,h^{-1}}$. At a wind speed over $63\,\mathrm{km\,h^{-1}}$, the system is called a tropical storm. When the maximum wind speed exceeding $119\,\mathrm{km\,h^{-1}}$, the storm is classified as a tropical cyclone (Merrill 1984).

**Six conditions favorable for this process (Gray 1968):**

- Surface layer temperature of the ocean water must be 26.5 °C or warmer and at least 50 m deep.
- A preexisting atmospheric circulation near the surface is necessary.
- To support the formation of deep convective clouds, the atmosphere must cool quickly enough with height.
- At a height of 5 km above the surface the atmosphere must be relatively humid.
- Cyclones can only exist at least 500 km away from the Equator.
- The wind speed must change slowly with height through the troposphere with more than 10 meters per second between the surface and an altitude of about 10000 meters.

The dynamics of a tropical cyclone are based on the fact that the exterior of a storm is cooler than its core. It is necessary that the temperature of the atmosphere decreases sufficiently rapidly with height. The warm, saturated air moving upwards in the center of the circulation tends to keep rising as long as the surrounding air is cooler and heavier. This vertical movement allows the development of deep convective clouds. At about 5 km, some additional air from the surrounding atmosphere is drawn into the cyclone. If this outside air is relatively humid, the circulation will continue to intensify. If it is sufficiently dry, it can evaporate some of the water droplets in the rising column, making the air cooler than the surrounding air. This cooling leads to the formation of strong drops, which interrupt the ascending movement and inhibit the development (Gray 1968). The predominant mechanism that shapes cyclones in the atmosphere, called baroclinic instability, is discussed in the next section.

### 2.3.2. A closer look on baroclinic instability

Baroclinic instability, a fluid dynamical instability characteristic of rotating, stratified fluids, is the most important mechanism for generating weather in the mid-latitudes (Grotjahn 2014). It requires planetary rotation and a horizontal temperature gradient, created by differential solar heating that leads to colder poles compared to the Equator. Baroclinic instability converts potential energy into kinetic energy manifesting in cyclones and anticyclones (Marshall and Plumb 2008; Shaw et al. 2016). The energy conversions are proportional to the perturbation heat fluxes in both the vertical and horizontal directions. A zonal mean meridional circulation like the Hadley cell can generate these heat fluxes in the atmosphere. Various observed properties, such as the dominant length scales, the propagation speed, the vertical structure as well as the energetics can be simulated by theoretical models of baroclinic instability (Grotjahn 2014).

Since the available potential energy is related to a horizontal temperature gradient, which is proportional to the vertical shear of zonal wind, the baroclinic instability can be considered as a shear instability. Usually it is studied by linearizing dynamics equations and by using eigenvalue or initial value methods. The most complex models are compared with observational data but can be conceptualized for example in a so-called two-layer quasi-geostrophic model of the atmosphere. These alternative views and analysis techniques generally provide good opportunities for a better understanding of baroclinic instability (Grotjahn 2014; Shaw et al. 2016).

In a two-layer model the atmosphere is idealized as two dry, incompressible ideal gas layers that represent the upper and lower troposphere. The fluid flow is in geostrophic and hydrostatic balance. The instability occurs due to the vertical shear in the jet stream associated with the imposed horizontal temperature gradient resulting from the thermal wind balance. The quasi-geostrophic theories provide a reasonable prediction of the propagation speed and length scale of cyclones in the lower troposphere.

Typically, the baroclinicity is measured by the maximum Eady growth rate, named after its inventor Eric Eady, connecting the temperature gradient with the Coriolis parameter and the Brunt–Väisälä frequency. The Brunt–Väisälä frequency or buoyancy frequency is the angular frequency at which a vertically displaced parcel oscillates in a statically stable environment (Marshall and Plumb 2008). The maximum Eady growth rate is proportional to the Equator-to-pole temperature gradient and inversely proportional to the vertical potential temperature (see Sect. 2.5) gradient. So, the key variables determining the frequency and strength of storms within the storm tracks are the vertical and horizontal temperature gradients (Eady 1949; Shaw et al. 2016).

In the Earth's atmosphere, the origin of the baroclinic instability growth is the jet stream which has an unstable profile, either horizontally, vertically or in both directions. As the differential radiative forcing continues, the jet becomes stronger and more unstable until it breaks out in cyclones that transfer heat to the north. They reduce the temperature gradient and therefore release the instability, flatten the isentropic slope and dissipate the jet. During winter when the surface baroclinicity is strongest, the storm tracks generally reach their maximum intensity, while they had their minimum intensity during summer when the baroclinicity is weakest (Chang et al. 2002; Marshall and Plumb 2008).

### 2.3.3. Parameters that define storm paths

As mentioned in the previous sections, storms are caused by the global imbalance in solar heating, which creates horizontal temperature gradients. The higher latitudes radiate more heat to space than they receive from the sun, so additional heat must reach them by winds from lower latitudes. As a result, cold fronts sweep equatorward and warm fronts move poleward. When the fronts come together, the troposphere in this region becomes baroclinically unstable (see Sect. 2.3.2). Cyclones and anticyclones grow on this instability, reducing the temperature difference and converting available potential energy into eddy kinetic energy. Therefore, any changes to the temperature gradient may be expected to affect the storm tracks (Fig. 2.4) (Woollings 2010; Harvey et al. 2014).

Studies identify mid-latitude diabatic heating as a key process responsible for the maintenance of baroclinicity (Hoskins and Valdes 1990; Held et al. 2002; Chang 2009). Sensible heat transfer from the ocean is the main contributor to the diabatic slope restoration near the surface, but the latent heating due to condensation of water vapor dominates in the free troposphere. As individual storms are influenced by the release of latent energy through water vapor condensation, changes in local moisture content may be expected to affect the storm tracks. When the eddies are growing in a moister environment, they also experience stronger dry stability and weaker baroclinicity than they did before (Schneider et al. 2010). The general role of atmospheric moisture content in storm track changes is an ongoing field of debate (Bengtsson et al. 2009; Zappa et al. 2013; Ludwig et al. 2014).

Static stability, the ability of a fluid at rest to become turbulent or laminar due to the effects of buoyancy, additionally affects the storm tracks as well as the local baroclinicity, with increased stability inhibiting storm growth (Harvey et al. 2014). Various studies show that the Equator-to-pole temperature difference is increased at higher altitudes by tropical tropospheric warming in response to carbon dioxide increase in the atmosphere and weakened at lower levels by polar warming mostly caused by Arctic amplification (Cohen et al. 2014; Lin et al. 2017). The polar surface warming further decreases the static stability as the vertical temperature difference is increased significantly. In the tropical region, on the other hand, the static stability is strengthened by the reduced vertical temperature gradient (Fig. 2.4 (Rind 2008; Harvey et al. 2014). Therefore, a connection between storm tracks and the relative magnitudes of tropical upper troposphere and polar lower troposphere warming can be assumed (Rind 2008; Butler et al. 2010). When only polar warming is imposed on a model, an equatorward shift of storm tracks can be observed. The fact that models suggest a poleward shift results from an upper level dominance (Bader et al. 2011; Harvey et al. 2014).

Previous studies have explored a strong connection between storm tracks and the North Atlantic Oscillation (NAO). There is also a relationship to the Arctic Oscillation (AO) (Seierstad and Bader 2008). Changes in the tracks associated with the NAO/AO have a strong influence on the surface temperature and precipitation in the North Atlantic sector. During a positive NAO/AO phase, the storm tracks

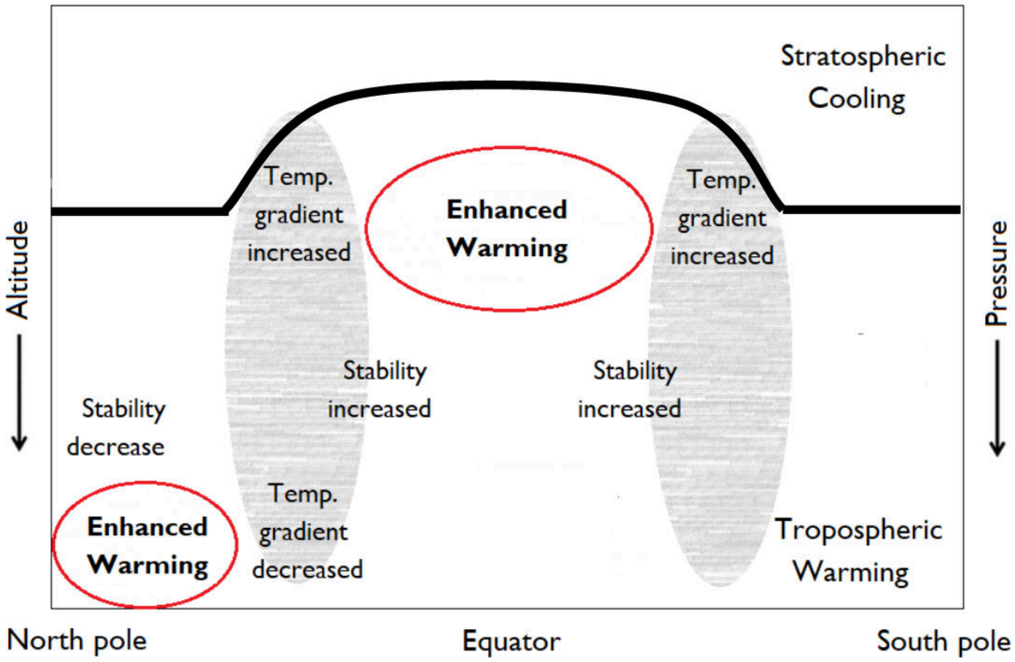
Stratospheric Cooling
Temp. gradient increased
Enhanced Warming
Temp. gradient increased
Altitude
Pressure
Stability increased
Stability increased
Stability decrease
Temp. gradient decreased
Enhanced Warming
Tropospheric Warming
North pole
Equator
South pole

**Figure 2.4.:** Schematic illustration of some global storm track change drivers. The storm tracks are marked in grey with the tropopause as a thick black line. Figure inspired by Woollings (2016).

shift polewards and winter comes mild across northern Eurasia and the east US but cold in the Arctic. In a negative phase, the tracks shift equatorward resulting in relatively mild Arctic temperatures and colder northern Eurasia and east US winters (Seierstad and Bader 2008).

Another important factor in the North Atlantic is the orientation of the North American coastline. The land-sea contrast and the sharp Sea Surface Temperature (SST) difference across the Gulf stream influence the storm track genesis. The variability in sea ice and snow ice cover has a significant effect on the storm tracks in some models (Seierstad and Bader 2008; Cohen et al. 2014).

On lower atmospheric heights the eddies form preferentially over the ocean surface with typical lifetimes of a few days. Eddy activity continues at upper levels across the land and this induces Rossby waves, which strongly influence the jet stream (Woollings et al. 2014; Woollings et al. 2016). While eddy-driven jets are derived from temporary large storm track eddies, the jets themselves steer and shape the evolution of the eddies, resulting in a strongly coupled system of eddies and mean westerly flow (Vallis and Gerber 2008; Shaw et al. 2016; Woollings 2016).

To investigate the storm track response to climate change, fully coupled ocean-atmosphere general circulation models are used. There was little consistency between models in the Fourth Assessment Report of the Intergovernmental Panel on Climate Change (IPCC) on how storm tracks might change in the future. However, Lambert and Fyfe (2006) showed a consistent modification in cyclone intensities across the

Coupled Model Intercomparison Project 3 (CMIP3), with an increase in stronger cyclones and an overall reduction in cyclone numbers.

To capture storm paths, either system-centered or Eulerian methods of storm track diagnosis are practicable. It is possible to use different fields like the Mean Sea Level Pressure (MSLP) or the upper (250 hPa) and lower (850 hPa) troposphere geopotential height, meridional wind and vorticity as well as potential vorticity on a 330 K isentropic surface. But there are various disadvantages; for example, the MSLP is strongly influenced by large spatial scales, such as the Icelandic low (Hoskins and Hodges 2002). Depending on the considered variable (Sea Level Pressure (SLP), geopotential height, or relative vorticity) it matters if local extremes are identified from a suitable anomaly fields or from the full field. Hoskins and Hodges (2002) for instance subtract the large area components of the fields to better understand the synoptic systems. Dynamic storm track measures like the high frequency geopotential height variance or eddy kinetic energy are to a certain degree subjective, such as the choice of filtering intervals for the high and band pass filter.

It is also possible that cyclones cells pass faster than the time steps of a method. Storm center tracking algorithms are used to determine the cyclones life time and location of the cyclogenesis and cyclolysis (see Sect. 2.3.1). The cyclone lifetime is important, because this parameter strongly influences the size of climatological ensemble of storm tracks as most of the circulations have a short lifetime of less than 2 days (Wernli and Schwierz 2006). The IMILAST project compared many different cyclone tracking methods and found that strong storms are generally identified by all methods (Ulbrich et al. 2013).

## 2.4. Atmospheric variability

Natural atmospheric variability refers to the variation in climate parameters caused by nonhuman forces. It occurs periodically, quasiperiodically or even emerges as sudden changes. There are two types leading to natural variability in atmospheric variables: those external and internal to the climate system. The external processes are the main driving force behind changes that occur over long time periods. The annual or seasonal cycle for example is induced by external solar irradiance variations caused by the tilting of the Earth's axis against the ecliptic. Additionally, feedback mechanisms can amplify the extent of the annual variation furthermore. It is necessary to take these natural signals in account when investigating anthropogenic climate changes (Yeh and Kirtman 2009; IPCC 2013).

### 2.4.1. The Quasi-Biennial Oscillation

The tropical Quasi-Biennial Oscillation (QBO) is perhaps one of the most spectacular low frequency variability phenomenons in the Earth's atmosphere. In the tropical stratosphere, equatorial zonal wind oscillates between easterlies, as wind blowing from the east is called, and westerlies with an irregular period of approximately 28 months. As soon as the easterlies fade out, the westerlies take over, and vice

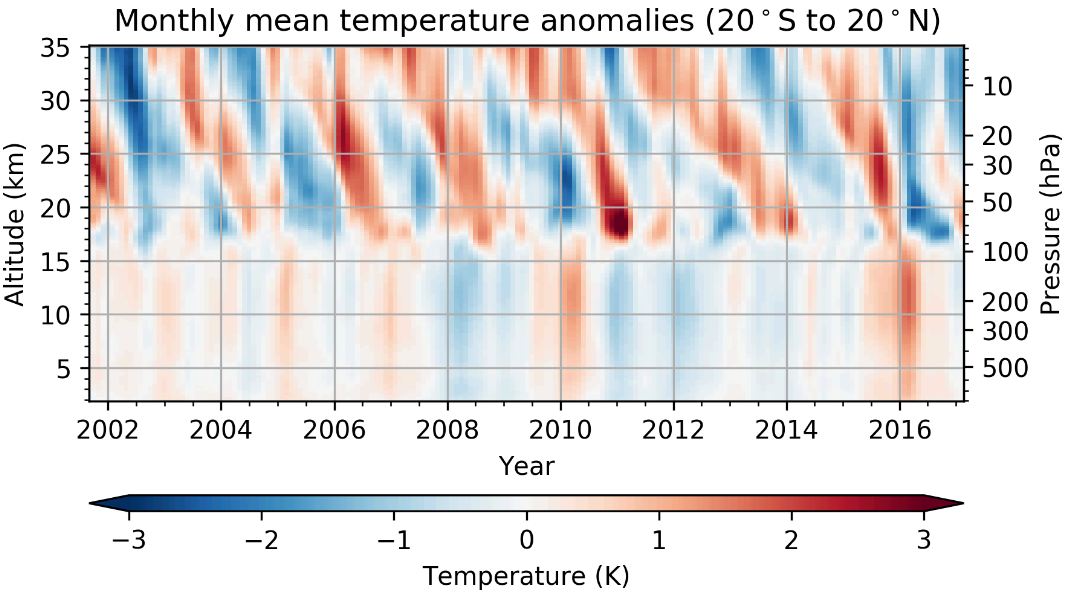

**Figure 2.5.:** Illustration of the downward-propagating Quasi-Biennial Oscillation (QBO) pattern in the lower stratosphere and the effect of El Niño–Southern Oscillation (ENSO) in the troposphere through zonal (−20° S to 20° N) monthly mean temperature anomalies between 2 km and 35 km. Figure taken from Wilhelmsen et al. (2018).

versa. The alternating wind regimes develop at the top of the lower stratosphere and dissipate at the tropical tropopause, propagating downwards at about 1 km per month (Scaife et al. 2000; Baldwin et al. 2001). The QBO-related winds at 10 hPa are in a different phase than the winds at 70 hPa, but they do not change a lot along the longitudinal axis (Naujokat 1986). The winds are centered latitudinal symmetric over the Equator with a meridional half width of approximately less than 15° towards higher latitudes (Dunkerton and Delisi 1985). The QBO reaches its largest amplitude of about 20 $\mathrm{m\,s^{-1}}$ in the middle to lower tropical stratosphere. In the 1970s, Richard Lindzen and James Holton recognized that the periodic wind reversal was driven by the vertical upwards transfer of momentum trough equatorial waves. These waves are dissipated in the stratosphere by radiative cooling and affect the stratospheric flow in the extratropics by modulating the effects of vertically propagating planetary waves (Scaife et al. 2000; Marshall and Scaife 2009).

The QBO is influenced but not synchronized to the annual cycle, as the change between eastward and westward winds tends to happen in the northern hemisphere in early summer and late spring. It is also strongly connected with the polar vortex and affects Sudden Stratospheric Warming (SSW) events (Andrews et al. 1987; Baldwin et al. 2001). The mixing of stratospheric ozone and modification of monsoon precipitation are two additional effects caused by the QBO. Cold Northern Europe winters and a weaker Atlantic jet stream often coincide with eastward phases of the QBO. A possible relationship between the QBO and the ENSO is currently a field of research (Newman et al. 2016).

It is practicable to investigate the QBO through temperature anomalies as they are proportional to the vertical gradient of the zonal wind (Randel et al. 1999; Baldwin et al. 2001). Figure 2.5 shows zonal (−20° S to 20° N) monthly mean temperature anomalies from Global Navigation Satellite System (GNSS) Radio Occultation (RO) data between 2 km and 35 km. It is easy to identify the quasi two-year period and the downward-propagating pattern. The strongest shifts correspond with the transition from westerlies to easterlies (Scherllin-Pirscher et al. 2017; Wilhelmsen et al. 2018). For a more accurate look into QBO features, see Holton and Hakim (2013).

### 2.4.2. El Niño-Southern Oscillation

In the troposphere, the dominant interannual variability mode is the El Niño–Southern Oscillation (ENSO), an irregularly periodic variation in winds and sea surface temperatures over the tropical eastern Pacific Ocean. The strong atmosphere-ocean coupling has three different states: The most familiar is the El Niño phase. In addition, there is the normal state of ocean and atmosphere and La Niña, the counterpart to El Niño. The phases have no fixed order and the events vary considerably in terms of magnitude, spatial pattern, temporal evolution, and predictability. This diversity results from the different roles of noise forcing and feedback processes (Jin et al. 2006; Capotondi 2015). Although the El Niño–Southern Oscillation (ENSO) presents itself as year to year climate fluctuation, its dynamics include a wide range of processes interacting on timescales that range from weeks to decades (Tziperman and Yu 2007; Choi et al. 2012). Its effects on atmospheric circulation can be detected globally, from the surface to the lower stratosphere (Randel et al. 2009).

Since the equatorial Pacific acts as a coupled system, air pressure and sea temperatures are the main driving factors. The positive feedback between ocean and atmosphere, or between sea surface temperature gradient and atmospheric circulation, explains the growth and amplification of the initial disturbance. The phase reversal from an El Niño to a La Niña state can be explained by the migration of long oceanic waves along the Equator.

In neutral years (Fig. 2.6 top), a pronounced high-pressure area in the central and eastern South Pacific generates a strong ground-level trade wind circulation. These trade winds carry large volumes of water vapor across the Pacific, leading to a distinctive low-pressure situation with intense thunderstorms and heavy rainfall over New Guinea and Indonesia. Rising humid air above Indonesia causes an eastward flow of air masses along the Equator. To compensate this near-ground east-west airflow, the ascended air in higher air layers flows back to the east and sinks again over South America. This leads to a closed equatorial circulation, which is according to its discoverer Sir Gilbert Walker also referred to as Walker circulation. Strong south-east trade winds provide an east-west directed ocean current, driving warm surface water from the South American coast to South Asia. In the Indonesian region, surface water is up to 8 °C warmer and the sea level is about 0.5 m higher than at the South American Pacific coast. While the warm water lowers the thermocline to 200 m in the Asian region, it is only 50 m deep in South America due to the eastward

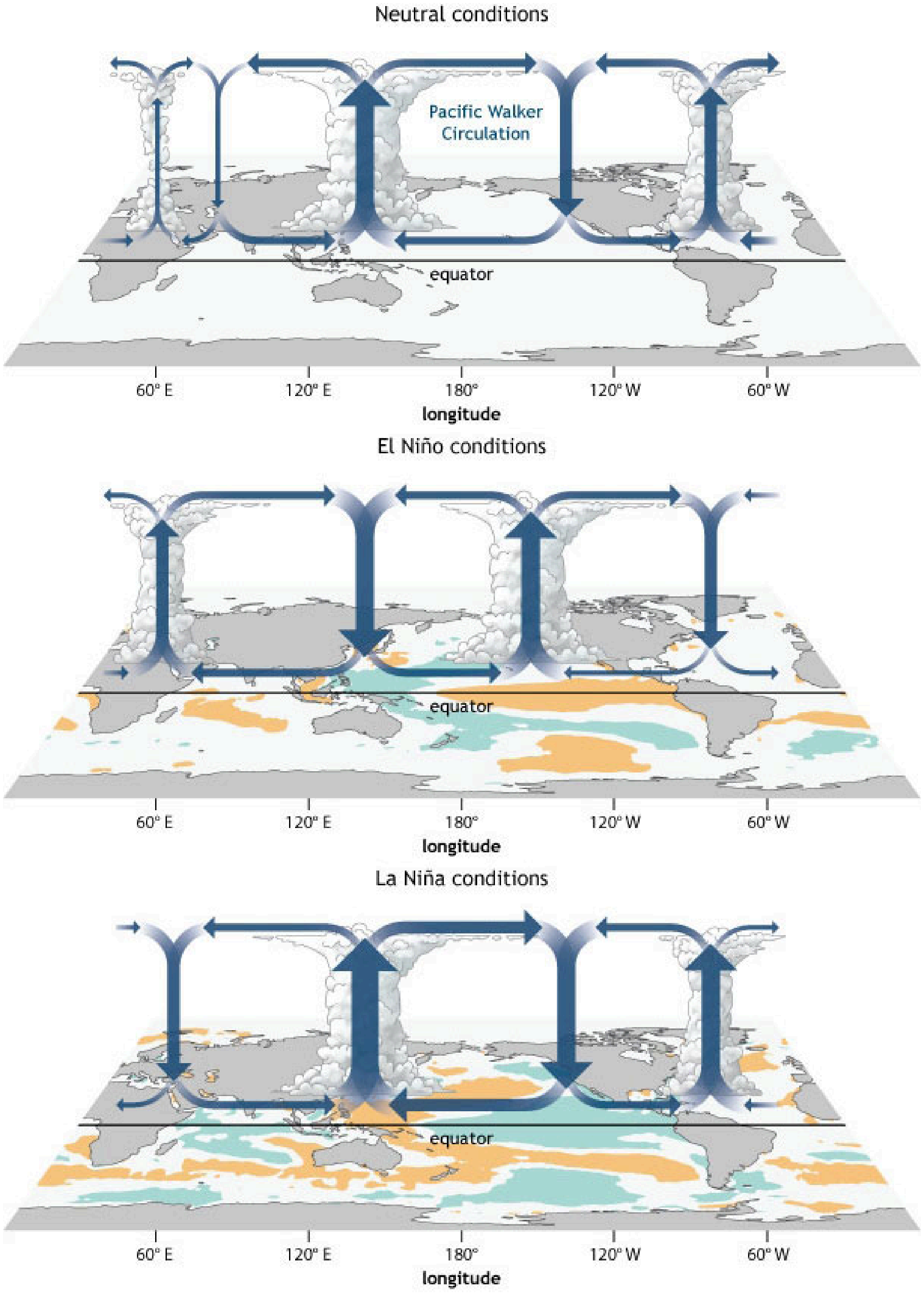
Neutral conditions
Pacific Walker Circulation
equator
60° E
120° E
180°
120° W
60° W
longitude
El Niño conditions
equator
60° E
120° E
180°
120° W
60° W
longitude
La Niña conditions
equator
60° E
120° E
180°
120° W
60° W
longitude

NOAA Climate.gov

**Figure 2.6.:** This diagram shows a model of surface temperatures and areas of rising air in the tropical Pacific during normal, El Niño, and La Niña conditions (top to bottom). Graphic taken from NOAA (https://www.climate.gov/enso, last visit on Oct 22, 2018).

drifting water. As a compensation for the drifting surface water, cold Antarctic deep water rises, resulting in cooler air over the sea surface with less water vapor percentage. Together with the dry, sinking air masses on the edge of the South Pacific anticyclones, this provides a low-rainy climate, especially on the coasts of Peru and northern Chile (Fig. 2.6 (top)).

Almost every autumn, this system begins to switch: The Inter-Tropical Convergence Zone (ITCZ) moves to the north, making the trade winds in the equatorial area a little weaker. The warm water stored in the West Pacific spills back in form of a Kelvin wave to the east within a few months. Thereby a noticeable warming of surface water, especially on the coasts of Ecuador and Peru, can be measured. The surface water is not mixed with the cool and nutrient-rich deep water, which leads to the death of all plankton and a migration of fish stocks. The eastward Kelvin wave also triggers a westward reflection wave, countering the flow reversal. That's the reason why a normal Walker circulation builds up again after a few weeks.

However, every two to ten years, an El Niño takes place where the flow reversal intensifies enormously and it comes to an extraordinary weakening of the South Pacific high-pressure area over several months. As a result, the southeast trade winds are weak or break down temporarily. This stops the equatorial water transport towards Indonesia. The cold Antarctic buoyancy water at the South American coast is largely covered by the backwashed warm water. This large-scale spread of warm water additionally weakens the South Pacific high-pressure area, resulting in an even greater slowing of the southeast trade winds and a reversal of the Walker circulation as the low pressure zone moves towards South America. In the coastal area of Ecuador, Peru and northern Chile, warm, humid air masses rise and cause heavy rainfall and flooding. In southeast Asia, however, high pressure systems are formed, causing long-lasting droughts (Fig. 2.6 (middle panel)) (IPCC 2007).

Between the El Niño years it happens that the normal conditions occur in a particularly strong form, these events are then called La Niña (Fig. 2.6 (bottom)). Although the ENSO is only active in the tropical Pacific, the variability of the Indian monsoon and the hurricane frequency in North and Central America are closely related to it. More than 90 % of the sun's energy is absorbed by the ocean, and several studies show that the ENSO can lead to short-term changes in the average global surface temperature of up to 0.39 °C (Trenberth et al. 2002). The variability in the troposphere due the ENSO phenomenon is visible in Fig. 2.5. El Niño events during winter 2002–2003, 2004–2005, 2006–2007 and 2009–2010 can be identified as well as a major event in 2015–2016 that lasts longer than normal (Timmermann et al. 2018). Additionally, La Niña events 2007–2008, 2010–2011 and 2011–2012 can be observed. For a review on the ENSO complexity, see Timmermann et al. (2018).

### 2.4.3. Sudden Stratospheric Warming events

A major, Sudden Stratospheric Warming (SSW) is possibly one of the most radical changes of weather that can be observed on our planet. Over a matter of days, the north polar stratospheric temperatures can fluctuate by more than 50 K. After this big change, the stratosphere recovers slowly to its typical state. These highly dynamic events also interact with the troposphere on a global scale and it seems that SSWs have occurred more frequently in the last 15 years (Butler et al. 2014).

The Sudden Stratospheric Warming events are caused by atmospheric waves forced through large-scale mountain systems of the northern hemisphere and land-sea distribution. At altitudes of about 10 km planetary-scale waves (Rossby waves) are formed, fed by temperature contrasts between land and ocean. This planetary waves are able to propagate into the stratosphere until they reach a critical layer, where they dissipate (Matsuno 1971). The upward moving waves have two effects: First, the air below the critical layer gets heated by the meridional flow (Schimanke et al. 2011). This leads to a decrease of the downward flow of the air at high latitude, weakens the polar vortex and additionally warms the polar surface region (Schoeberl and Newman 2014).

The most dramatic SSWs are called major warmings. During a major warming, the westerly winds at 60° N and 10 hPa reverse. This results in a complete disruption of the polar vortex and the vortex will either be displaced from its normal location of the pole or split into daughter vortices (McInturff 1978). While major warmings only occur every other winter, events of weaker amplitude appear frequently during the winter season. An example of stratospheric warming can be found in Fig. 2.7. The variability in the stratosphere also modifies the distribution of atmospheric trace gases, including stratospheric ozone. The polar vortex acts as a barrier between large trace gas concentrations within the vortex and small concentrations outside the vortex or vice versa. During a SSW event, the vortex collapses, removing this barrier and increasing the mixing of air between mid-latitudes and the polar region. This final warming often appears in March or April, when the polar vortex breaks down and reverses from the winter circulation into the summer circulation (Butler et al. 2017).

In the literature different definitions have been used to diagnose the occurrence of SSW events, yielding discrepancies in the detected events (Palmeiro et al. 2015). For more than ten years, SSWs have been identified by using daily synoptic weather maps at high altitudes. For this study, major SSW events were determined by using the diagnostic from Charlton and M.Polvani (2007) on zonal wind data at 60° latitude from NASA[1].

Recent research has conclusively shown that extreme events can have substantial impacts on winter surface climate, including increased frequency of cold air outbreaks over Eurasia and North America and anomalous warming over Greenland and eastern Canada (Butler et al. 2017). SSW events can also affect atmospheric chemistry,

---

[1] retrieved from http://acdb-ext.gsfc.nasa.gov/Data_services/met/ann_data.html, last visit on Sep 25, 2018

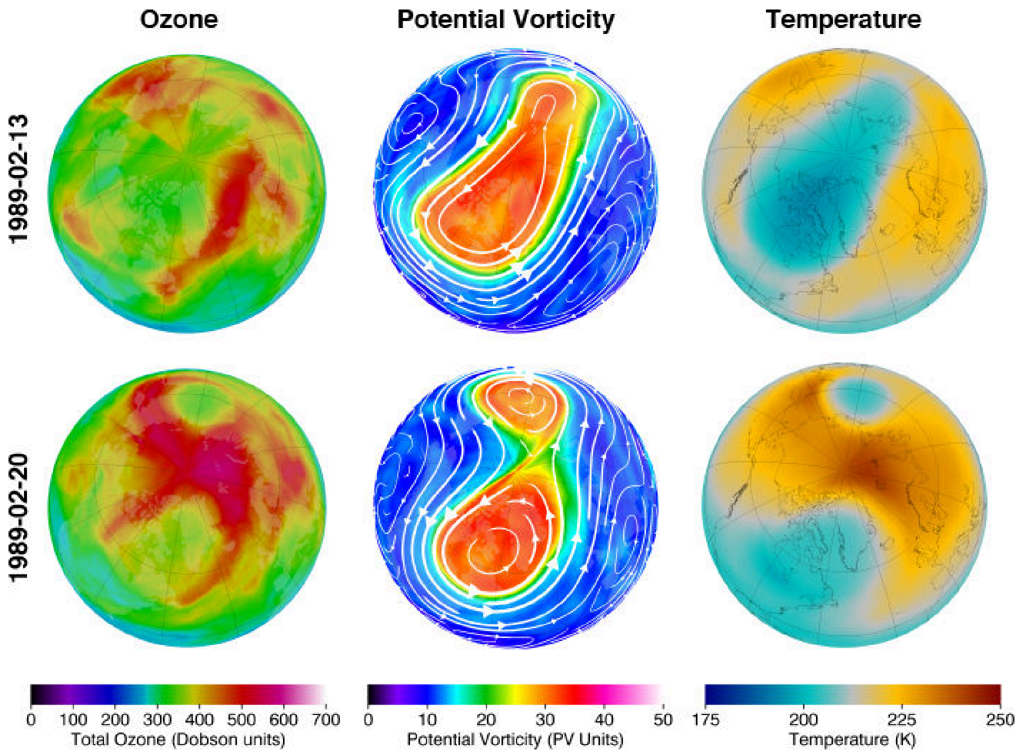
Ozone
Potential Vorticity
Temperature
1989-02-13
1989-02-20
0 100 200 300 400 500 600 700
Total Ozone (Dobson units)
0 10 20 30 40 50
Potential Vorticity (PV Units)
175 200 225 250
Temperature (K)

**Figure 2.7.:** Example of Sudden Stratospheric Warming events in the northern hemisphere through total ozone (left), potential vorticity on a 460 K potential temperature surface (mid), and temperature on a 50 hPa pressure surface (right) for 13 and 20 February 1989. Graphic taken from NASA Ozone Watch (https://ozonewatch.gsfc.nasa.gov/facts/warming_NH, last visit on Sep 18, 2018).

winds, and electron densities, as well as the electric fields and they extend from the surface to the thermosphere across both hemispheres. Baldwin et al. (2001) and Schimanke et al. (2011) showed the impact of SSW events on the North Atlantic Oscillation (NAO), the Arctic Oscillation (AO), and the location of storm tracks. In all these studies, an increase of geopotential height above the pole was observed and a decrease of geopotential height at mid-latitudes for at least 60 days after the peak of the warming has been mentioned. Outside of the tropics, an SSW event can displace extratropical cyclonic storm tracks towards the Equator, resulting in an increased probability that storms will pass over the United Kingdom and southern Europe. Additionally, record-breaking cold temperatures and snowfall in the eastern North America are possible (Kidston et al. 2015).

Studies show that individual SSW developments depend on the conditions of the winter stratosphere. They interact with some known oscillations like the ENSO or the QBO (Holton and Austin 1991; Labitzke et al. 2006; Butler and Polvani 2011). The solar cycle and strong volcanic eruption at high latitudes can also have an influence on stratospheric circulation.

## 2.5. Vertical coordinates

In meteorology it is customary to use pressure $p$ rather than height $z$ as the primary vertical coordinate. There is a practical advantage in observations as it is simpler to measure pressure in situ than height. With $p$ as a vertical coordinate, the height $z$ becomes a dependent variable $z(p)$ (Marshall and Plumb 2008).

However, the geopotential height $Z$ is a vertical coordinate related to the Mean Sea Level (MSL) of the Earth, an adaptation to the geometric height $z$ using the variation of gravity $g$ with latitude and elevation $h$. It can also be considered as a "gravity-adjusted" height. It can be calculated by:

$$Z(h) = \frac{\Phi(h)}{g_0} \tag{2.1}$$

with $g_0 = 9.806\,65\,\mathrm{m\,s^{-2}}$ as the standard gravity at MSL and $\Phi$ as the geopotential.

The geopotential $\Phi$ is defined as the work required to raise a unit mass to the height $z$ from Mean Sea Level:

$$\Phi(h) = \int_0^h g(\phi, z)dz \tag{2.2}$$

where $\phi$ is the latitude.

Geophysical scientists often utilize the geopotential height $Z$ as a function of pressure. Using the hypsometric equation, the geopotential height can also be calculated by:

$$Z = -[R\langle T(p, p_0)\rangle / g_0] ln(p/p_0) \tag{2.3}$$

where $\langle T(p, p_0)\rangle$ is the mean temperature from the surface to a certain pressure level $p$.

Geopotential height is valuable for locating troughs and ridges, highs and lows, which are the upper level counterparts of surface cyclones and anticyclones. Since warm air is less dense than cold air, it causes pressure surfaces to be higher in warmer air masses, while denser, colder air allows the pressure surface to be lower.

The geopotential height difference $\Delta Z = Z_2 - Z_1$ between pressure levels is referred to as the thickness of the layer. It is proportional to the mean virtual temperature in that layer. A line drawn on a weather map connecting points of equal geopotential height is called a height contour. At every point along a given contour, the values of geopotential height are the same. The geopotential height contours can be used to calculate the geostrophic wind, which is faster where the contours are more closely spaced and tangential to the geopotential height contour (Andrews et al. 1987; Marshall and Plumb 2008).

The potential temperature $\theta$ is by definition the temperature that a parcel of dry air at pressure $p$ and temperature $t_K$ would acquire if it were compressed or expanded adiabatically to the reference pressure $p_0 = 1000\,\mathrm{mbar}$:

$$\theta = t_K \cdot \left(\frac{p_0}{p}\right)^{\frac{R}{c_p}} \tag{2.4}$$

with $c_p$ as the specific heat at constant pressure and $R$ as the ideal gas constant. Thus, potential temperature, unlike temperature, is conserved under adiabatic displacement. Equation (2.4) directly determines how the temperature of an air parcel will change as it is moved around adiabatically. So, if $\theta$ is known, Eq. (2.4) allows to determine the temperature at any given pressure. The potential temperature can also be used as a field variable for characterizing the thermodynamic state of the atmosphere (Andrews et al. 1987).

The static stability of the unsaturated atmosphere can be measured by the potential temperature change with height as follow:

$$\left.\begin{array}{l}\text{unstable}\\ \text{neutral}\\ \text{stable}\end{array}\right\}\text{ if }\left(\frac{d\theta}{dz}\right)\left\{\begin{array}{l}<0\\ =0\\ >0\end{array}\right. \tag{2.5}$$

If the potential temperature decreases with height, a compressible atmosphere gets unstable. Observations of decreasing potential temperature with height are uncommon as the convection acts to fast mixing the atmosphere and turn it back to a stably stratified state. Since parcels with the same potential temperature can be exchanged without heating or work being required, lines of constant potential temperature can be assumed as natural flow pathways. This fact is used in isentropic analysis, which allows visualization of air movement and in particular analysis of vertical motion on a large-scale (Marshall and Plumb 2008).

# 3. Data sets

## 3.1. Radio Occultation data

Global Navigation Satellite System (GNSS) Radio Occultation (RO) data provide atmospheric temperature profiles with very high vertical resolution and independent information on altitude and pressure. This unique property is of substantial advantage when analyzing atmospheric characteristics that mainly focus on altitude and pressure knowledge as well as other thermodynamic atmospheric variables (Scherllin-Pirscher et al. 2017). Due to the particular characteristics of GNSS RO, these data are often used for numerical weather prediction (Kuo et al. 2000), climate monitoring (Steiner et al. 2001), ionospheric research (Schreiner et al. 1999), and space weather calculations (Jakowski et al. 2002).

In this study, troposphere and lower stratosphere data from 2001 to 2017 are used. The data are based on RO sensors from different Low Earth Orbit (LEO) satellite missions. Continuous RO observations of the Earth's atmosphere were delivered by the German Challenging Mini-Satellite Payload (CHAMP) satellite (Wickert et al. 2004) from mid-2001 to October 2008 shown in Fig. 3.1. In addition to the CHAMP measurements, the Argentine Satélite de Aplicaciones Científicas/Scientific Applications Satellite C (SAC-C) (Hajj et al. 2004) and the U.S./German Gravity Recovery and Climate Experiment (GRACE) (Wickert et al. 2005; Beyerle et al. 2005) missions, both launched in 2002, gathered data till 2013 respectively 2017. Ongoing RO missions are the Taiwan/U.S. FORMOSAT-3/COSMIC (F3C) (Anthes et al. 2008; Anthes 2011) and the European Meteorological Operational (MetOp)/Global Navigation Satellite Systems Receiver for Atmospheric Sounding (GRAS) (Loiselet et al. 2000; Luntama et al. 2008) missions. Additionally, the German Terra Synthetic Aperture Radar (TerraSAR-X) satellite provides a small amount of RO data (Wickert et al. 2009).

All the RO observation satellites mentioned above receive radio-wave signals from Global Positioning System (GPS) satellites in an active limb sounding (occultation) geometry (Fig. 3.2). The theory of the limb sounding is first described by Baum and Code (1953). It is a remote sensing technique and acquires, in contrast to in-situ measurements, information about the atmosphere without being in direct contact with it (Elachi and Zyl 2006).

During an occultation event the GPS signals propagate through the atmosphere, where they get bent due to the Earth's density gradients. This bending can be identified as a phase-shift with respect to the original signal. The measurement is based on high-precise, synchronized atomic clocks on the emitting and receiving satellites. The retrieval (Fig. 3.3 of the temperature profiles with the WEGC

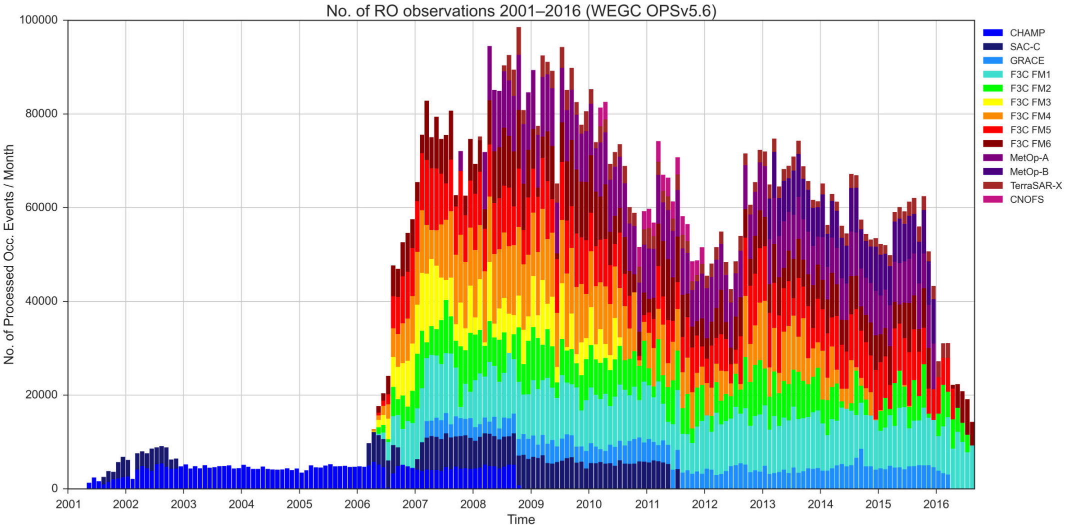

**Figure 3.1.:** Number of RO observations between 2001 and 2016 used for the Wegener Center for Climate and Global Change (WEGC) OPSv5.6 processing (Angerer et al. 2017).

Occultation Processing System version 5.6 (OPSv5.6) includes the elimination of the ionospheric influence on the measurement by a combination of two GPS signals (two carrier frequencies: 1575.42 MHz and 1227.60 MHz) as well as a Doppler-shift correction. The Doppler-shift correction is necessary due the movement of the emitting and receiving satellites and it utilizes precise orbit information like the position and velocity of these satellites. It is also used to calculate the bending angle $\alpha$ from the phase-shift assuming local spherical symmetry (Scherllin-Pirscher et al. 2011b; Liu et al. 2013). An inverse Abel integral (Fjeldbo et al. 1971) is applied to obtain the refractive index $n$ as a function of $a$ certain radius $r_t$.

$$n(r_t) = \exp\left[-\frac{1}{\pi}\int_{a_t}^{\infty}\frac{\alpha(a)}{\sqrt{a^2-a_t^2}}\,da\right] \tag{3.1}$$

The bending angle $\alpha$ is $a$ function of the vertical distance a between the center of refraction and the ray asymptote. Under the assumption of spherical symmetry, the refractive index $n$ reaches its maximum when the ray is closest to the Earth's surface. This indicates the radius of the Tangent Point (TP) $r_t$. To avoid a singularity at $a = a_t$ an integration per layer is used at the WEGC (Steiner 1998). The refractivity profile $N(h)$ for different heights $h$ above Mean Sea Level (MSL) is given by:

$$N(h) = 10^6(n(h) - 1) \tag{3.2}$$

To retrieve atmospheric parameters from the refractivity, the Smith–Weintraub formula is used (Smith and Weintraub 1953). In the presence of non-negligible

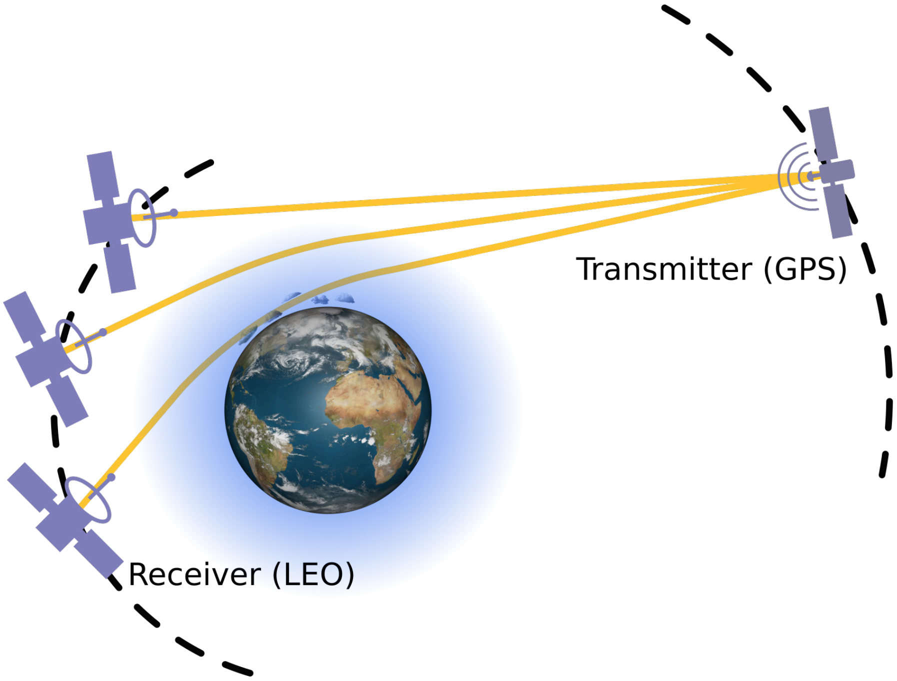

**Figure 3.2.:** Schematic principle of a RO event. Radio signals from GPS satellites bend as they pass through the atmosphere; the amount of bending relates to the atmospheric pressure, temperature, and moisture levels.

atmospheric humidity (tropical tropospere), additional background information must be included. For OPSv5.6, European Centre for Medium-Range Weather Forecasts (ECMWF) short-range forecast are used. For statistical optimization between 40 km and 120 km, short-range forecast profiles of the ECMWF are used to initialize the Abel integral in the WEGC OPSv5.6. This processing step stabilizes the retrieval and minimizes residual ionospheric errors from solar activity (Gobiet and Kirchengast 2004; Steiner et al. 2013). The RO products are therefore not entirely independent from ECMWF background data. A detailed description of the WEGC OPSv5.6 can be found in Schwärz et al. (2013).

Overall, the RO method has several distinct benefits like a high accuracy of less than 1 K for individual profiles in the upper troposphere and lower stratosphere. The precision totals less than 0.05 K. The accuracy is influenced by instrument quality, the condition of the atmosphere and the ionosphere as well as the exactness of the orbit determination and the quality of the initialization of the Abel integral (Kursinski et al. 1997; Schreiner et al. 2007; Anthes 2011; Scherllin-Pirscher et al. 2011b; Scherllin-Pirscher et al. 2011a; Ladstädter et al. 2015). Ladstädter et al. (2015) compared RO with Radiosonde Observation (RAOB) (VAISALA) data. They discovered a good agreement between RO and RAOB data in the Arctic.

Due to the self-calibrating nature of the measurement, data between different receiver satellites are highly consistent and can be combined to a single long-term

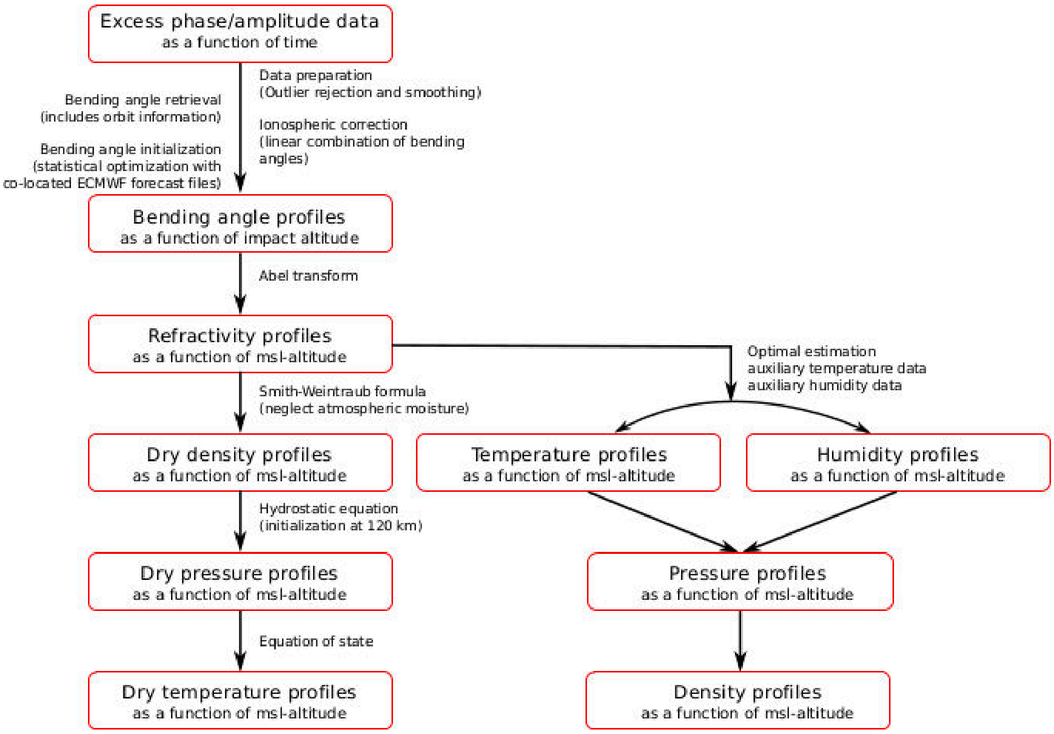
Excess phase/amplitude data
as a function of time
Data preparation
(Outlier rejection and smoothing)
Ionospheric correction
(linear combination of bending angles)
Bending angle retrieval
(includes orbit information)
Bending angle initialization
(statistical optimization with co-located ECMWF forecast files)
Bending angle profiles
as a function of impact altitude
Abel transform
Refractivity profiles
as a function of msl-altitude
Optimal estimation
auxiliary temperature data
auxiliary humidity data
Smith-Weintraub formula
(neglect atmospheric moisture)
Dry density profiles
as a function of msl-altitude
Temperature profiles
as a function of msl-altitude
Humidity profiles
as a function of msl-altitude
Hydrostatic equation
(initialization at 120 km)
Dry pressure profiles
as a function of msl-altitude
Pressure profiles
as a function of msl-altitude
Equation of state
Dry temperature profiles
as a function of msl-altitude
Density profiles
as a function of msl-altitude

**Figure 3.3.:** Summary of the processing steps of the OPSv5.6 retrieval at the WEGC taken from Schwärz et al. (2013).

stable climate record (Foelsche et al. 2011a). RO measurements can be performed under all weather conditions (clear and cloudy air) due to the microwave GPS signals. The typical horizontal resolution of about 60 km in the lower troposphere to about 300 km in the stratosphere is described in Kursinski et al. (1997). It allows applications at mesoscales to larger scales. Due to the limb sounding technique of RO, the data have a high vertical resolution from 0.1 km near the surface to about 1.5 km in the stratosphere. This can be used to get information on specific levels such as the tropopause or the planetary boundary layer (Kursinski et al. 1997; Gorbunov 2002). Due to the fixed GPS satellites inclination of 55° and the increasing number of LEO satellites, the measurements are performed globally and asynoptic over a full diversity of (local) times. Since almost all RO satellites are in high inclination orbits, even Sudden Stratospheric Warming (SSW) events can be studied with RO data.

## 3.2. Model data

Forecasts and reanalyses use numerical models of the atmosphere and oceans to make short-term weather prognoses or longer-term climate predictions. A dynamic model of the atmosphere and the physical processes that occur, like cloud formation, is needed as well as models of other processes in the Earth system such as atmospheric composition, the land processes and marine environment. The forecasts are limited by the fact that the atmosphere is chaotic and that mathematical models cannot perfectly represent the laws of physics governing the dynamic equations. The models also have to be simplified for many processes with very small scales, such as the formation of clouds, which results in some uncertainties (Dee et al. 2011). The comprehensive Earth-system model developed at ECMWF in co-operation with Météo-France forms the base for all model data used in this work. All the main applications required are available through one computer software system called IFS.

### 3.2.1. ECMWF analyses

Six-hourly global operational analysis data from the ECMWF between December 2001 and February 2017 are utilized for the comparison with RO data. For the assimilation process, a lot of observations are used, including RO measurements (Healy 2007). The forecast fields are averaged over a period of 6 h centered on synoptic times, i.e. 0000, 0600, 1200 and 1800 UTC, derived from forecast lead times between 3 and 27 h. The data have a horizontal resolution (T42) of 64 points in latitude and 128 points in longitude, which roughly equals the horizontal resolution of RO measurements (Borsche 2008). The vertical resolution is 91 layers (L91) between the Earth's surface and about 0.01 hPa (80 km altitude) (Richardson 2005). In this study, six-hourly interval data as well as a monthly climatology from this ECMWF field are used.

### 3.2.2. ERA-Interim

In addition to the six-hourly ECMWF data, ERA-Interim (ERAI) fields are utilized for comparison. erai is a global atmospheric reanalysis and combines a numerical forecast model and observations since 1979. The data assimilation system that was used to produce ERAI data is based on a 2006 release of the Integrated Forecasting System (IFS) (Cy31r2). The system includes a 4-dimensional variational analysis (4D-Var) with a 12-hour analysis window. The spatial resolution of the data set is approximately 80 km (T255 spectral) on 60 vertical levels from the surface up to 0.1 hPa (Simmons et al. 2007; Dee et al. 2011). For more information about ERA-Interim see, e.g. Poli et al. (2010), Dee et al. (2011) and Simmons et al. (2014).

## 3.3. Data preprocessing

In my study I use monthly mean temperature RO data as well as interpolated ECMWF and ERAI data sets on a 2.5°×2.5° horizontal grid. This 144×72 longitude-latitude grid has a vertical grid of 100 m from the Earth's surface to 60 km altitude (601 points). For each grid point, all RO profiles within 300 km radius from the center of the grid are used. At higher latitudes, more profiles are within this radius, resulting in a larger sample size and a stronger Sampling Error (SE) correction (see Sect. 3.3.1 and Fig. B.3). All data sets range from December 2001 to February 2017.

### 3.3.1. Sampling error correction

All RO climatologies are affected by random (statistical) errors, sampling errors, and systematic errors. The total climatological error results from combining these error components. While the magnitude of the statistical error depends primarily on the number of measurements, the SE is also strongly influenced by the sampling density and atmospheric variability (Pirscher et al. 2007; Foelsche et al. 2008). As the atmospheric variability is strongest at high latitudes during wintertime, the largest SEs occur during this period of time (Fig. B.3 and Fig. B.4 to Fig. B.18).

Scherllin-Pirscher et al. (2011a) recommended to subtract the SE when using RO climatologies for climate research. A reasonable approach to estimate the magnitude of the SE is the comparison to a "true" reference field. In this study I assume that ECMWF analysis fields are valid approximations of the "true" global field.

Pirscher (2010) described the methodology for the SE estimation of RO in detail. In summary, collocated ECMWF profiles are averaged to latitudinal bands and monthly means, representing the atmospheric state at the times and locations of RO measurements. Then the SE is calculated by subtracting this collocated field from the ECMWF field, thereby estimating the error caused by not fully sampling the atmospheric state. In the last step, the estimated SE is subtracted from the RO field. The substantial quality improvement of the RO climatological fields by this method has been shown in different studies (Foelsche et al. 2011b; Scherllin-Pirscher et al. 2011b; Ladstädter et al. 2011). Impacts on my study can be found in Sect. B.

### 3.3.2. Preparation for the temperature difference calculation

First, zonal bands are computed from the monthly mean temperature data. Then, the monthly mean temperature anomalies are created to deseasonalize the input data. This is achieved by calculating the average temperature for each month for a reference time period from January 2002 to December 2016. The monthly averages are then subtracted from the original temperature data at the corresponding months. To reduce statistical errors, the RO data sets are latitude weighted (weighting by cosine of latitude). These fields are used for the computation of Equator-to-pole temperature differences and trends.

### 3.3.3. Preparation for storm analysis

For a more detailed look on storm events, quality-controlled (Angerer et al. 2017) daily weighted (over 5 days) RO profiles from September 2006 to August 2016 are utilized. The profiles are first brought to a consistent grid. In the vertical direction, each profile is interpolated to pressure levels $p$ corresponding to an altitude grid $z$ with 200 m steps using the barometric formula:

$$p(z) = p_0 \exp\left(-\frac{z}{H}\right), \tag{3.3}$$

with the scale height $H = 7000\,\mathrm{m}$ and the standard surface pressure $p_0 = 1013.25\,\mathrm{hPa}$. Then the profiles $x_i$ are averaged in the horizontal direction to a regular 2.5°×2.5° longitude-latitude grid $x_{\mathrm{grid}}$ by applying a weighted mean given as:

$$x_{\mathrm{grid}}(\lambda, \phi, d) = \frac{\sum_i w_i x_i(\lambda_i, \phi_i, d_i)}{\sum_i w_i} \quad \text{with} \tag{3.4}$$

$$w_i = \begin{cases} \exp\left(-\left[\left(\frac{\Delta\lambda_i}{L}\right)^2 + \left(\frac{\Delta d_i}{D}\right)^2\right]\right) & \text{if } (\lambda_i, \phi_i, d_i) \text{ in } (\lambda \pm 7.5°, \phi \pm 2.5, d \pm 2) \\ 0 & \text{else,} \end{cases}$$

$\Delta\lambda_i = \lambda - \lambda_i$ is the continuous longitudinal distance of a certain profile at a longitude $\lambda_i$ with reference to the grid center $\lambda$ while $\Delta d_i = d - d_i$ describes the (discrete) temporal distance of a certain profile on a day $d_i$ to the reference day $d$, $L = 7.5°$, and $D = 1$ day (see also Randel and Wu 2005).

Averaging the profiles of five days and the resulting effective resolution of 15°×5° in longitude and latitude has been chosen for minimizing the number of empty grid cells, while still being able to resolve the maximum amount of atmospheric variability (Brunner et al. 2016). Such fields are used by Brunner et al. (2016) to detect atmospheric blocking. Here, I use them for detecting storm events.

For the ECMWF comparison, six-hourly 2.5°×2.5° ECMWF full field data has been averaged for each day separately.

# 4. Methods

The methods applied in this work are described in the following. To get an overview on the global Equator-to-pole temperature difference, temperature gradients are computed (Sect. 4.1). For a more detailed look, the differences of certain latitude bands are calculated (Sect. 4.2). Based on these data, temperature trends are determined. In addition, the trends for the Atlantic region (60° W to 10° W) and for each season (DJF, MAM, JJA, SON) are calculated. To take the atmospheric temperature variability into account, variability indices are applied in the regression (Sect. 4.4.2). Higher temporally resolved isentropic and pressure surfaces are used for identifying strong storm events (Sect. 4.3). All RO data sets are compared to ECMWF or ERAI data sets.

## 4.1. The Equator to pole temperature gradient

As individual storms extract energy from horizontal temperature differences, changes in the Equator-to-pole temperature gradient may be expected to affect the storm tracks. To investigate how the Equator-to-pole temperature gradient has varied in the 21st century, monthly mean $2.5° \times 2.5°$ RO data from December 2001 to February 2017 are used. To receive a more robust gradient estimate, these data are averaged to 5° zonal bands. Then the temperature derivative from South Pole to North Pole between each zonal band is calculated for each altitude level. The sign of the received South Pole to Equator data is reversed, resulting in a temperature gradient from the Equator to the poles in both hemispheres. After this, the seasonal averages for winter months (December, January and February) and summer months (June, July, August) are calculated. Finally, the temperature gradient anomalies are computed by subtracting the average of all 16 winter/summer seasons from each year's seasonal data.

## 4.2. Area average differencing method

From the gradient data it is obvious that there are regions with relatively strong variation over the years, which mainly occur in the upper troposphere and the stratosphere. Following Harvey et al. (2014), the Equator-to-pole temperature difference is obtained by the following diagnostic: First, the zonal averages for the tropical (30° S to 30° N) and the Arctic (60° N to 85° N) region are calculated as described in Sect. (3.3.2). Then the difference is computed by subtracting the Arctic zonal average from the tropical zonal mean. Note that I focus on the northern hemisphere as Arctic amplification has more impact on this region. For comparison, ECMWF and ERAI full-field temperature anomaly data for the same time period are used.

As many storm events occur the Atlantic region, a separate calculation is accomplished only using grid points between 60° W and 10° W. For storm tracks, the upper stratosphere is not as important as the regions below, so the data are restricted to below 30 km altitude. Regressions (see Sect. 4.4.1) are performed using the Ordinary Least Squares (OLS) or Generalized Least Squares Autoregressive process (GLSAR) model. To reduce the influence of natural variability, variability indices (see Sect. 4.4.2) are applied to the regression. As results, the temporal development of the temperature difference per altitude as well as temperature trends are plotted.

The GLSAR model is applied when the time series is temporally correlated (autocorrelated). Note that this model does not work well for the stratospheric region containing the full Quasi-Biennial Oscillation (QBO) variability. However, after removing the variability by a multiple regression, the GLSAR is well suited. Therefore, I use a full multiple regression with GLSAR for the main results, while I use OLS for the simple linear trend and seasonal trends. A downside of using the OLS model when autocorrelation is present is the underestimation of the trends significance. I therefore do not depict trend significance when showing OLS results for monthly time series.

To check for specific seasonal differences, temperature trends for all 20° zonal bands in the northern hemisphere are computed for each season separately. Additionally, the difference between the tropical zonal mean and the Arctic zonal average are calculated for the each season too. For the regression, seasonal variability indices are used.

In addition to the temperature data results, trends in geopotential height are computed. Geopotential height fields are available as 2.5°×2.5° monthly mean fields on pressure levels. Accordingly, the variability indices files are regridded to pressure levels by exchanging the altitude dimension with the pressure dimension and interpolating the resulting data onto a pressure grid between 1000 hPa to 10 hPa.

## 4.3. Isentropic surfaces

In my work, I analyze two storm cases, the European windstorm Klaus and the tropical typhoon Haiyan, using RO data. I follow the method of Papritz and Spengler (2015) who used an isentropic framework to identify mid- and high latitude storm tracks with ECMWF data. For this purpose, daily weighted (over 5 days) RO profiles from September 2006 to August 2016 (see Sect. 3.3.3) are taken to calculate the potential temperature $\theta$ for each grid point by utilizing the absolute temperature $t_k$ and the associated pressure $p$ in Eq. (2.4) with the standard surface pressure $p_0 = 1000\,\text{hPa}$ and the ideal gas constant $R = 8.314\,\text{J/molK}$. The specific heat capacity $c_p$ at constant pressure $dP = 0$ is assumed with 29.098 J/molK (Ahrens 1995; Andrews 2000). To get specific isentropic layers, the pressure coordinates are swapped against the potential temperature values at each grid point. The new potential temperature coordinates are then interpolated onto an equidistant vertical grid with 150 grid points between 250 K and 400 K. The six-hourly ECMWF data are processed in the same way. In the end, the geopotential height is plotted on different isentropic levels between 290 K and 310 K. For comparison, the geopotential height anomalies are calculated as the deviations of the daily geopotential height at 850 hPa from the monthly mean geopotential height.

## 4.4. Multiple linear regression

### 4.4.1. Generalized least squares model with auto regression

For the trend estimation a Generalized Least Squares Autoregressive process (GLSAR) is used. Classical regression models try to determine the relationship between the independent and the dependent variable. Rawlings et al. (1998) defines a standard regression model as

$$\mathbf{y} = \mathbf{X}\boldsymbol{\beta} + \boldsymbol{\epsilon} \tag{4.1}$$

with $\mathbf{y}$ as the $n \times 1$ response vector; $\mathbf{X}$ as a $n \times p$ model matrix and $\boldsymbol{\beta}$ as a $p \times 1$ vector of parameters to estimate. $\boldsymbol{\epsilon}$ is an error term and in an OLS model it is assumed to be normally distributed $N_n(0, \sigma^2)$ with $\sigma^2$ as the variance. This leads to an estimator of $\boldsymbol{\beta}$,

$$\mathbf{b}_{\mathrm{OLS}} = \left(\mathbf{X}'\mathbf{X}\right)^{-1}\mathbf{X}'\mathbf{y} \tag{4.2}$$

with a covariance matrix

$$\mathrm{Var}(\mathbf{b}_{\mathrm{OLS}}) = \sigma^2\left(\mathbf{X}'\mathbf{X}\right)^{-1} \tag{4.3}$$

In a linear regression model, certain assumption are made including linearity, homoscedasticity, normality and no auto correlation between the error terms. If the assumption of a missing correlation in the error term is violated, the underlying model would be invalidated, distorting the standard errors of the parameters. If the errors are correlated, the least squares estimators are inefficient and the estimated variance is inappropriate (Gershenfeld 1999; Fox 2002; Akpan and Moffat 2018). An attempt to overcome this weakness is to generalize the OLS, assuming a more universal $\boldsymbol{\epsilon} \sim N_n(0, \boldsymbol{\Sigma})$ with a symmetric and positive-definite error-covariance matrix $\boldsymbol{\Sigma}$. The different diagonal entries in $\boldsymbol{\Sigma}$ correspond to non-constant error variance, while nonzero minor diagonal entries correspond to correlated errors. If the $\boldsymbol{\Sigma}$ is known, the log-likelihood for the model would be

$$\ln(L(\boldsymbol{\beta})) = -\frac{n}{2}\ln(2\pi) - \frac{1}{2}\ln(\det\boldsymbol{\Sigma}) - \frac{1}{2}(\mathbf{y} - \mathbf{X}\boldsymbol{\beta})'\boldsymbol{\Sigma}^{-1}(\mathbf{y} - \mathbf{X}\boldsymbol{\beta}) \tag{4.4}$$

which is minimized by the Generalized Least Squares (GLS) estimator of $\boldsymbol{\beta}$,

$$\mathbf{b}_{\mathrm{GLS}} = \left(\mathbf{X}'\boldsymbol{\Sigma}^{-1}\mathbf{X}\right)^{-1}\mathbf{X}'\boldsymbol{\Sigma}^{-1}\mathbf{y} \tag{4.5}$$

and a covariance matrix

$$\mathrm{Var}(\mathbf{b}_{\mathrm{GLS}}) = \left(\mathbf{X}'\boldsymbol{\Sigma}^{-1}\mathbf{X}\right)^{-1} \tag{4.6}$$

Most of the time, the error-covariance matrix $\boldsymbol{\Sigma}$ is not known and must be estimated from the data along with the regression coefficients $\boldsymbol{\beta}$. Assuming a stationary process generating the regression error and that the covariance of two errors only depends upon their separation (s) in time, it follows that (Fox 2002; Akpan and Moffat 2018):

$$\mathrm{Cov}(\epsilon_t \epsilon_{t+s}) = \mathrm{Cov}(\epsilon_t \epsilon_{t-s}) = \sigma^2 \rho_s \tag{4.7}$$

where $\rho_s$ is the error autocorrelation at lag s. This leads to an error-covariance matrix with the following structure:

$$\boldsymbol{\Sigma} = \sigma^2 \begin{pmatrix} 1 & \rho_1 & \rho_2 & \cdots & \rho_{n-1} \\ \rho_1 & 1 & \rho_1 & \cdots & \rho_{n-2} \\ \rho_2 & \rho_1 & 1 & \cdots & \rho_{n-3} \\ \vdots & \vdots & \vdots & \ddots & \vdots \\ \rho_{n-1} & \rho_{n-2} & \rho_{n-3} & \cdots & 1 \end{pmatrix} = \sigma^2 \rho \tag{4.8}$$

Hence, if the values of $\sigma^2$ and $\rho_s$ are known, it is possible to use this result to find the GLS estimator of $\boldsymbol{\beta}$ in a time series regression. But in general, these parameters are unknown. The large number $(n-1)$ of different $\rho_s$ makes their estimation impossible without specifying additional structure for the autocorrelation. There are several standard models for stationary time-series (Fox 2002). In this work, the most common model is used. It is related to autocorrelated regression errors in the first-order Autoregressive process (AR)(1):

$$\epsilon_t = \phi \epsilon_{t-1} + \nu_t \tag{4.9}$$

where the "random shocks" $\nu_t$ are assumed to be Gaussian white noise, $\mathrm{NID}(0, \sigma_\nu^2)$. Under this model, $\rho_1 = \phi$, $\rho_s = \phi^s$ and $\sigma^2 = \sigma_\nu^2/(1-\phi^2)$. Because, as a correlation, $|\phi| < 1$, the error $\phi_s$ decay exponentially towards 0 as s increases (Fox 2002; Akpan and Moffat 2018).

### 4.4.2. Regression including atmospheric variability indices

In my thesis, I am using a regression model that includes a constant and a linear term as well as main sources of natural variability, such as El Niño–Southern Oscillation (ENSO), QBO and SSW events. The atmospheric temperature variability indices I am using for the regression are based on Wilhelmsen et al. (2018). They provided tropical troposphere and stratosphere indices based on GNSS RO temperature measurements. The input file they worked with included the whole vertical and horizontal information from 2 to 35 km and from 30° S to 30° N. By using an Empirical Orthogonal Functions (EOF) analysis at each altitude level separately, they received a mixture of all variability modes contributing at the respective altitude level, including QBO and ENSO (Wilhelmsen et al. 2018). The variability indices are defined as the main Principal Components (PCs) of the EOF analysis.

For my study, I created in addition variability indices for the Arctic region from 60° N to 85° N to cover SSW events. They are based on the same deseasonalized monthly mean temperature anomaly data as the tropical indices. For the geopotential height indices, I used deseasonalized monthly mean geopotential height anomaly data on pressure levels.

The regression model $\mathbf{y}^{\mathrm{mod}}$ for each grid point $\phi$ and each altitude $a$ is then defined by:

$$\mathbf{y}^{\mathrm{mod}}{}_{\phi,a,t} = \beta^{\mathrm{const}}_{\phi,a} + \beta^{\mathrm{linear}}_{\phi,a}\, t + \beta^{\mathrm{trop}}_{\phi,a}\, T_{ind} + \beta^{\mathrm{pol}}_{\phi,a}\, P_{ind} + \epsilon \tag{4.10}$$

where $\beta^{\mathrm{const}}_{\phi,a}$, $\beta^{\mathrm{linear}}_{\phi,a}$, $\beta^{\mathrm{trop}}_{\phi,a}$ and $\beta^{\mathrm{pol}}_{\phi,a}$ are the regression coefficients (generally $\beta_{\phi,a}$ hereafter). $\epsilon$ is an autoregressive function. To get the residuum $r_{\phi,a,t}$, the deseasonalized model is subtracted from the anomaly time series:

$$r_{\phi,a,t} = \mathbf{y}^{\mathrm{ano}}_{\phi,a,t} - \mathbf{y}^{\mathrm{mod}}{}_{\phi,a,t} \tag{4.11}$$

The regression coefficients are determined by a least squares approach

$$\mathrm{RV}_{\phi,a} = \sum_{t} r^2_{\phi,a,t} \xrightarrow{\beta_{\phi,a}} \mathrm{min!} \tag{4.12}$$

where RV is the Residual Variance. Equation (4.12) varies the regression parameter in order to minimize RV. In practice, the GLSAR function in the Python module statsmodels is used.

# 5. Results

This chapter presents the results of the analyses of the data sets introduced in the previous chapters. This includes an analysis of the global temperature gradient variation from 2002 to 2016 as well as a deeper look into the global and Atlantic temperature difference trends between the tropical and the Arctic region for the same time period. Different data sets are compared to each other and the origin of the trend has been analyzed. Seasonal patterns should give information about the temperature trends for each season separately. Using a vertically resolved atmospheric variability index accounting for tropical QBO/ENSO and polar SSW events reduces the uncertainties significantly.

A special focus is given on two storm events in 2009 and 2011. Geopotential height from RO and ECMWF data sets are compared at 850 hPa as well as on 297 K or 304 K potential temperature levels to identify cyclone tracks. This should give information on how well storms can be detected with the available data and if it is possible to locate a shift in the storm tracks in future studies.

## 5.1. Vertical resolved gradients and differences between the tropics and the Arctic

### 5.1.1. Equator-to-pole temperature gradients

As a result of differential radiation effects and air mass transport, large temperature differences between certain areas of the globe exist. Figure 5.1 shows the temperature anomaly gradient from the Equator to the poles in the northern hemispheric winter months based on RO data. Each year is plotted separately. There are large gradient variations in the higher northern latitudes between 10 km and 30 km altitude. Especially the years 2001/02, 2002/03, 2003/04, 2005/06, 2008/09, 2009/10 and 2012/13 show a strong warming gradient with more than 2 K in the lower stratosphere over the Arctic region, while 2004/05, 2010/11, 2013/14 and 2015/16 present the opposite. The strong warming gradient corresponds well with SSW events determined from zonal wind data[2] at 60° N latitude. In 2004/05, 2010/11 and 2015/16, extreme ozone depletion happened in the Arctic stratosphere, resulting in a strong polar vortex and record breaking negative temperatures that are visible in Fig. 5.1 (Hobe et al. 2006; Arnone et al. 2012; Voigt et al. 2018).

---

[2] retrieved from http://acdb-ext.gsfc.nasa.gov/Data_services/met/ann_data.html, last visit Oct 25, 2018

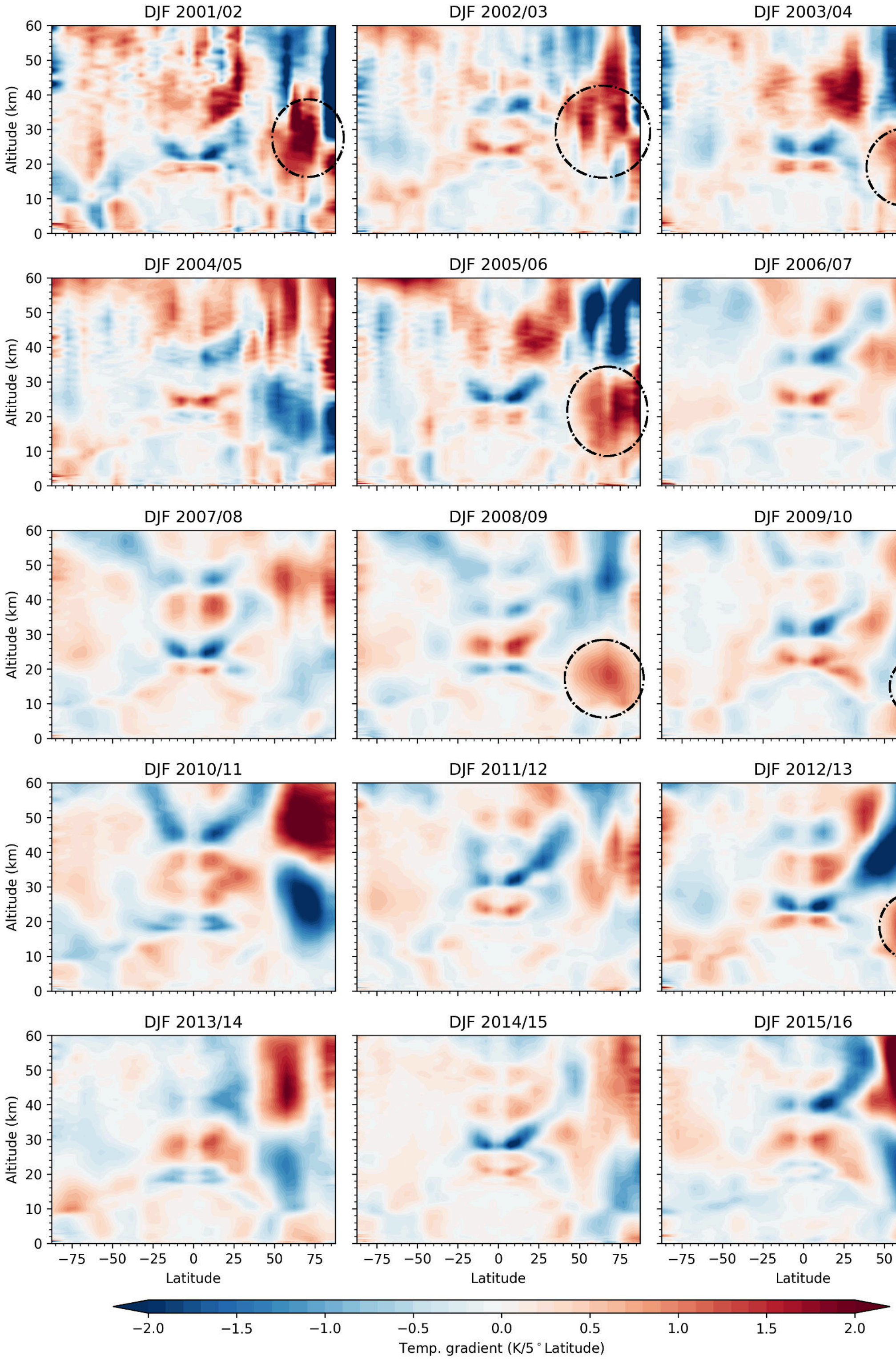

**Figure 5.1.:** Equator-to-pole temperature gradient for the winter season (December, January, February). RO anomaly data from 2002–2016 on a 5° resolution grid. SSW events are marked with a black circle.

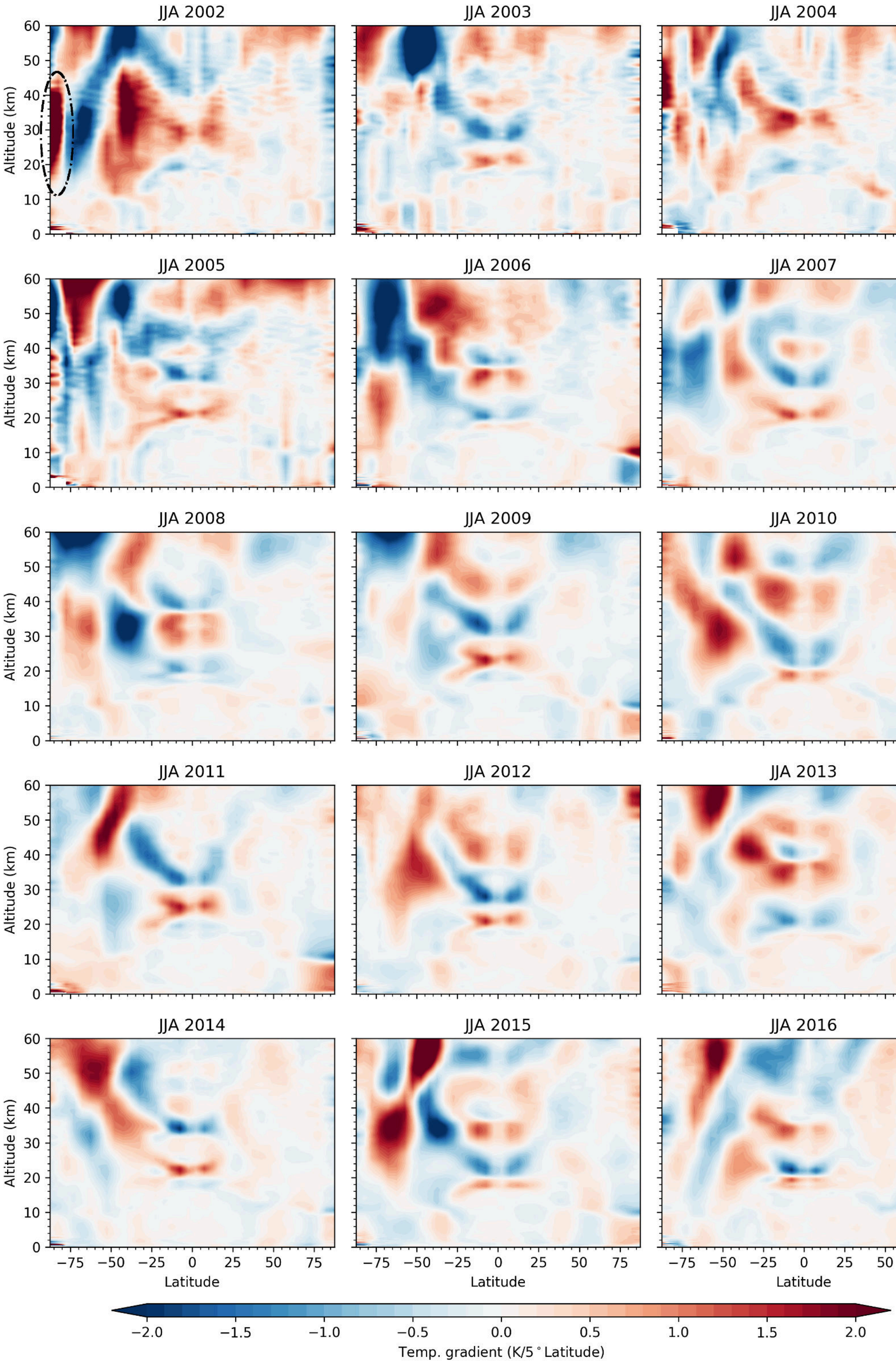

**Figure 5.2.:** Equator-to-pole temperature gradient for the summer season (June, July, August). RO anomaly data from 2002–2016 on a 5° resolution grid. SSW events are marked with a black circle.

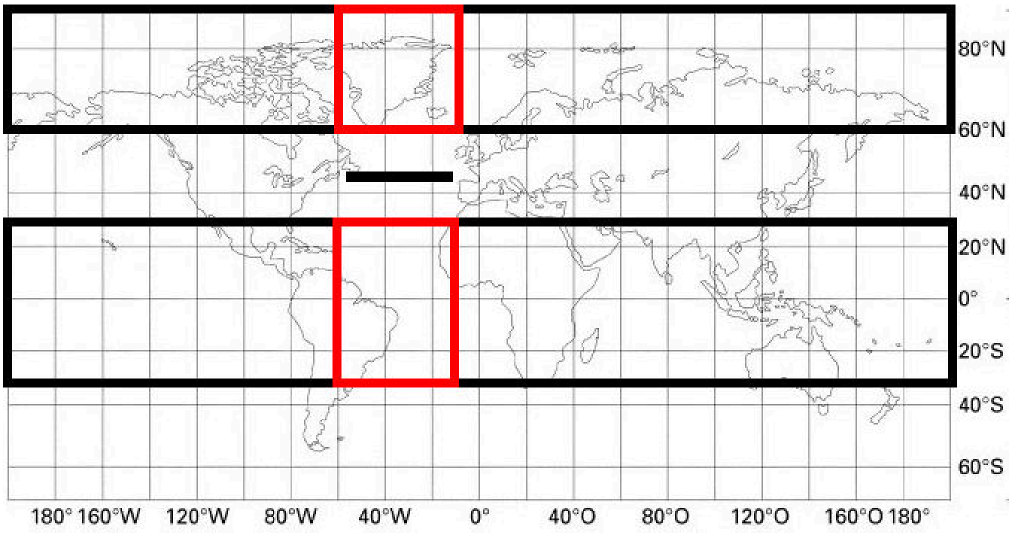

**Figure 5.3.:** Regions used for the calculation. The tropic (30° S to 30° N) and Arctic (60° N to 85° N) latitude bands are drawn as black rectangles. The Atlantic areas that were chosen for the calculations are denoted by red rectangles.

The air masses in the Arctic above 30 km change in the complete opposite way as below. The temperature gradient in these air layers is strongly positive in 2004/05, 2010/11, 2013/14 and 2015/16, but negative in 2001/02, 2003/04, 2005/06, 2008/09, 2009/10 and 2012/13. In connection with SSW events, the strong negative gradients around the stratopause are related to a weakening and/or reversal of the dominating eastward directed zonal winds in the mesosphere. The reversal results from the growth of upward propagating transient planetary waves and their non-linear interaction with the zonal mean flow (Kishore et al. 2012). In addition, the chemical composition changes during SSW recoveries, leading to an ozone depletion in the upper stratosphere and the lower mesosphere (Orsolini et al. 2010).

Near the surface the gradient also changes, although the variability there is far weaker than above. In the tropical region between ±25° the main variation occurs around the tropopause. The gradient is around ±1 K, switches signs multiple times per altitude and is nearly symmetrical around the Equator. This is most likely caused by air mass transport through the QBO and the Brewer-Dobson circulation.

Note that there is only a weak temperature anomaly gradient in the Southern Hemisphere in Fig. 5.1 overall due to the stronger solar radiation income in the Antarctic region for the chosen time period. The increase of the sample size after 2005/06 (see Fig. 3.1) is clearly visible in a more accurate resolution in layer differences.

For summer months visible in Fig. 5.2, there are hardly any temperature gradients to observe in the northern hemisphere. Although there is a SSW event visible in 2002. It is the only major SSW event in the southern hemisphere in the 21st century so far.

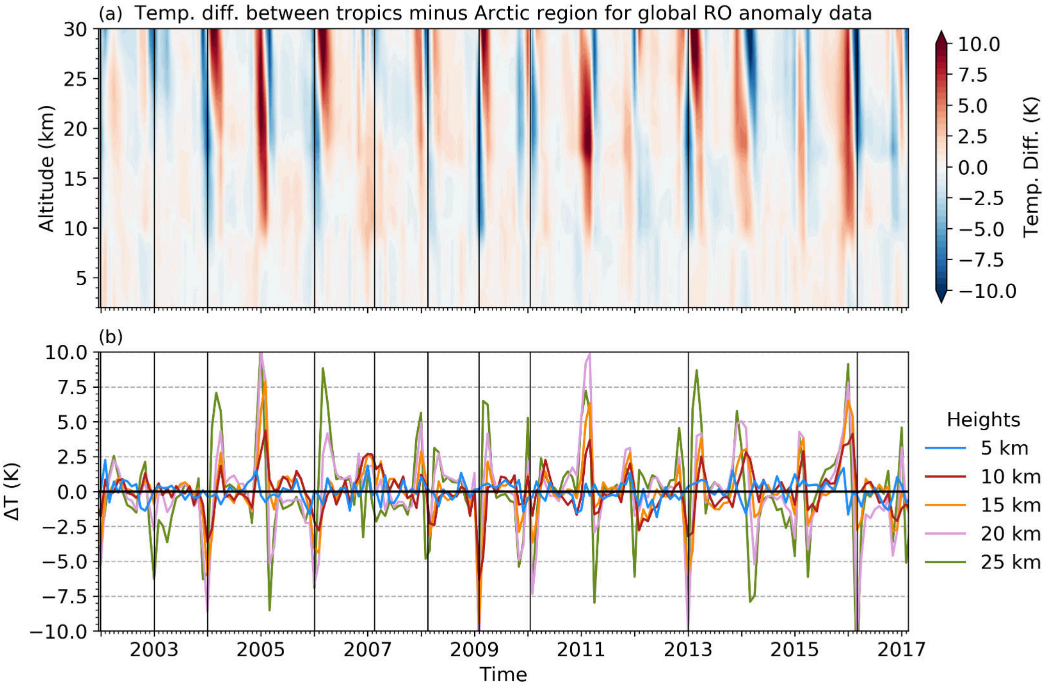

**Figure 5.4.:** (a) Temperature difference between the tropics (30° S to 30° N) minus the Arctic (60° N to 85° N) based on RO temperature anomaly fields. The anomalies are relative to the time period between December 2001 to February 2017. (b) Same data used as (a), trend plotted for specific heights. The black lines indicate SSW events.

### 5.1.2. Temperature anomaly differences over time (2002-2017)

Figure 5.4 presents the temporal evolution in temperature difference between the tropics (30° S to 30° N) minus the Arctic region (60° N to 85° N) (see Fig. 5.3) up to 30 km altitude based on RO temperature anomaly fields. The temperature anomaly differences are generally within ±2 K up to 10 km altitude, and become much larger above. In extreme cases, the temperature anomaly difference can change more than 20 K within a month. The periods of large negative anomaly differences in the lower stratosphere correspond with SSW events. Large positive differences correlate well with cold stratospheric winters, e.g 2004/05, 2010/11 and 2015/16 where large ozone loss took place (Hobe et al. 2006; Arnone et al. 2012; Voigt et al. 2018). The results are consistent with those based on ECMWF (Fig. A.1) and ERAI (Fig. A.2) data sets.

Regressing the anomaly data sets on a vertically resolved atmospheric variability index after Wilhelmsen et al. (2018) reduces the differences significantly (Fig. 5.5). By decreasing the influence of tropical QBO and ENSO variability as well as polar vortex fluctuations with SSW events, the overall minimum and maximum temperature anomaly differences are lowered by more than half. There are still larger peaks at some major SSW events like in 2009 and 2013, but they do not exceed −6 K. Similar

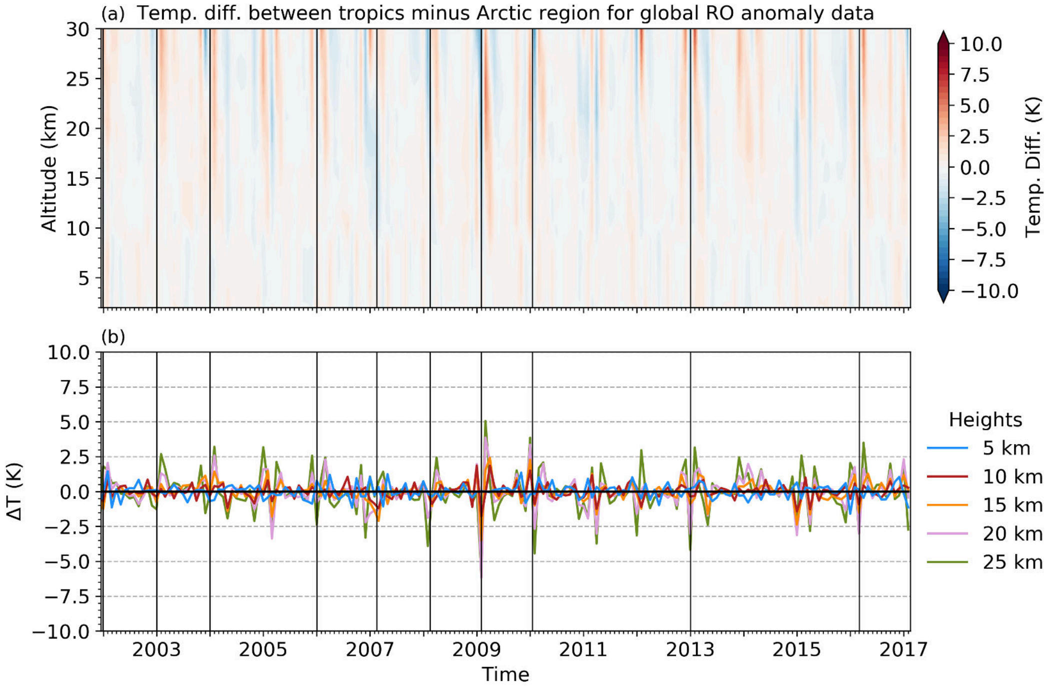

**Figure 5.5.:** Same as Fig. 5.4, but regressed onto a vertically resolved atmospheric variability index after Wilhelmsen et al. (2018) accounting for tropical QBO/ENSO and polar SSW events. The black lines indicate SSW events.

to Fig. 5.4, where the vertically resolved atmospheric variability index had not been used, the temperature differences in Fig. 5.5 variate more in the stratosphere than in the troposphere. The RO results are consistent with other data sets (Fig. A.3, Fig. A.4).

The temporal evolution of temperature differences in the Atlantic region (10° W to 60° W, red rectangles in Fig. 5.3) is more distinct than on the global scale, with temperature anomaly differences larger than ±15 K (Fig. 5.6(a)). The large variations in the 2004/05, 2005/06, 2009/10, and 2013/14 winter months correlate well with SSW events. Using the atmospheric variability index in the regression for the Atlantic region (10° W to 60° W) gives similar results as for the global data set (Fig. 5.6(b)). The differences decrease by more than 10 K for some periods and the anomaly peaks for each altitude level flatten. But still a variation of around ±6 K remains (Fig. 5.6(d)). Other data sets (Fig. A.5, Fig. A.6) provide similar results.

These outcomes suggests that the temporal evolution of the temperature difference between the tropics (30° S to 30° N) minus the Arctic region (60° N to 85° N) is particularly influenced by natural variability resulting from ENSO, QBO and SSW events and a large part of this variability is removed by applying vertically resolved atmospheric variability indices to the regression. The reduction is visible in all data sets and it can be seen in the global mean data as well as in the data for the Atlantic region (10° W to 60° W).

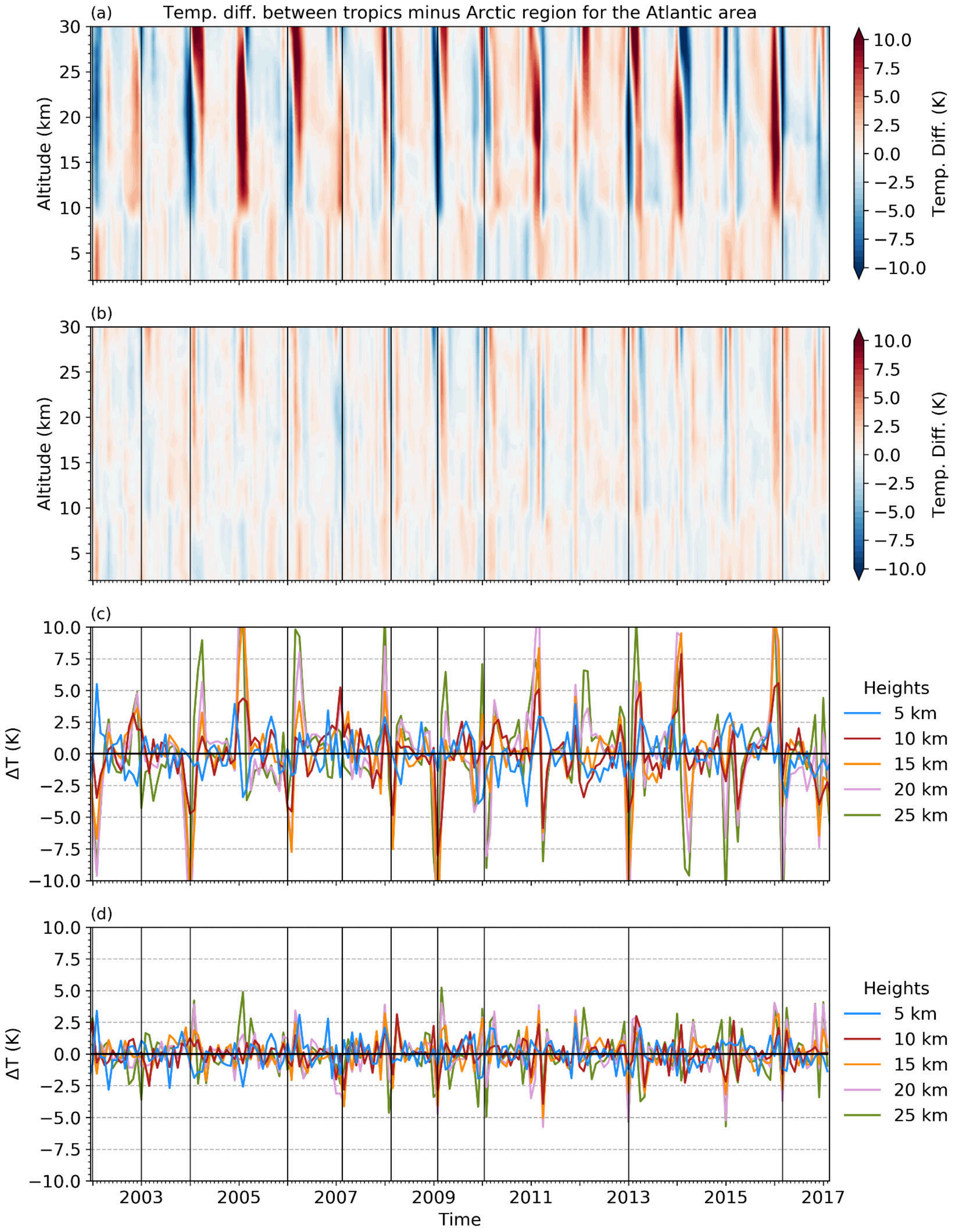

**Figure 5.6.:** (a) Temperature difference between the tropics (30° S to 30° N) and the Arctic (60° N to 85° N) for the Atlantic region (10° W to 60° W) based on RO temperature anomaly fields. The anomalies are relative to the time period between December 2001 to February 2017. (b) The data is regressed onto a vertically resolved atmospheric variability index accounting for tropical QBO/ENSO and polar SSW events. For (c) and (d) the same data as in (a) and (b) are used and the temporal evolution was plotted for specific heights only. The black lines represent SSW events for the same time period.

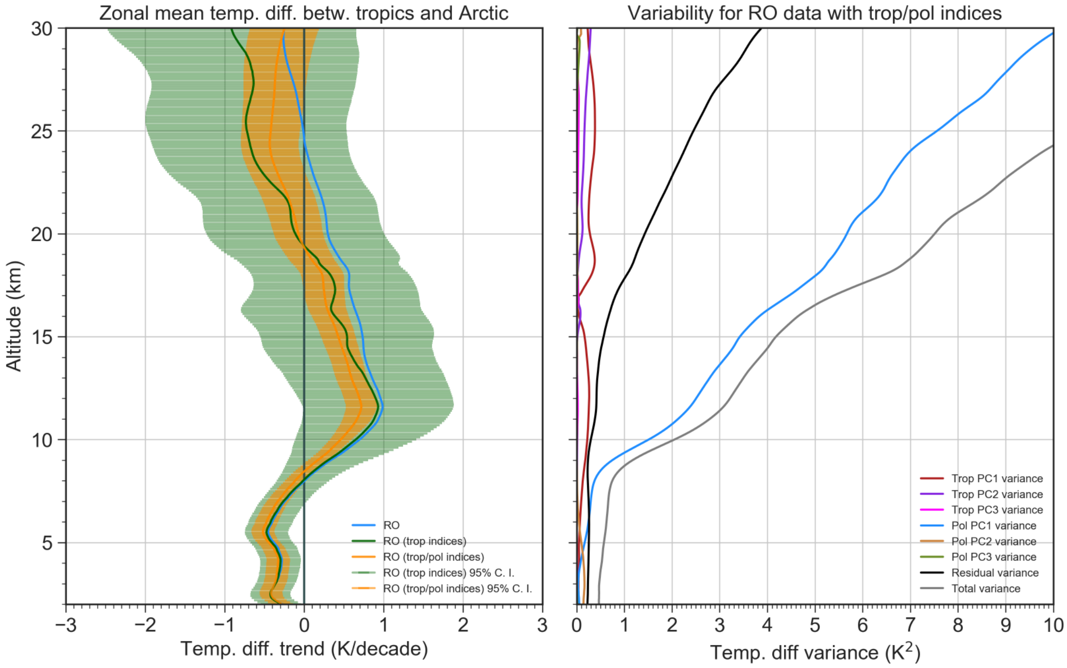

**Figure 5.7.:** Vertically resolved temperature difference trend between the tropics (30° S to 30° N) and the Arctic (60° N to 85° N) based on RO data. Left: The blue line depicts the simple linear trend of sampling error corrected data. The anomaly data was regressed onto a vertically resolved atmospheric variability index accounting for tropical QBO and ENSO (green). In addition, a polar variability index accounting for SSW events (orange) was used. The anomalies are computed relative to the time period from December 2001 to February 2017. Right: Different variability indices in form of PCs explaining the respective variance.

## 5.2. Vertically resolved trends

### 5.2.1. Zonal mean temperature trends

As shown in the previous section, a large part of the variation in temperature difference between the tropics (30° S to 30° N) and the Arctic (60° N to 85° N) exists due to atmospheric phenomena like ENSO or SSW events. Each altitude layer is affected differently. Figure 5.7 demonstrates that there is not only strong short-term variability (Fig. 5.4), but also a background trend in the different atmospheric layers. In the lower troposphere, the temperature difference trend between the tropics and the Arctic decreases between −0.1 K and −0.5 K per decade. This means that either the temperature at the pole has risen or the tropical one has been reduced. At around 8 km the trend becomes positive, up to 0.8 K per decade near 12 km altitude. Above the trend is getting weaker per altitude until 19 km, where it changes back to a negative trend of about −0.4 K per decade up to 30 km. Figure 5.7 shows that regressing the anomaly data onto a vertically resolved atmospheric variability index after Wilhelmsen et al. (2018) reduces the uncertainties dramatically and yields more

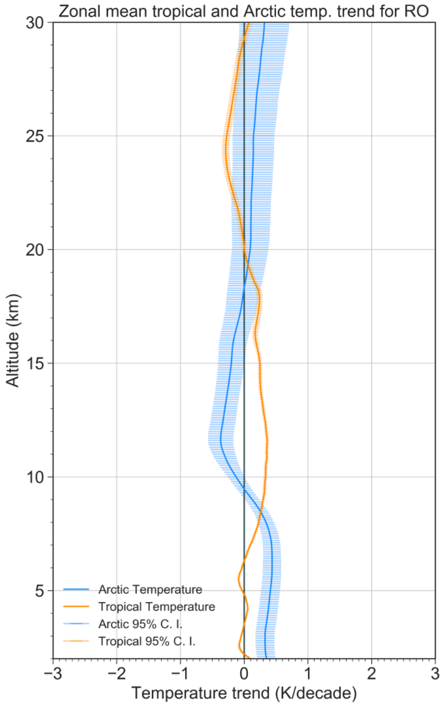

**Figure 5.8.:** Tropical (orange) and Arctic (blue) temperature trend for zonal mean RO data. The data have been regressed onto different variability indices.

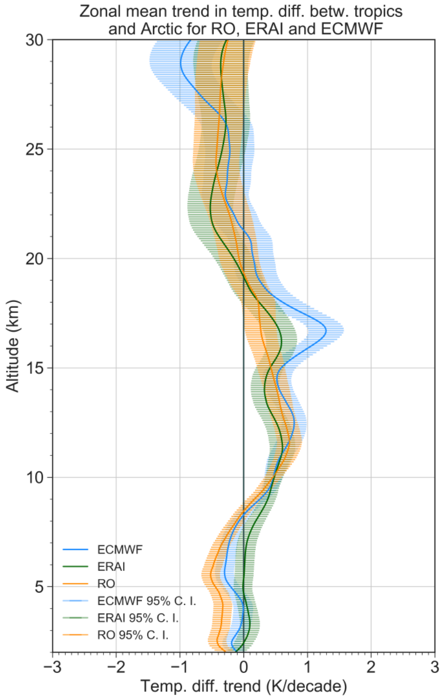

**Figure 5.9.:** Same vertically resolved temperature difference trend as in Fig. 5.7, with both variability indices used, but for RO (orange), ERAI (green) and ECMWF (blue) data sets.

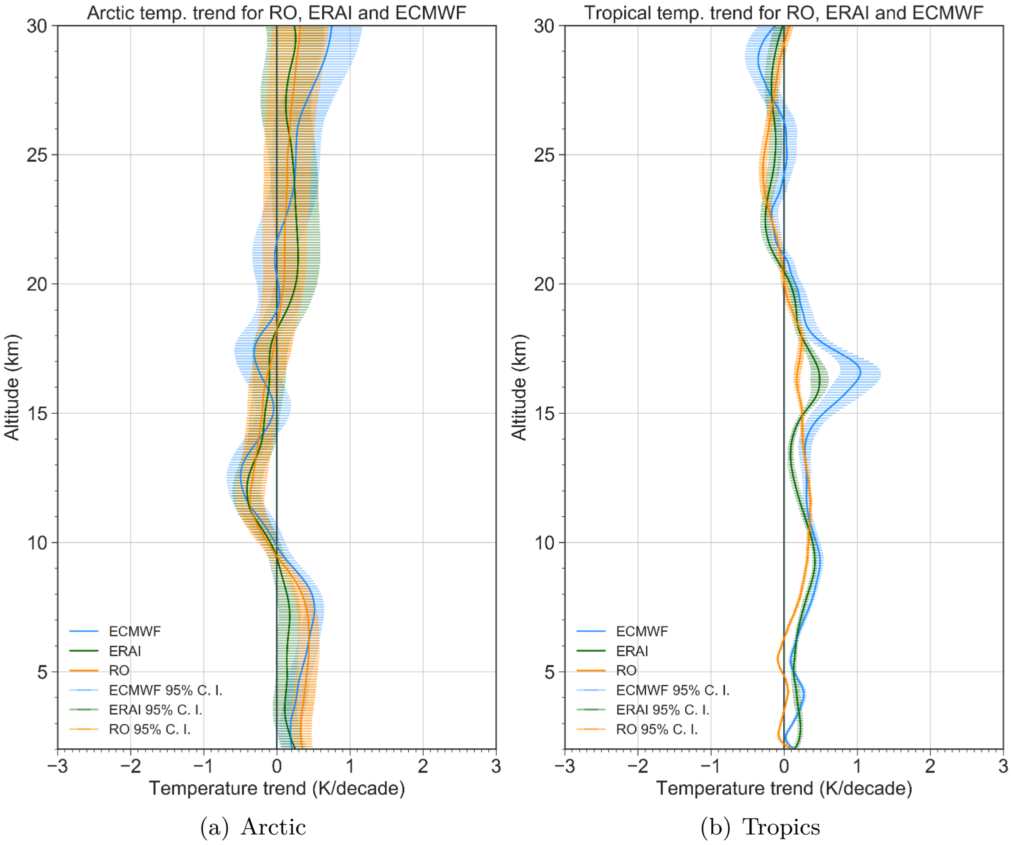

(a) Arctic

(b) Tropics

**Figure 5.10.:** Arctic (60° N to 85° N) temperature trends and tropical (30° S to 30° N) temperature trends for RO (orange), ERAI (green) and ECMWF (blue) data sets. The tropical data have been regressed onto a vertically resolved atmospheric variability index accounting for tropical QBO and ENSO, while the Arctic data have been regressed on a variability index accounting for polar SSW events.

significant results. What stands out in Fig. 5.7 is the large difference between the polar PC1 and the other PCs above 8 km. While the tropical PC1 and PC2 can only explain a small part of the variability in the stratosphere, most of it can be attributed to variability in the polar stratosphere.

Analyzing the temperature anomaly trends for the Arctic (60° N to 85° N) and the tropics (30° S to 30° N) separately gives an explanation for the difference trend in Fig. 5.7. In the Arctic region (Fig. 5.8 and Fig. 5.10(a)) the trend is exactly the opposite to the difference plot with a positive polar trend in RO data at the surface, a negative maximum near 12 km and a positive tendency in the upper stratosphere. This explains the difference trend, as the Arctic temperature anomaly data is subtracted from the tropical one.

In the tropics (Fig. 5.8 and Fig. 5.10(b)), the trend is slightly positive in the lower troposphere, around 0.3 K in the upper troposphere and becomes slightly negative above 20 km altitude for RO data. As the RO temperatures in the moist atmosphere are influenced by ECMWF short-term forecast data in the moist air retrieval, artefacts in the moist tropical troposphere below 8 km arise, resulting in a near to zero trend.

Comparing the RO data with ECMWF and ERAI data in Fig. 5.9 reveals the similar trends overall, but discrepancies between certain layers. The tropospheric trends are negative for the RO and ERAI data sets, with the ERAI becoming zero at 4 km, while the ECMWF trend oscillates around zero between 2 km and 8 km. Above 10 km altitude the ERAI and RO data sets show the same tendency with the ERAI data oscillating around the RO trend.

There is a positive maximum for both in the tropopause region with 0.8 K per decade. The ECMWF trend in the stratosphere is similar, but shows a large peak near 16 km stemming from the representation of the tropical tropopause (see Fig. 5.9).

In the Arctic, ERAI shows a noticeable weaker trend in the troposphere (see Fig. 5.10(a)). Overall ERAI and ECMWF show oscillating structures in the vertical trend which might be due to the underlying model and weighting functions in the assimilation process.

### 5.2.2. Temperature trends and difference trends in the Atlantic region

In addition to the global mean Equator-to-pole temperature difference I also analyzed the temperature difference over the Atlantic region (10° W to 60° W) (see Fig. 5.3) as storms are regularly forming in this area.

The temperature difference between the tropics (30° S to 30° N) and the Arctic (60° N to 85° N) in the Atlantic region shows a slight warming to near zero trend in the lower troposphere up to 5 km altitude (Fig. 5.11). The difference trend increases to about 0.5 K per decade to 0.6 K per decade at 10 km to 15 km altitude. The trend changes to negative values above 19 km with about −1 K per decade near 25 km altitude. Fig. 5.12 shows the corresponding trend values. The mid-to upper troposphere in the tropical Atlantic region warms by about 0.3 K per decade and the lower stratosphere above cools by about −0.2 K per decade. In contrast I found in the high latitude Atlantic region a cooling for the whole troposphere of between −0.1 K per decade to −0.4 K per decade, and a warming in the stratosphere of about 0.7 K per decade near 25 km altitude. For the tropics, I found the trend in the Atlantic region very similar to the global mean trend. For the Arctic region, the trend are of opposite sign in the troposphere, for the Atlantic region it is positive while it is negative in the global mean. This indicates a stable trend for the tropical region around the globe and strong variation in the polar region, especially in the troposphere.

The variability is much higher in the Atlantic region than globally, mainly caused by variation in the Arctic region as explained by the polar PC1 (Fig. 5.11 right). Also the polar PC2 and PC3 do explain a lot more temperature variance than on the global scale.

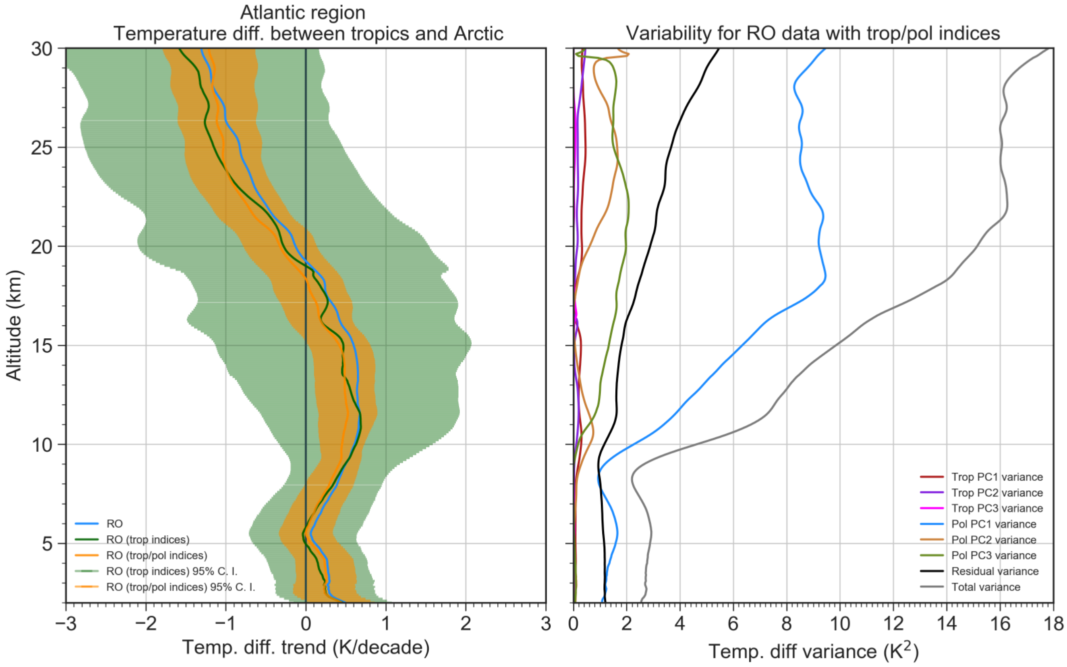

**Figure 5.11.:** Vertically resolved temperature difference trend for the Atlantic region (10° W to 60° W) between the tropics (30° S to 30° N) and the Arctic (60° N to 85° N) for RO data. Left: The blue line depicts the simple linear trend of sampling error corrected data. The anomaly data was regressed onto a vertically resolved atmospheric variability index accounting for tropical QBO and ENSO (green). In addition, a polar variability index accounting for SSW events (orange) was used. The anomalies are computed relative to the time period from December 2001 to February 2017. Right: Different variability indices in form of PCs explaining the respective variance.

The comparison of all data sets in Fig. 5.13 shows larger differences between ERAI and RO data in the lower troposphere. Above 10 km they show a similar trend. The large peak near 17 km and 30 km for the ECMWF data can possibly be explained by the underlying model and data assimilation processes.

The lower to middle tropospheric trend for the polar Atlantic temperature anomaly data (Fig. 5.12 and Fig. 5.14(a)) is shifted by 0.7 K against the global trend in Fig. 5.10(a). While the tendency in the lower stratosphere is nearly the same, it changes to negative further down for the Atlantic data and is far stronger in the mid stratosphere. As opposed to the polar trend, the Atlantic tropical temperature variations shown in Fig. 5.12 and Fig.5.14(b) are the same as for the global data.

Separately analyzing regions over land, ocean, and land-ocean visible in Fig. 5.14(c) and Fig. 5.14(d) leads to the conclusion that there is a strong influence of the Greenland area in the Atlantic region. As there are strong differences in land-ocean distributions between the tropics and the Arctic region, the polar troposphere trend is different in the Atlantic compared with the zonal mean data, while the tropical trends do not differ much as the tropical area data includes a high percentage of

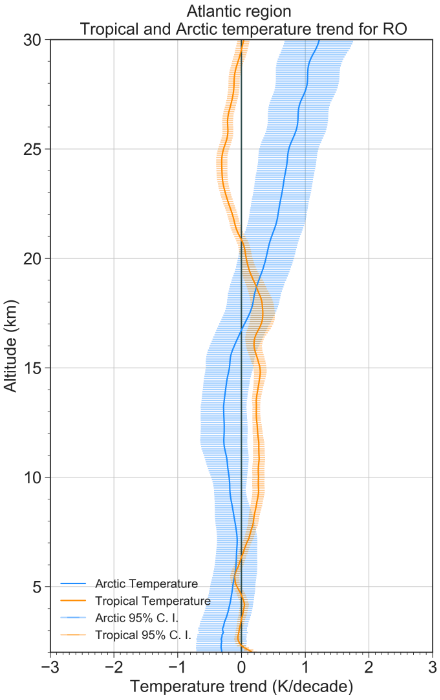

**Figure 5.12.:** Tropical (orange) and Arctic (blue) temperature trend in the Atlantic region for RO data. The data have been regressed onto different atmospheric variability indices.

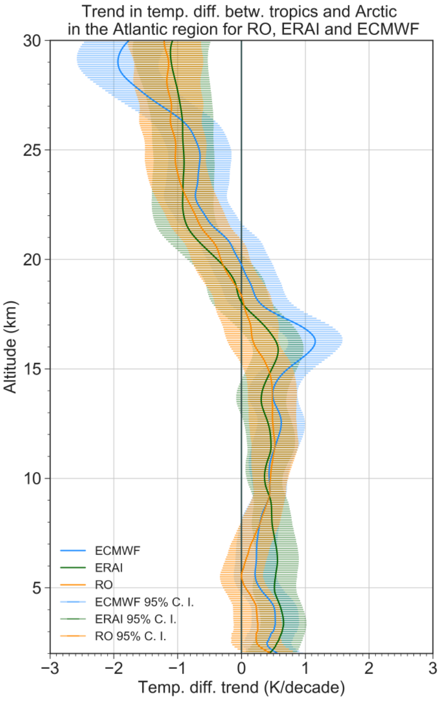

**Figure 5.13.:** Same vertically resolved temperature difference trend as in Fig. 5.11, with both variability indices used, but for RO (orange), ERAI (green) and ECMWF (blue) data sets.

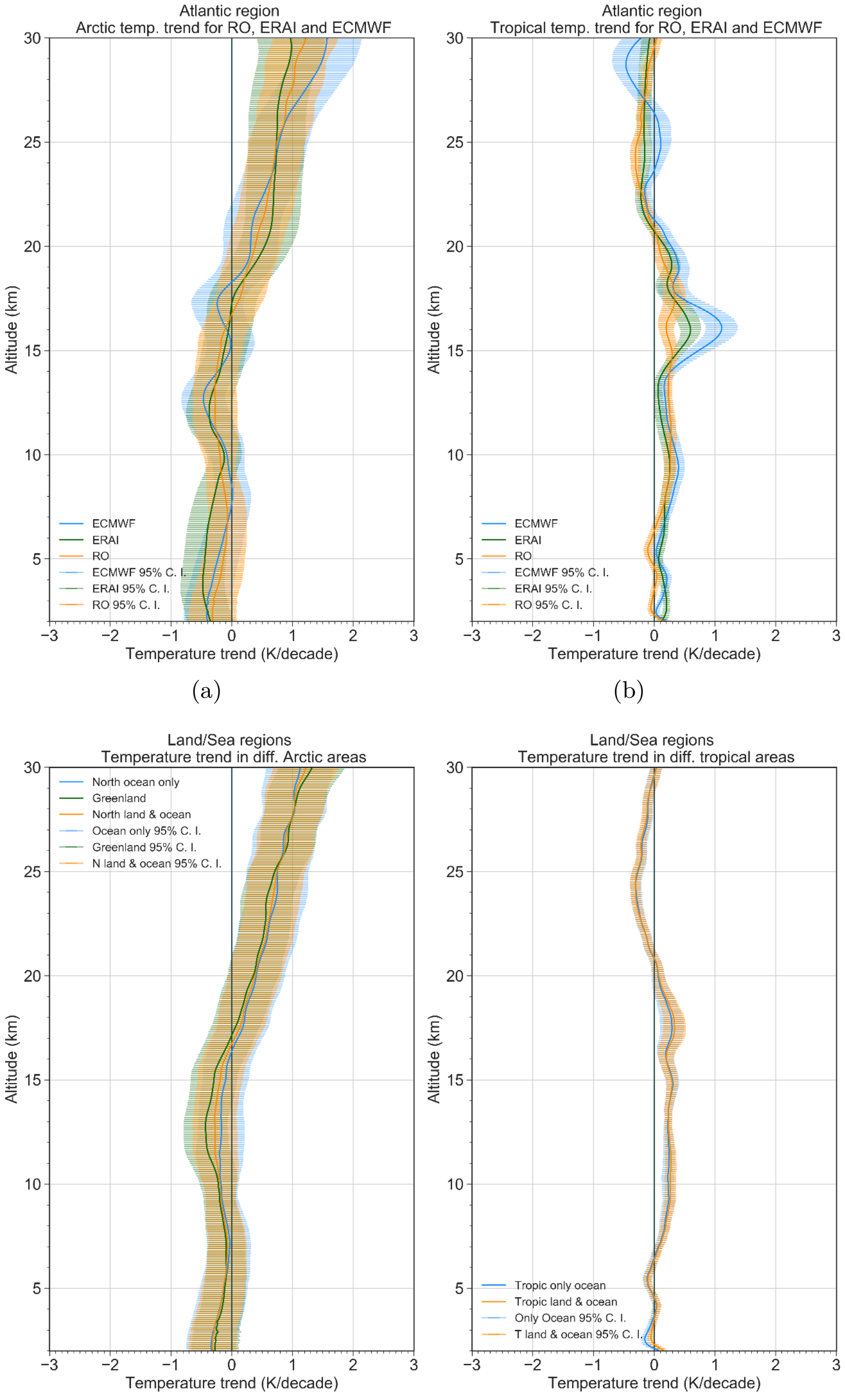

(a) (b)

(c) (d)

**Figure 5.14.:** Top: Comparison of temperature trends in the Atlantic region at high latitudes and in the tropics for RO (orange), ERAI (green) and ECMWF (blue) data sets. Bottom: (c) Comparing Arctic continental and ocean data (blue) with Greenland (green) and ocean only data (orange) for the Atlantic region. (d) Same as (c) but for tropical latitudes comparing land and ocean data with ocean only data. Processed in the same way as Fig. 5.10.

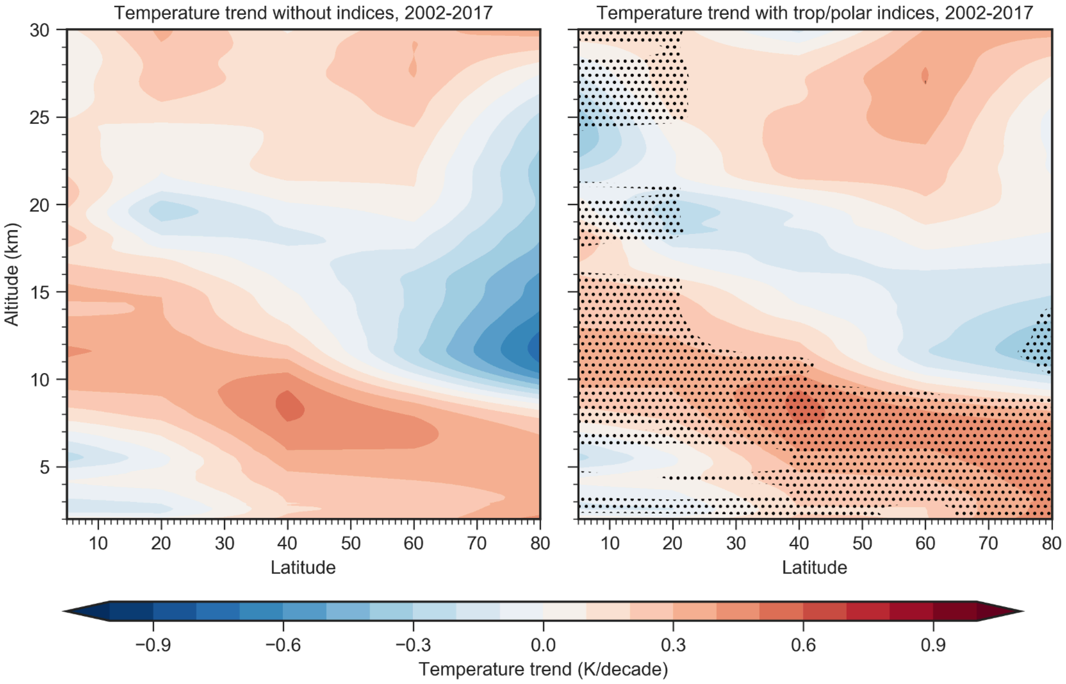

**Figure 5.15.:** Temperature trends in the northern hemisphere for RO data from 2002–2017 on 20° latitude bands. Left: Simple linear trend of the SE corrected anomaly data. Right: The anomaly data have been regressed onto vertically resolved atmospheric variability indices accounting for tropical (QBO and ENSO, 0° to 45°) and polar (SSW, 45° to 90°) variability. Trends, which are significant at the 95 % level, are marked with black dots.

stable ocean areas. Besides this, the tropical region is hardly affected by the seasons and the weather conditions are more stable there.

### 5.2.3. Seasonal temperature trends

Various studies show that seasonal patterns in temperature trends are an important indicator for climate change (Randel et al. 1999; Free 2011; Cohen et al. 2012; Barnes and Screen 2015). In Fig. 5.16, I illustrate the seasonal dependence of temperature trends in the northern hemisphere based on RO temperature anomaly fields. Although the amount of data points that are used for the regression is with 15 seasons on the lower side, the results are in a similar range as the annual trend shown in Fig. 5.15 based on 180 months. While only slight seasonal variation can be recognized in the troposphere applying a simple linear regression in Fig. 5.16 (top 4 panels), large differences in trends are visible in the stratosphere especially between 60° N and 80° N in winter (December, January, February) and spring (March, April, May). Figure 5.16 (bottom 4 panels), shows seasonal trends based on multiple linear regression accounting for tropical and polar variability. The differences in seasonal trends are reduced and the statistical significance of trends in the tropics is increased.

The temperature trends in the tropics are similar in all seasons (see Fig. 5.17 (left) and Fig. 5.18 (left)). There is hardly any trend in the tropics up to 8 km altitude. Note that RO temperature in the moist atmosphere are influenced by ECMWF short-term forecast data used in the moist air retrieval. This leads to artefacts in the moist tropical troposphere below 8 km and results in a near zero trend (same as in Fig. 5.10(b)). Above 8 km the trend becomes positive with a maximum of 0.5 K per decade near 12 km. At around 20 km the trend changes to negative with −0.2 K per decade. All tropical seasonal results correspond well with the annual temperature trend visible in Fig. 5.8 and Fig. 5.10(b).

However, the temperature trends in the region from 60° N to 80° N differ among the seasons in Fig. 5.16 (bottom 4 panels), especially above 25 km. While the trend is positive in spring and autumn (September, October, November), the trend becomes slightly negative in the winter season. In the Arctic stratosphere, a mean warming trend of 0.4 K per decade to 0.7 K per decade is found in spring and autumn at all altitudes. In winter the trend becomes positive above 20 km altitude, while in the summer (June, July, August) the trend is near zero. In the Arctic troposphere, a warming trend of 0.4 K per decade below is shown for all seasons in Fig. 5.17 (right) and Fig. 5.18 (right). A similar trend can be seen in the annual data in Fig. 5.8 and Fig. 5.10(a).

In the mid-latitudes, there are also large differences in seasonal trends visible in Fig. 5.16 (bottom 4 panels). While weak insignificant negative trends with −0.2 K per decade in the lower troposphere and −0.4 K per decade near 25 km are recognizable in the summer season, the opposite is shown for the winter months. Additionally, there is a strong negative peak with more than −1 K per decade at 26 km for the autumn months that can not be identified for other seasons. The reason for this feature is not clear and possibly due to the variability indices being created for tropical and high latitude regions. This is a topic of further investigation.

In summary, these results show that the seasonal trends derived from regression using vertically resolved variability indices are similar in the troposphere and vary in the upper stratosphere, mainly near the Arctic region. The trends stay the same after the variability indices are applied to the regression, only the intensity is reduced in most cases. This is an indication of strong influences from natural variability in form of SSW events which have a massive affect on the seasonal trends.

### 5.2.4. Trend in geopotential height

Figure 5.19 presents the difference trend of geopotential height on pressure levels for RO zonal mean (top, left) and Atlantic (10° W to 60° W) (bottom, left) data sets. The corresponding explaining variability breakdown can be found in the panels on the right side. Applying a vertically resolved atmospheric variability index reduces the uncertainties in certain layers substantially. While indices that account only for tropical variability phenomenons give a small reduction in the confidence interval (green), using an additional index accounting for the polar variability tightens the confidence interval strongly (orange).

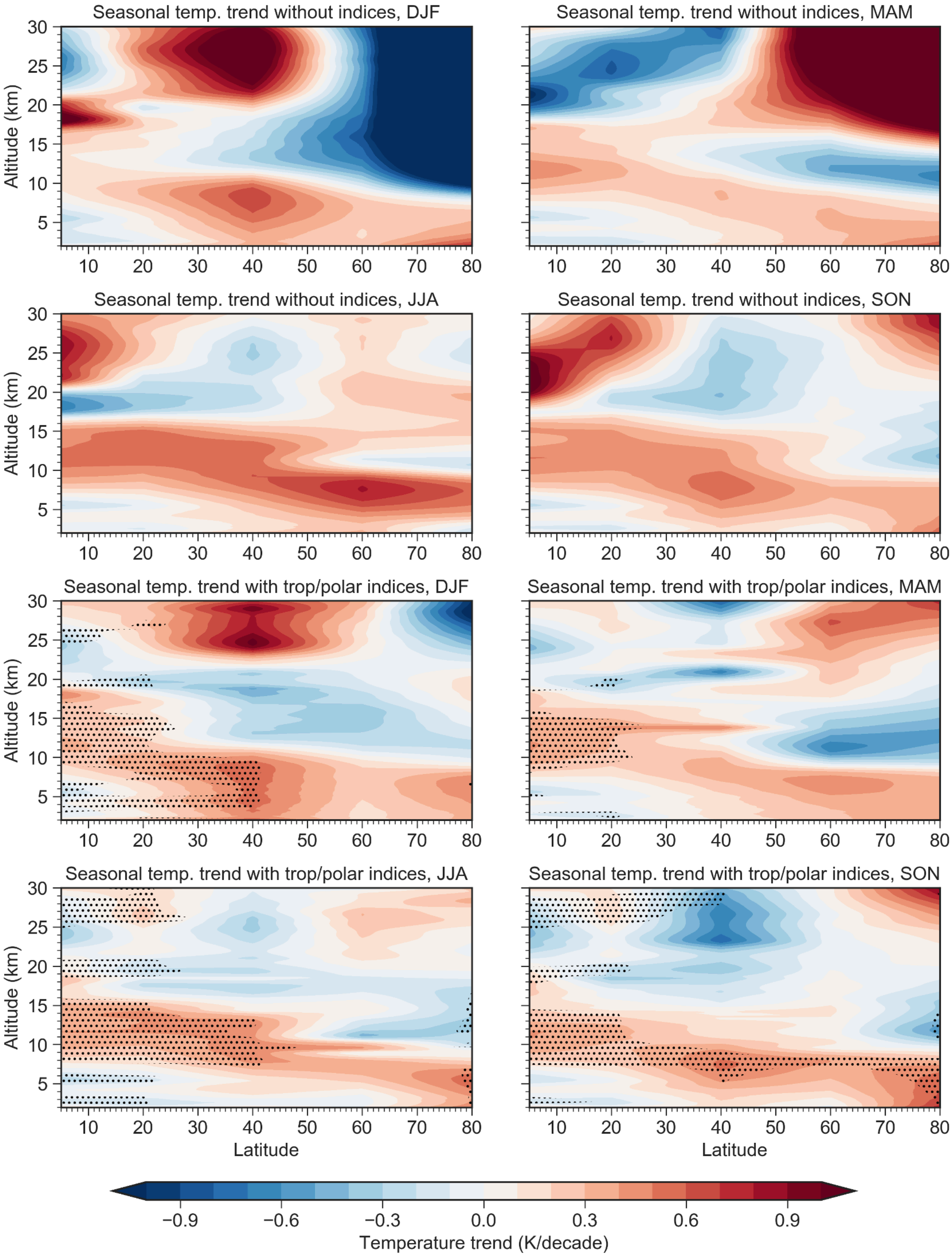

**Figure 5.16.:** Seasonal temperature trends in the northern hemisphere for RO data on 20° latitude bands. Top 4 panels: Simple linear trend for winter (DJF), spring (MAM), summer (JJA) and autumn (SON) RO. Bottom 4 panels: The same seasonal anomaly data as above have been regressed onto vertically resolved atmospheric variability indices accounting for tropical (QBO and ENSO, 0° to 45°) and polar (SSW, 45° to 90°) variability. Trends, which are significant at the 95 % level, are marked with black dots.

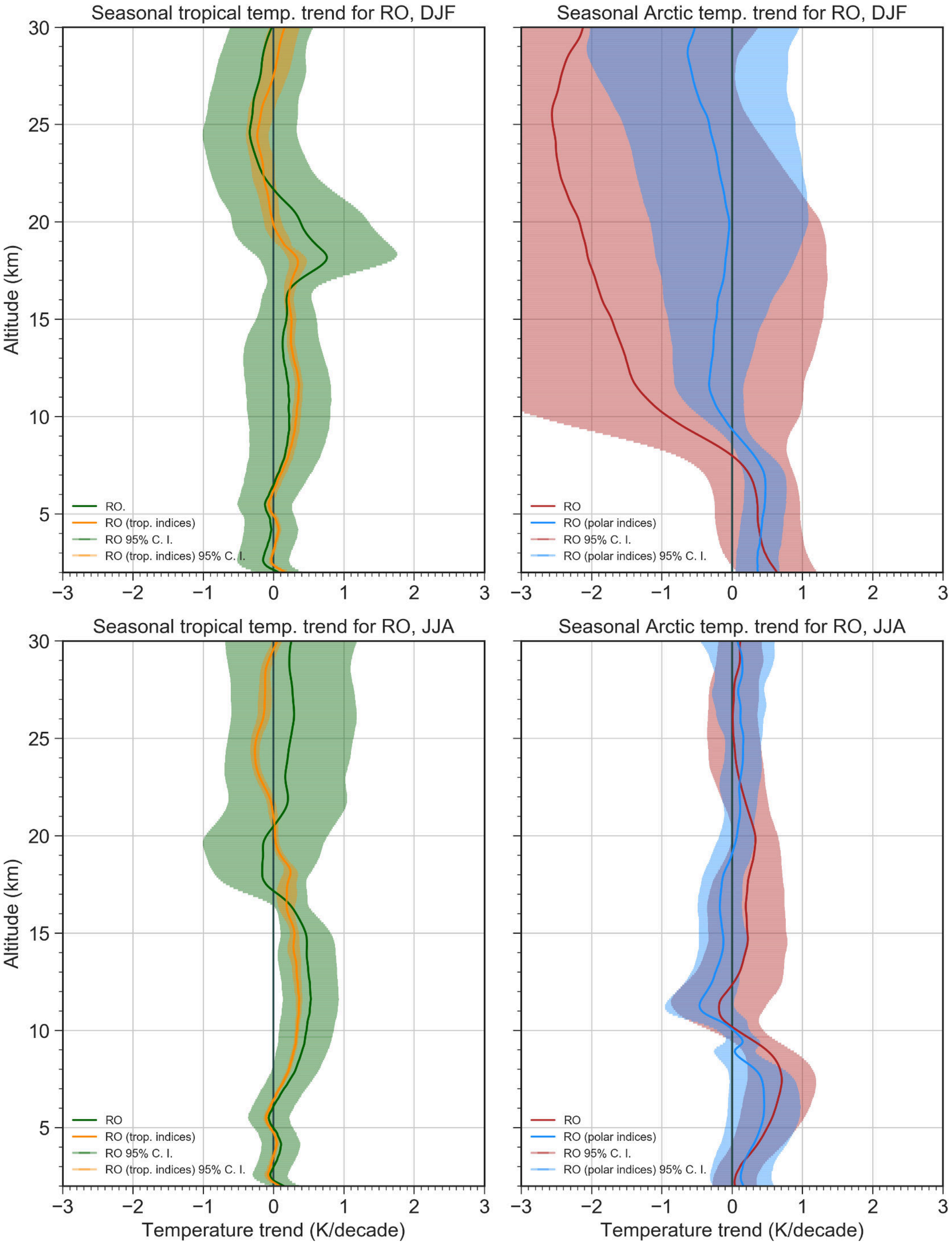

**Figure 5.17.:** Left: Seasonal temperature trends for the tropics (30° S to 30° N). Right: Seasonal temperature trends for the Arctic region (60° N to 85° N). The trends for the winter seasons can be found on the 2 top panels while the trends for the summer season are visible on the 2 bottom panels. The green and red lines depict the simple linear trend. The orange and blue line depict the trend based on multiple linear regression with vertically resolved atmospheric variability indices.

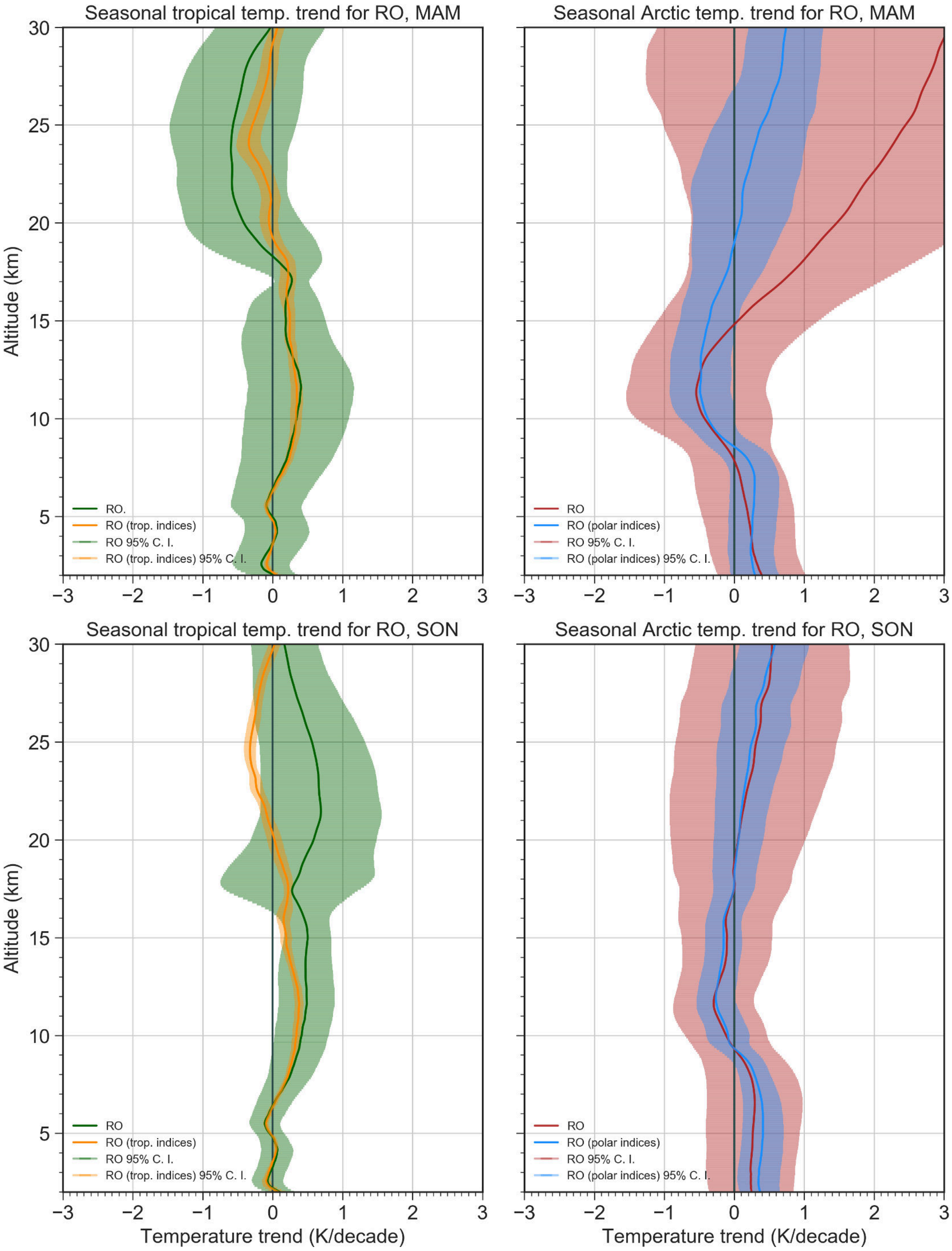

**Figure 5.18.:** Left: Seasonal temperature trends for the tropics (30° S to 30° N). Right: Seasonal temperature trends for the Arctic region (60° N to 85° N). The trends for the spring seasons can be found on the 2 top panels while the trends for the autumn season are visible on the 2 bottom panels. The green and red lines depict the simple linear trend. The orange and blue line depict the trend based on multiple linear regression with vertically resolved atmospheric variability indices.

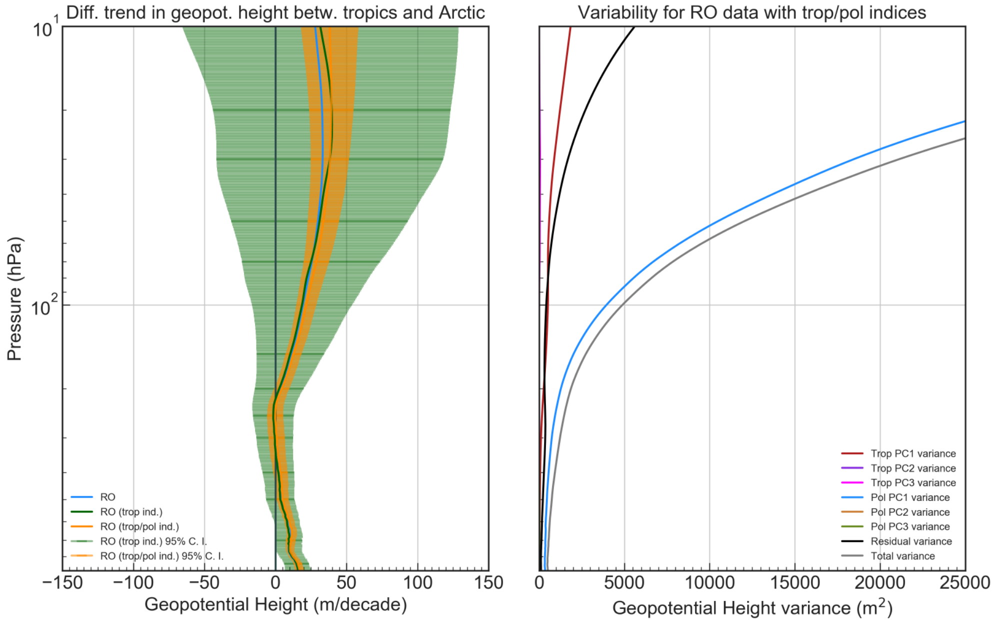

(a) Zonal mean

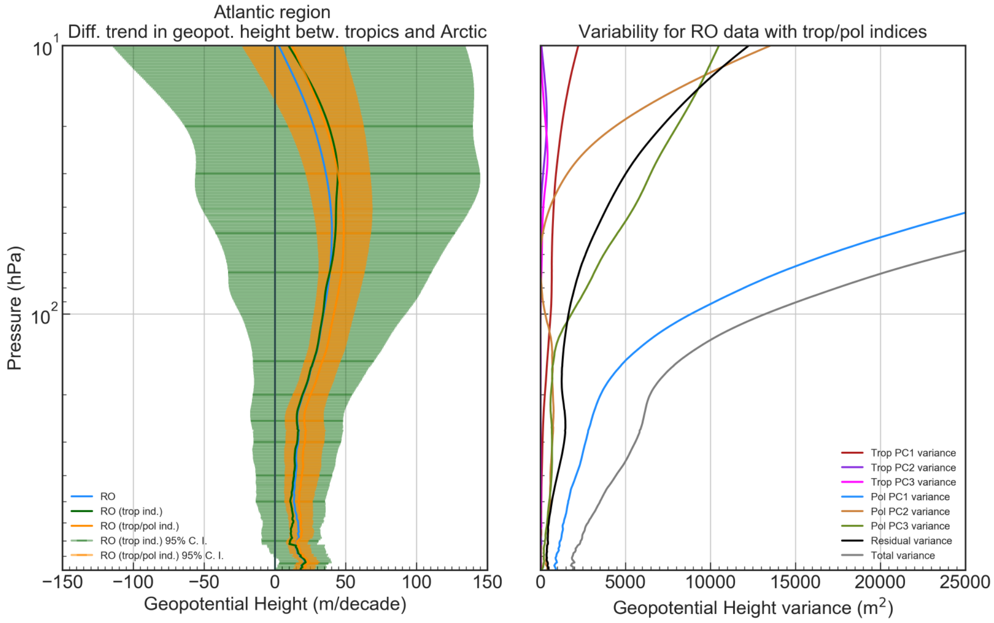

(b) Atlantic region

**Figure 5.19.:** (a) Trend of global geopotential height difference between the tropics (30° S to 30° N) and the Arctic region (60° N to 85° N) for RO data. Left: The blue line depicts the simple linear trend of sampling error corrected anomaly data. The anomaly data was regressed onto a vertically resolved atmospheric variability pressure index accounting for tropical QBO and ENSO (green line) and a polar variability index accounting for SSW events (orange line). (b) Same as (a) but for Atlantic (10° W to 60° W) region. Note that the anomalies are relative to the time period between December 2001 to February 2017. Right: Different variability indices in form of PCs explaining the respective variance.

The data show a positive trend in the geopotential height difference between the tropical (30° S to 30° N) and Arctic region (60° N to 85° N) regions. While ECMWF data present a near to zero trend in the troposphere Fig. A.7(a), a small positive trend of 10 m per decade to 20 m per decade is identified in RO data Fig. 5.19(a). Above 200 hPa the trend increases with height, similar in RO and ECMWF. In the stratosphere, the RO trend is a little bit weaker. Above 40 hPa, it gets more positive after applying both indices to the regression, resulting in a maximum trend of more than 45 m per decade. The ECMWF data show a maximum trend of about 60 m per decade at 20 hPa.

The confidence interval is stronger reduced after applying both variability indices to the regression. An explanation for these results may be found by separately analyzing tropical and Arctic geopotential height trends (Fig. 5.20 and Fig. A.8). In the tropics, there is a significant trend visible in geopotential height for RO data as well as for the ECMWF data. The trend is always positive between 10 m and 30 m per decade. The confidence interval is heavily reduced by accounting for tropical variability indices in the regression.

For the Arctic trend visible in Fig. 5.20 the confidence interval gets wider above 200 hPa when using a simple linear regression. By accounting for polar variability in the regression, the confidence interval is reduced heavily, especially after 200 hPa. The trend is positive in the troposphere with around 5 m per decade and negative in the stratosphere with $-5$ m per decade.

In the Atlantic region a continuous positive tendency between 1000 hPa and 10 hPa is found for both data sets. While the positive trend in the troposphere does not change for the RO data (Fig. 5.19(b)), the positive tendency increases per altitudes for ECMWF (Fig. A.7(b)). The variance between the RO and ECMWF difference trend is small. Same as before, the trends get more pronounced when accounting for variability in the regression. The variability breakdown represents mainly polar variation to explain most variance, with an additional PC3 that may be connected to a “warming hole” in this area.

While the tropical trend in the Atlantic region (Fig. 5.20(d)) is similar to the zonal mean trend (Fig. 5.20(b)), the Arctic trend varies more in the troposphere. The Arctic geopotential height trend is slightly positive in the zonal mean (Fig. 5.20(a)), but slightly negative in the North Atlantic region (Fig. 5.20(c)). Note that geopotential height trends are largely consistent with temperature trends, i.e. warming corresponds with an increasing geopotential height while cooling decreases geopotential height of constant pressure surfaces. In the stratosphere the trend becomes more negative when the polar variability indices are applied to the regression.

It should also be noted that the RO data that are used for this calculations are not SE corrected.

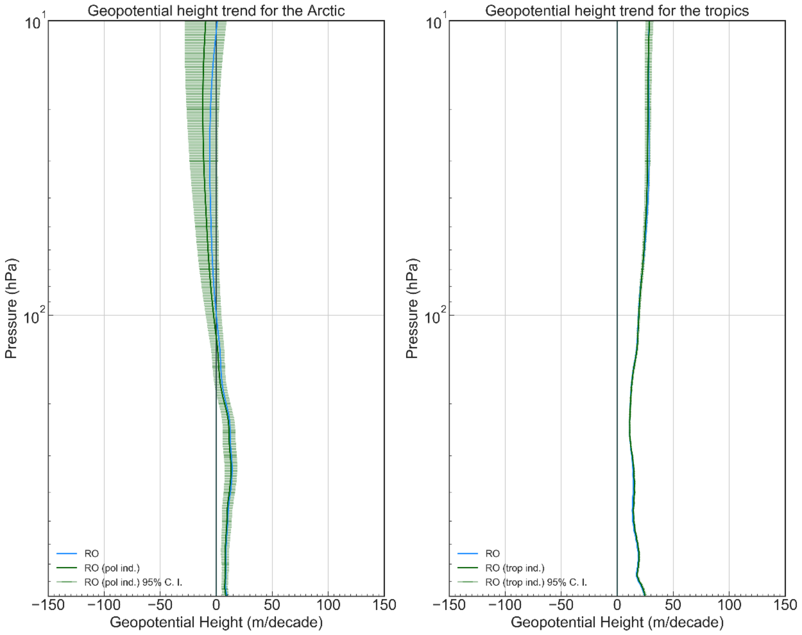

(a) Arctic (b) Tropics

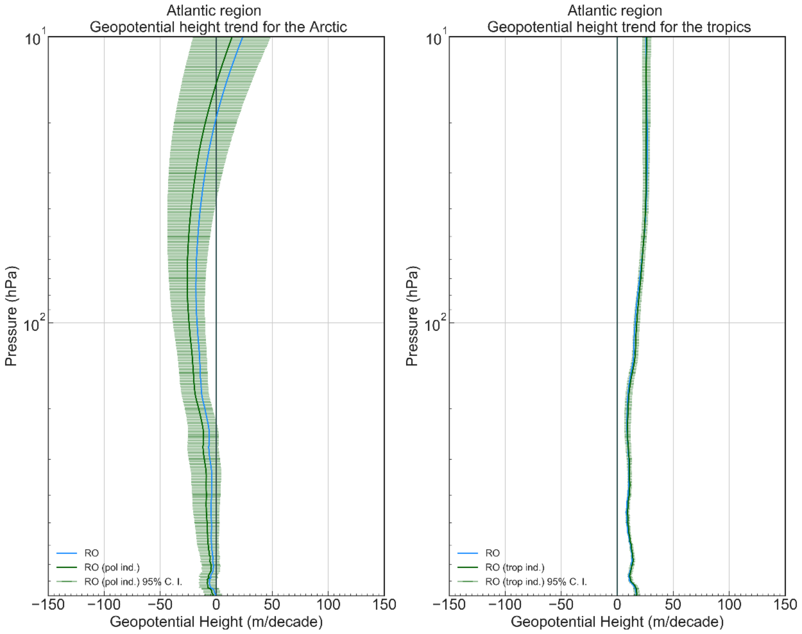

(c) Atlantic, Arctic (d) Atlantic, Tropics

**Figure 5.20.:** Trend in zonal mean geopotential height for (a) the Arctic region (60° N to 85° N) and (b) the tropical region (30° S to 30° S) RO data. The tropical anomaly data have been regressed onto a vertically resolved atmospheric variability index accounting for tropical QBO and ENSO, while the Arctic data have been regressed on a variability index accounting for polar SSW events. (c) and (d) are same as (a) and (b) but for the Atlantic region (10° W to 60° W) only. Note that the anomalies are relative to the time period from December 2001 to February 2017.

## 5.3. Two examples of storm tracking with Radio Occultation

As explained in Sect.2.3, the Equator-to-pole gradient structure is expected to influence the genesis of mid-latitude cyclones. To analyze potential changes in these storm tracks, a precise determination of their locations is required. In this section I use two exemplary storm cases to show how the storm tracks can be analyzed using available RO data and discuss the shortcomings of the present RO event distribution in this context.

### 5.3.1. Extra-tropical cyclone Klaus

The winter storm Klaus shown in Fig. 5.21 and Fig. 5.22 was considered the most damaging wind storm that affected northern Iberia and southern France since the devastating storm Martin in December 1999 (Liberato et al. 2011; Ulbrich et al. 2013). The storms lowest Mean Sea Level Pressure (MSLP) with 965 hPa occurred between 0000 UTC 23 January and 0000 UTC 25 January 2009.

Analyzing the geopotential height anomalies at 850 hPa for the daily RO and ECMWF data in Fig. 5.21, its not possible to identify the storm. A possible explanation for this might be that the resolution in time and space is to low. The cyclone simply moved too fast with gust of winds stronger than $216\,\mathrm{km\,h^{-1}}$ and so the geopotential height anomaly for one day is too blurred. However, what can be identified is a low-pressure system over Iceland. This so-called Iceland low is clearly resolved for for the ECMWF data on the 23 January 2009, but can also be determined in the RO data set on the same day.

Similar resolution problems occurred when the geopotential height was investigated on a 293 K isentropic surface in Fig. 5.22 after Papritz and Spengler (2015). It is not possible to identify any storms. There are also strong differences between RO and ECMWF data. While the RO data set did not change this much between day 1 and day 2, with only a minor variation at the southern storm path, there is huge variability in the ECMWF data. A strong variation at the northern area of the cyclone track can be seen additionally. In all 4 plots the storm path is located at around 2600 m geopotential height.

Increasing the time resolution to six-hourly data intervals (Fig. C.1, Fig. C.2, Fig. C.5, Fig. C.8) shows far better results but as the grid resolution with $2.5°\times2.5°$ is still five times lower than in Papritz and Spengler (2015), the storm is not this well resolved. Nevertheless, it is possible to identify a decrease of geopotential height at 850 hPa in Fig. C.1 and Fig. C.2 of up to 300 m difference to normal conditions for this month. This means that there is a low pressure system moving along the track.

The biggest challenge here is to separate the cyclone from other low pressure fields without knowing the storm path before. This is particularly demanding for the case of storm Klaus shown in Fig. C.5 and Fig. C.8 for the six-hourly data on a 293 K isentropic surface. Storm Klaus only travels onto a small geopotential height range between 1800 m and 2800 m and moves within this geopotential “wave“.

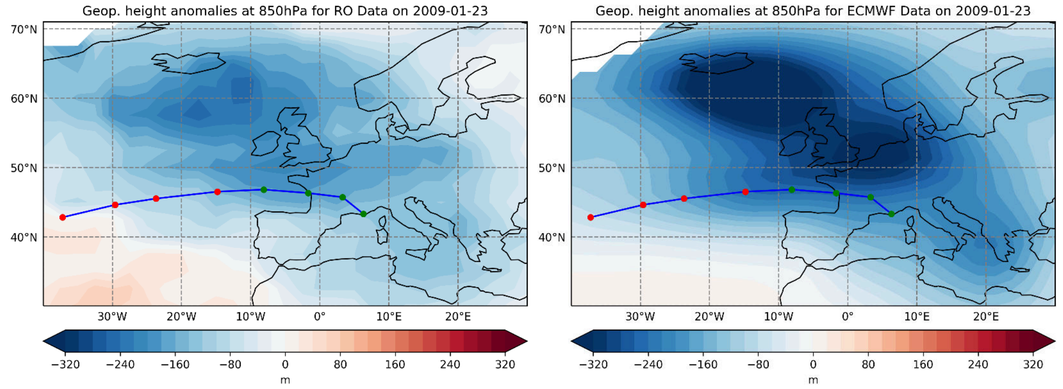
Geop. height anomalies at 850hPa for RO Data on 2009-01-23
Geop. height anomalies at 850hPa for ECMWF Data on 2009-01-23
70°N
60°N
50°N
40°N
30°W
20°W
10°W
0°
10°E
20°E
−320
−240
−160
−80
0
80
160
240
320
m

(a) 01-23 850 hPa RO

(b) 01-23 850 hPa ECMWF

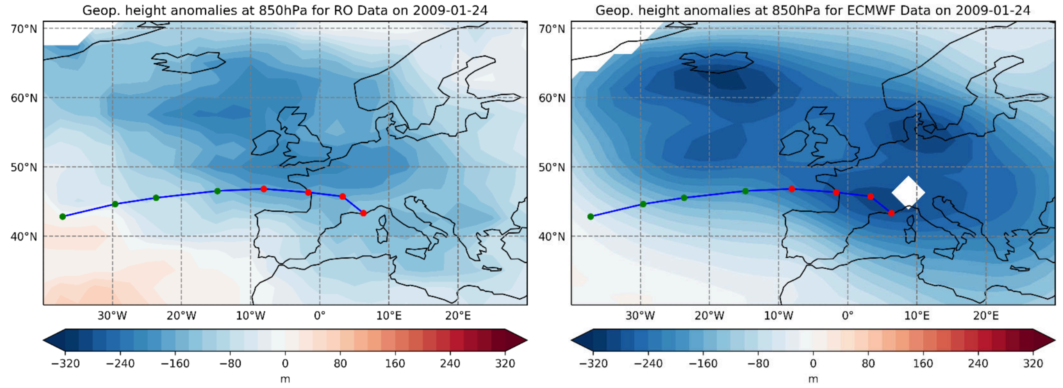
Geop. height anomalies at 850hPa for RO Data on 2009-01-24
Geop. height anomalies at 850hPa for ECMWF Data on 2009-01-24
70°N
60°N
50°N
40°N
30°W
20°W
10°W
0°
10°E
20°E
−320
−240
−160
−80
0
80
160
240
320
m

(c) 01-24 850 hPa RO

(d) 01-24 850 hPa ECMWF

**Figure 5.21.:** Geopotential height anomalies at 850 hPa for RO (right) and ECMWF data (left). Difference between the daily data and the monthly climatological average geopotential height for January from 2006 to 2016. The blue line indicates the surface track of the cyclone Klaus for the time period between 0000 UTC 23 January 2009 (top) and 18 UTC 24 January 2009 (bottom). The position of the storm center in six-hourly intervals is marked with a red dot. Green dots indicate the storm path (Coordinates taken from Liberato et al. (2011)).

### 5.3.2. Tropical cyclone Haiyan

Typhoon Haiyan, known as Super Typhoon Yolanda in the Philippines, shown in Fig. 5.23 and Fig. 5.24 moved much closer to the Equator than winter storm Klaus. This Category 5 (after the Saffir–Simpson hurricane wind scale) cyclone had winds with more than 310 $\mathrm{km\,h^{-1}}$, but the system itself did not travel this fast, so it can be well identified in Fig. 5.23 for RO and ECMWF data. The geopotential height anomalies at 850 hPa between the daily data and the November climatological average from 2006 to 2016 reveal differences up to 100 m. For the ECMWF data sets the low geopotential height system moves exactly along the storm path and increases from 06 November 2013 to 08 November 2013 by nearly 50 m. For six-hourly intervals (Fig. C.3 and Fig. C.4), the typhoon can be detected even better. While the

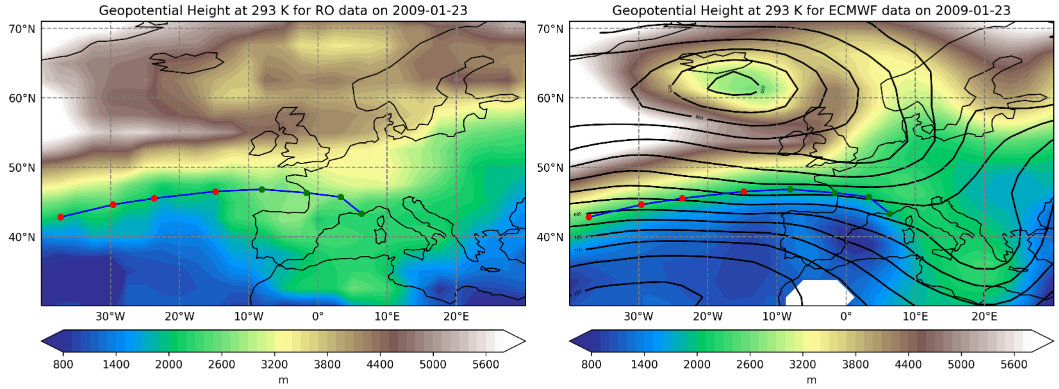
Geopotential Height at 293 K for RO data on 2009-01-23
Geopotential Height at 293 K for ECMWF data on 2009-01-23
70°N
60°N
50°N
40°N
30°W
20°W
10°W
0°
10°E
20°E
800
1400
2000
2600
3200
3800
4400
5000
5600
m

(a) 01-23 293 K RO (b) 01-23 293 K ECMWF

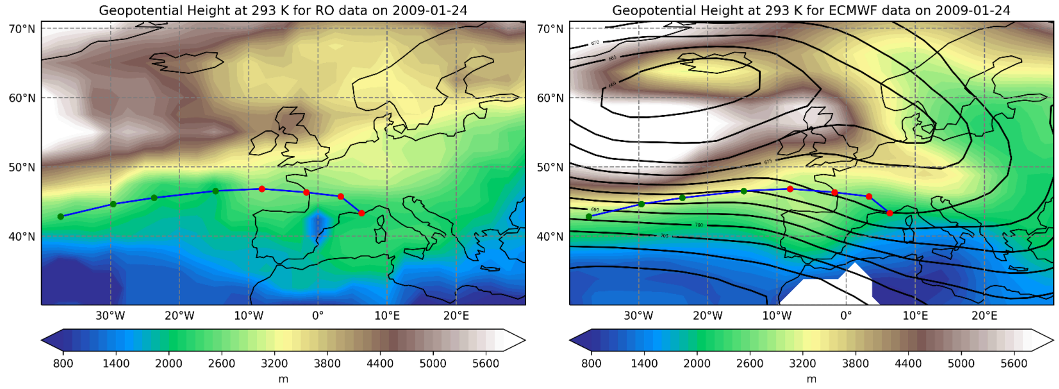
Geopotential Height at 293 K for RO data on 2009-01-24
Geopotential Height at 293 K for ECMWF data on 2009-01-24
70°N
60°N
50°N
40°N
30°W
20°W
10°W
0°
10°E
20°E
800
1400
2000
2600
3200
3800
4400
5000
5600
m

(c) 01-24 293 K RO (d) 01-24 293 K ECMWF

**Figure 5.22.:** Geopotential height at 293 K isentropic surface for RO (right) and ECMWF data (left). Isobars at 3 km are visible as black lines on the right figures. The storm path is the same as in Fig. 5.21.

ECMWF shows good results, the RO data in Fig. 5.23 (left) presents large negative geopotential height anomalies near the cyclone path, so the storm can be detected, but it is not as accurate as with the ECMWF data. The storm location can not be exactly determined as the RO daily data are calculated through a five day average weighting (see Sect. 3.1).

In contrast to the 850 hPa difference, the RO data set gives better information at the 304 K potential temperature surface than the ECMWF data (Fig. 5.24). While there is a low geopotential height system between 900 m and 1100 m north of the cyclone path in RO data, it is hard to identify in ECMWF data where only the isobaric lines denote the cyclone track. Even the six-hourly intervals (Fig. C.7, Fig. C.7) does not give a consistent picture.

Overall, the results show that RO data can be used only for analyzing large slow moving storm systems with current available resolution at isentropic surfaces. For smaller faster moving storm systems the current resolution is to low.

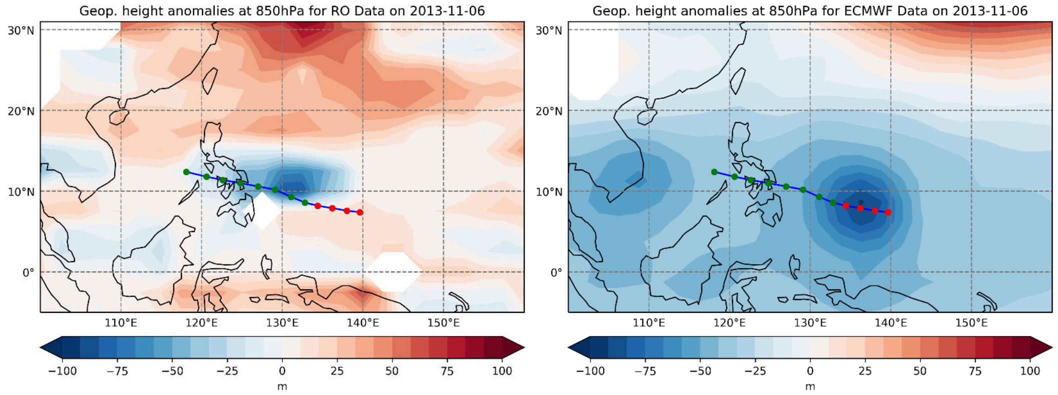
Geop. height anomalies at 850hPa for RO Data on 2013-11-06
Geop. height anomalies at 850hPa for ECMWF Data on 2013-11-06
30°N
20°N
10°N
0°
110°E
120°E
130°E
140°E
150°E
−100
−75
−50
−25
0
25
50
75
100
m

(a) 11-06 850 hPa RO

(b) 11-06 850 hPa ECMWF

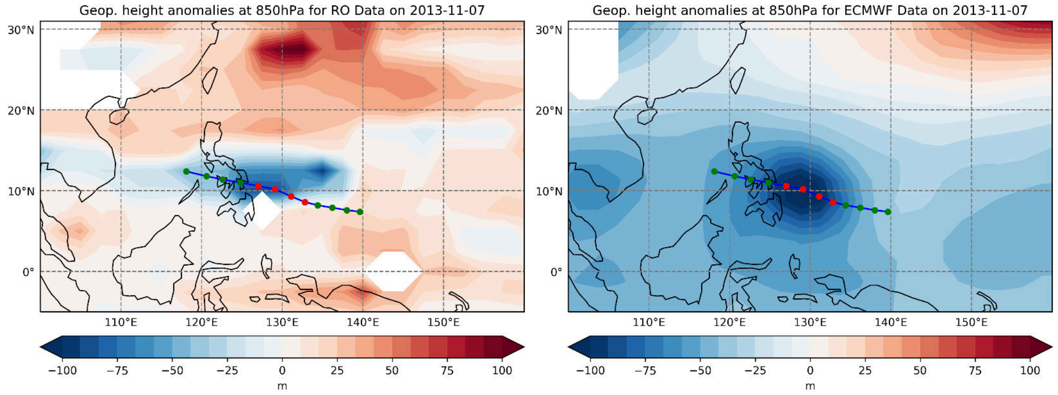
Geop. height anomalies at 850hPa for RO Data on 2013-11-07
Geop. height anomalies at 850hPa for ECMWF Data on 2013-11-07
30°N
20°N
10°N
0°
110°E
120°E
130°E
140°E
150°E
−100
−75
−50
−25
0
25
50
75
100
m

(c) 11-07 850 hPa RO

(d) 11-07 850 hPa ECMWF

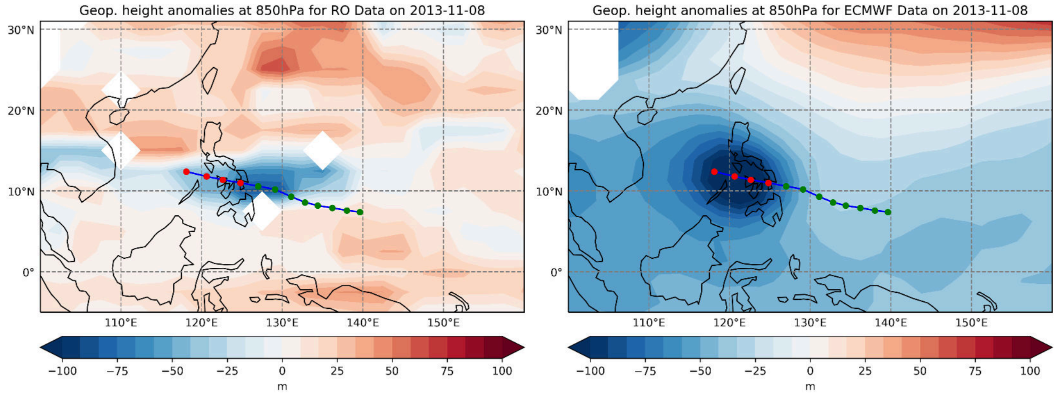
Geop. height anomalies at 850hPa for RO Data on 2013-11-08
Geop. height anomalies at 850hPa for ECMWF Data on 2013-11-08
30°N
20°N
10°N
0°
110°E
120°E
130°E
140°E
150°E
−100
−75
−50
−25
0
25
50
75
100
m

(e) 11-08 850 hPa RO

(f) 11-08 850 hPa ECMWF

**Figure 5.23.:** Geopotential height anomalies at 850 hPa for RO data (right) and ECMWF data (left). Difference between the daily data and the monthly average geopotential height for November from 2006 to 2016. The blue line indicates the surface track of the typhoon Haiyan for the time period between 06 November 2013 (top) and 08 November 2013 (bottom). The position of the storm in six-hourly intervals is marked with a red dot. The green dots indicate the storm path (retrieved from the hurricane and tropical cyclones archive www.wunderground.com/hurricane/hurrarchive.asp, last visit on Sep 21, 2018).

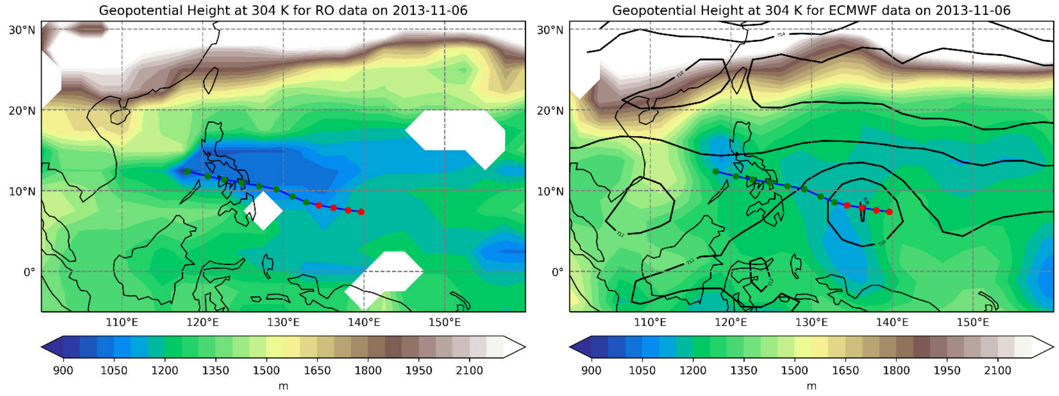
Geopotential Height at 304 K for RO data on 2013-11-06
Geopotential Height at 304 K for ECMWF data on 2013-11-06
30°N
20°N
10°N
0°
110°E
120°E
130°E
140°E
150°E
900
1050
1200
1350
1500
1650
1800
1950
2100
m

(a) 11-06 304 K RO (b) 11-06 304 K ECMWF

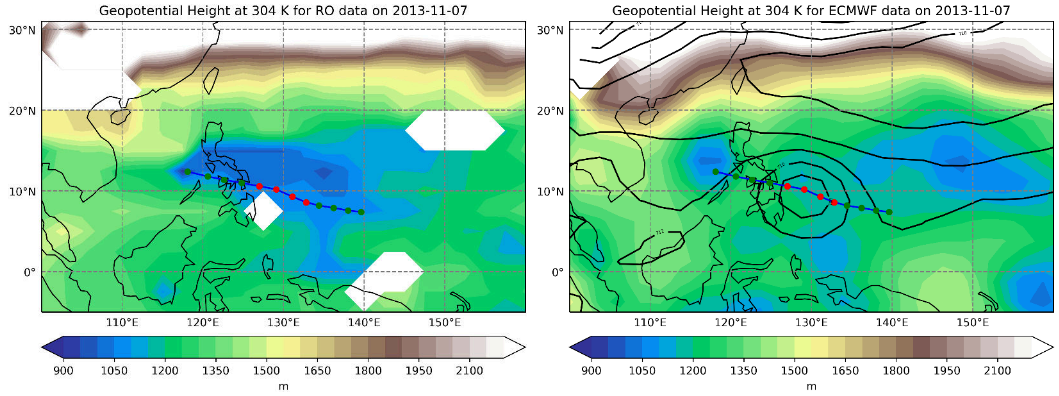
Geopotential Height at 304 K for RO data on 2013-11-07
Geopotential Height at 304 K for ECMWF data on 2013-11-07
30°N
20°N
10°N
0°
110°E
120°E
130°E
140°E
150°E
900
1050
1200
1350
1500
1650
1800
1950
2100
m

(c) 11-07 304 K RO (d) 11-07 304 K ECMWF

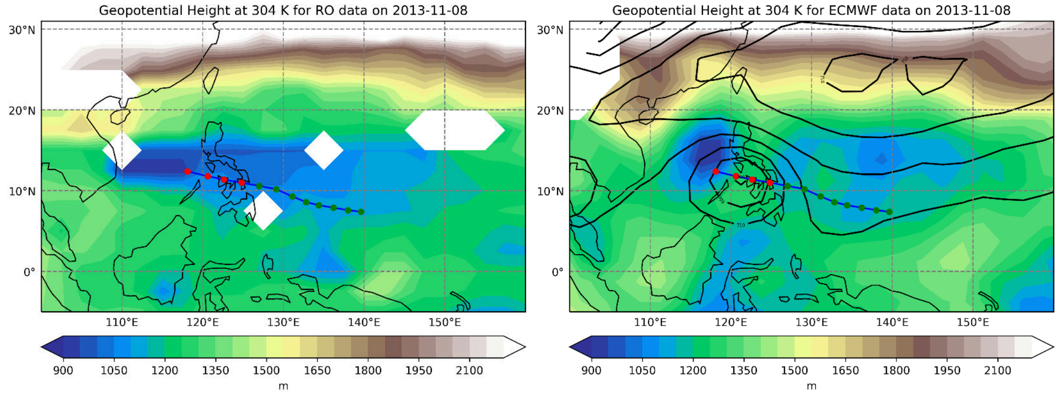
Geopotential Height at 304 K for RO data on 2013-11-08
Geopotential Height at 304 K for ECMWF data on 2013-11-08
30°N
20°N
10°N
0°
110°E
120°E
130°E
140°E
150°E
900
1050
1200
1350
1500
1650
1800
1950
2100
m

(e) 11-08 304 K RO (f) 11-08 304 K ECMWF

**Figure 5.24.:** Geopotential height at a 304 K isentropic surface for RO data (right) and ECMWF data (left). Isobars at 3 km are shown as black lines in the right panels. The storm track is the same as in Fig. 5.23.

# 6. Summary and conclusion

The goal of the present research was to investigate polar amplification and related changes in storm tracks in the period from 2002 to 2017. Through analyzing Radio Occultation (RO) observations it is possible to verify the Arctic amplification trend and its influence on the Equator-to-pole temperature difference at a high vertical resolution. Multiple regression analyses revealed a positive temperature trend in the polar troposphere and a cooling trend in the polar lower stratosphere (Fig. 5.10(a)). These results may be explained by the fact that the melting of sea ice causes less radiation to be reflected at the Earth's surface. Instead it is absorbed by the water there, warming the troposphere after the heat is released later. RO observations and analyses of European Centre for Medium-Range Weather Forecasts (ECMWF) and ERA-Interim (ERAI) data sets showed a similar temperature increase in the troposphere.

The tropical area has a higher tropopause altitude and therefore the positive temperature trend extends nearly up to 18 km (Fig. 5.10(b)). Above a slight cooling is found in the tropical stratosphere. Changes in this region may be responses to a carbon dioxide increase in the atmosphere as well as warming at the surface. The surface warming strengthens the vertical stratospheric circulation, redistributing ozone, which leads to cooling of the lower stratosphere (Lin et al. 2017).

Analyzing the Equator-to-pole temperature difference (Fig. 5.7) showed a negative trend in the troposphere, i.e. the difference between both zonal bands gets smaller, and a positive trend in the lower stratosphere where the differences get larger. These results are in accordance with previous studies demonstrating that polar amplification has weakened the temperature gradient near the surface, while the temperature difference at higher altitudes has strengthened (O'Gorman 2010; Harvey et al. 2014).

In contrast to the global findings, however, the Atlantic region between 10° W and 60° W revealed a different picture of the polar troposphere with a cooling trend up to 18 km (Fig. 5.14(a)). Note that the RO and ECMWF analyses showed less cooling than ERAI below 8 km. The discrepancy between the zonal mean and the Atlantic trend may exist due to the strong influence of the Greenland area in the Atlantic region (Fig. 5.14(c)). A decline in Arctic sea ice exposes the ocean to anomalous surface heat and freshwater flows, leading to positive buoyancy anomalies that weakens the Atlantic Meridional Overturning Circulation (AMOC) and its poleward heat transport. The resulting "warming hole" over south Greenland can be recognized as a negative temperature trend (Stroeve et al. 2014; Rahmstorf et al. 2015; Sévellec et al. 2017). These outcomes also reflect those of AMAP (2017) who found a downward trend in sea ice thickness and extent, land ice volume, and spring snow cover extent and duration. A consequence of these results is the fact that the rest of the polar region has been warming even more for the investigated time period.

In the tropical Atlantic, the temperature trend (Fig. 5.14(b)) is the same as globally (Fig. 5.10(b)) due to the high percentage of stable ocean water in both regions.

Analyzing the temperature difference between the tropics and the Arctic region in the Atlantic (Fig. 5.11) revealed a positive trend in the troposphere and lower stratosphere, i.e. differences get larger. Arctic RO temperature difference trends are smaller between 3 km and 8 km in comparison to the other data sets.

Analyzing the latitudinally resolved trend (Fig.5.15) revealed a warming of the troposphere in all latitudes (90 % significance) and a cooling in the lower stratosphere. A warming is found in the mid-stratosphere at mid- and high latitudes.

Seasonal data in Fig. 5.16 (bottom), Fig. 5.17 and Fig. 5.18 revealed only small differences in seasonal trends, except in the mid-stratosphere. No distinct differences between trends in the winter and summer seasons were found in the investigated period 2002-2017 from observations. Findings based on models (Barnes and Screen 2015) showing stronger changes in Arctic trends in winter than in summer could not be confirmed with the short observational data set.

Nearly all natural signals were detected and removed from the trend by using vertically resolved atmospheric variability indices after Wilhelmsen et al. (2018). According to these data, it can be inferred that polar phenomenons that are connected to the polar vortex have massive effects on the trends' uncertainties either on a global scale or when analyzing only the Atlantic region. The strongest impact is due to Sudden Stratospheric Warming (SSW) events visible in Fig. 5.4 and Fig. 5.6. These events do not only effect the stratosphere, but also influence the lower mesosphere due to enhanced mesospheric ionization with an amplified $NO_X$ influx from the thermosphere (Fig. 5.1) (Shepherd 2014; Feng et al. 2017).

Investigations of geopotential height trends revealed an increase in geopotential height difference between the tropics and the Arctic region among all pressure levels. In the Atlantic region, trends showed the same tendency. When analyzing the tropical and Arctic geopotential height trends separately, the results aligned well with the recent temperature trends, showing similar tendencies and further support the idea of Arctic amplification.

RO delivers excellent information on temperature trends and changes in the Arctic region are clearly visible, however it is very challenging to identify storms and their associated paths. I investigated two prominent storm cases with different characteristics.

The winter storm Klaus was one of the most intense cyclones in the 21st century causing widespread damage across France and Spain. As the storm moved very fast and was small in extent, it could not be discovered in RO or ECMWF daily data (Fig. 5.21, Fig. 5.22). By increasing the time resolution to 6 h intervals, cyclone evolution and pathing can be observed far better, but the storm is still not well resolved in ECMWF analyses (Fig. C.1, Fig. C.2). Overall it was difficult to separate the cyclone from other low pressure fields without pre-information on the storm path.

Nevertheless, it was possible to identify larger and slower moving storms with the available RO data. The tropical typhoon Haiyan that devastated portions of Southeast Asia in 2013 traveled much slower than Klaus. It could be identified in geopotential height anomalies at constant pressure (Fig. 5.23) for RO observations and ECMWF analyses, where the latter data showed a better identification of the cyclone area. Surprisingly, tracking the cyclone at isentropic surfaces (304 K) showed that identification of the cyclone with RO is superior to ECMWF (Fig. 5.24). Future studies on this topic should focus more on large slow moving cyclones or work with a higher time resolution.

It remains an open question whether Arctic amplification influences storm tracks or not. Although storm track changes in the 21st century were not investigated in this research, previous studies predict a variation in cyclone locations (Catto et al. 2011; Woollings et al. 2012; Harvey et al. 2014). There is a high propability that in a warmer climate we will see a stronger shift in storm tracks and more extreme weather events happening along its way (Ulbrich et al. 2009; Zappa et al. 2013; IPCC 2018).

# Acronyms

**FORMOSAT-3** Formosa Satellite mission-3.

**TerraSAR-X** Terra: the Earth; SAR: Synthetic Aperture Radar; X: X-band radar (wavelength).

**AMOC** Atlantic Meridional Overturning Circulation.

**AO** Arctic Oscillation.

**AR** Autoregressive process.

**AR4** Fourth Assessment Report.

**CHAMP** Challenging Mini-Satellite Payload.

**CMIP3** Coupled Model Intercomparison Project 3.

**COSMIC** Constellation Observing System for Meteorology, Ionosphere, and Climate.

**ECMWF** European Centre for Medium-Range Weather Forecasts.

**ENSO** El Niño–Southern Oscillation.

**EOF** Empirical Orthogonal Functions.

**ERAI** ERA-Interim.

**F3C** FORMOSAT-3/COSMIC.

**GLS** Generalized Least Squares.

**GLSAR** Generalized Least Squares Autoregressive process.

**GNSS** Global Navigation Satellite System.

**GPS** Global Positioning System.

**GRACE** Gravity Recovery and Climate Experiment.

**GRAS** Global Navigation Satellite Systems Receiver for Atmospheric Sounding.

**IFS** Integrated Forecasting System.

**IMILAST** Intercomparison of Mid-Latitude Storm Diagnostics.

**IPCC** Intergovernmental Panel on Climate Change.

**IR** Infrared.

**ITCZ** Inter-Tropical Convergence Zone.

**LEO** Low Earth Orbit.

**MetOp** Meteorological Operational [satellite series].

**MSL** Mean Sea Level.

**MSLP** Mean Sea Level Pressure.

**NAO** North Atlantic Oscillation.

**NASA** National Aeronautics and Space Administration.

**NOAA** National Oceanic and Atmospheric Administration.

**OLS** Ordinary Least Squares.

**OPSv5.6** Occultation Processing System version 5.6.

**PC** Principal Component.

**QBO** Quasi-Biennial Oscillation.

**RAOB** Radiosonde Observation.

**RO** Radio Occultation.

**RV** Residual Variance.

**SAC-C** Satélite de Aplicaciones Científicas/Scientific Applications Satellite C.

**SE** Sampling Error.

**SLP** Sea Level Pressure.

**SST** Sea Surface Temperature.

**SSW** Sudden Stratospheric Warming.

**TP** Tangent Point.

**UCAR** University Corporation for Atmospheric Research.

**UG** University of Graz.

**UTC** Universal Time Coordinated.

**UV** Ultraviolet.

**WEGC** Wegener Center for Climate and Global Change [University of Graz].

# List of Figures

1.1. Temperature anomaly on 27 February 2018 . . . . . . . . . . . . . . 2

2.1. Layers of Earth's Atmosphere . . . . . . . . . . . . . . . . . . . . . . . . . 7
2.2. Arctic amplification . . . . . . . . . . . . . . . . . . . . . . . . . . . . . 8
2.3. Evolution of a cyclone . . . . . . . . . . . . . . . . . . . . . . . . . . . . 10
2.4. Global drivers causing storm track change . . . . . . . . . . . . . . . . 14
2.5. QBO illustration through tropical monthly mean temperature anomalies 16
2.6. Climate pattern across the tropical Pacific illustrating ENSO events 18
2.7. Example for sudden stratospheric warming . . . . . . . . . . . . . . . 21

3.1. RO observations from different satellites . . . . . . . . . . . . . . . . 26
3.2. Schematic geometrie of RO . . . . . . . . . . . . . . . . . . . . . . . . . 27
3.3. Summary of the RO retrieval algorithm of the OPSv5.6 retrieval . . 28

5.1. Temperature anomaly gradient from 2002–2016 for the winter season 40
5.2. Temperature anomaly gradient from 2002–2016 for the summer season 41
5.3. Different latitude bands used for the differencing method . . . . . . 42
5.4. Global RO temperature difference without indices . . . . . . . . . . 43
5.5. Global RO temperature difference with tropical and Arctic indices . 44
5.6. Atlantic RO temperature difference with and without indices . . . . 45
5.7. Trend in zonal mean temperature difference between the tropics and the Arctic based on RO data, compare different index applications for RO data . . . . . . . . . . . . . . . . . . . . . . . . . . . . . . . . . . 46
5.8. Zonal Mean temperature trend for the tropical and the Arctic region 47
5.9. Trend in global temperature difference between the tropical and the Arctic region, compare RO, ERAI and ECMWF data . . . . . . . . 47
5.10. Global temperature trend for the Arctic and the tropics separately, compare RO, ERAI and ECMWF data . . . . . . . . . . . . . . . . . 48
5.11. Trend in the Atlantic temperature difference between the tropics and the Arctic region, compare different indexing applications for RO data 50
5.12. Atlantic temperature trend for the tropical and the Arctic region . . 51
5.13. Trend in Atlantic temperature difference between Arctic and tropics, compare RO, ERAI and ECMWF data . . . . . . . . . . . . . . . . . 51
5.14. Atlantic temperature trend for the tropics and the Arctic separately, compare RO, ERAI and ECMWF data as well as ocean and land data 52
5.15. Temperature trends for the northern hemisphere 2002–2017, compare indices usage . . . . . . . . . . . . . . . . . . . . . . . . . . . . . . 53

5.16. Seasonal temperature trends for the northern hemisphere , compare indices usage . . . 55
5.17. Seasonal temperature trends for the tropics and the Arctic for the winter and summer seasons . . . 56
5.18. Seasonal temperature trends for the tropics and the Arctic for the spring and autumn seasons . . . 57
5.19. Trend in geopotential height for global and Atlantic RO anomaly data 58
5.20. Trend in geopotential height for global and Atlantic Arctic and tropical RO data . . . 60
5.21. Storm Klaus geopotential height difference at 850 hPa . . . 62
5.22. Geopotential height at 293 K isentropic surface for RO and ECMWF data for Storm Klaus . . . 63
5.23. Storm Haiyan geopotential height difference at 850 hPa . . . 64
5.24. Geopotential height at 304 K isentropic surface for RO and ECMWF data for Storm Haiyan . . . 65

A.1. Global ECMWF temperature difference without indices . . . 92
A.2. Global ERAI temperature difference without indices . . . 92
A.3. Global ECMWF temperature difference with tropical and polar indices 93
A.4. Global ERAI temperature difference with tropical and polar indices 93
A.5. Atlantic ECMWF temperature difference with and without indices . 94
A.6. Atlantic ERAI temperature difference with and without indices . . . 95
A.7. Trend in geopotential height for global and Atlantic ECMWF anomaly data . . . 96
A.8. Trend in geopotential height for the zonal mean tropical and Arctic ECMWF anomaly data . . . 97

B.1. Measurement points for Arctic and tropics . . . 100
B.2. Sampling error trend for tropical and Arctic RO temperature anomaly data . . . 101
B.3. Sampling Error for different latitude bands . . . 102
B.4. Sampling Error for 2002 . . . 103
B.5. Sampling Error for 2003 . . . 104
B.6. Sampling Error for 2004 . . . 105
B.7. Sampling Error for 2005 . . . 106
B.8. Sampling Error for 2006 . . . 107
B.9. Sampling Error for 2007 . . . 108
B.10. Sampling Error for 2008 . . . 109
B.11. Sampling Error for 2009 . . . 110
B.12. Sampling Error for 2010 . . . 111
B.13. Sampling Error for 2011 . . . 112
B.14. Sampling Error for 2012 . . . 113
B.15. Sampling Error for 2013 . . . 114
B.16. Sampling Error for 2014 . . . 115

B.17. Sampling Error for 2015 . . . . . . . . . . . . . . . . . . . . . . . . . . 116
B.18. Sampling Error for 2016 . . . . . . . . . . . . . . . . . . . . . . . . . . 117

C.1. Storm Klaus geopotential height difference on six-hourly intervals for the 23 January . . . . . . . . . . . . . . . . . . . . . . . . . . . . . . . . 120
C.2. Storm Klaus geopotential height difference in six-hourly intervals for the 24 January . . . . . . . . . . . . . . . . . . . . . . . . . . . . . . . . 121
C.3. Storm Haiyan geopotential height difference in six-hourly intervals from 06 November to 07 November . . . . . . . . . . . . . . . . . . . . 122
C.4. Storm Haiyan geopotential height difference in six-hourly intervals from 07 November to 08 November . . . . . . . . . . . . . . . . . . . . 123
C.5. Geopotential height at 293 K potential temperature surface for ECMWF data for Storm Klaus in six-hourly intervals for the 23 January . . . 124
C.6. Geopotential height at 293 K potential temperature surface for ECMWF data for Storm Klaus in six-hourly intervals for the 24 January . . . 125
C.7. Geopotential height at a 304 K isentropic surface for ECMWF data for Storm Haiyan in six-hourly intervals from 06 November to 07 November 126
C.8. Geopotential height at a 304 K isentropic surface for ECMWF data for Storm Haiyan in six-hourly intervals from 07 November to 08 November 127

# Bibliography

Aguado, E. and J. E. Burt (2006). *Understanding Weather and Climate*. 4th ed. Prentice-Hall (Pearson Education). 474 pp. ISBN: 0131496964.

Ahrens, T. J., ed. (1995). *Global Earth Physics: A Handbook of Physical Constants*. American Geophysical Union. 376 pp.

Akpan, E. A. and I. U. Moffat (2018). “Modeling the Autocorrelated Errors in Time Series Regression: A Generalized Least Squares Approach”. *J. Adv. Math. Com. Sci.* 26.4, pp. 1–15. DOI: 10.9734/JAMCS/2018/39949.

Alexeev, V. A., P. L. Langen, and J. R. Bates (2005). “Polar amplification of surface warming on an aquaplanet in ‘ghost’ forcing experiments without sea ice feedbacks”. *Climate Dyn.* 24.7, pp. 655–666. ISSN: 1432-0894. DOI: 10.1007/s00382-005-0018-3.

Allen, R. J. and S. C. Sherwood (2008). “Warming maximum in the tropical upper troposphere deduced from thermal winds”. *Nature Geoscience* 1. DOI: 10.1038/ngeo208.

AMAP (2017). “Snow, Water, Ice and Permafrost. Summary for Policy-makers”. In: Oslo, Norway: Arctic Monitoring and Assessment Programme (AMAP), pp. 1–20.

Andrews, D. G. (2000). *An Introduction to Atmospheric Physics*. Cambridge University Press. 240 pp.

Andrews, D. G., J. R. Holton, and C. B. Leovy (1987). *Middle Atmosphere Dynamics*. Vol. 40. International Geophysical Series. Academic Press. 489 pp.

Angerer, B., F. Ladstädter, B. Scherllin-Pirscher, M. Schwärz, A. K. Steiner, U. Foelsche, and G. Kirchengast (2017). “Quality aspects of the WEGC multi-satellite GPS radio occultation record OPSv5.6”. *Atmos. Meas. Tech.* 10, pp. 4845–4863. DOI: 10.5194/amt-10-4845-2017.

Anthes, R. A. (2011). “Exploring Earth’s atmosphere with radio occultation: contributions to weather, climate, and space weather”. *Atmos. Meas. Tech.* 4, pp. 1077–1103. DOI: 10.5194/amt-4-1077-2011.

Anthes, R. A., P. A. Bernhardt, Y. Chen, L. Cucurull, K. F. Dymond, D. Ector, S. B. Healy, S.-P. Ho, D. C. Hunt, Y.-H. Kuo, H. Liu, K. Manning, C. McCormick, T. K. Meehan, W. J. Randel, C. Rocken, W. S. Schreiner, S. V. Sokolovskiy, S. Syndergaard, D. C. Thompson, K. E. Trenberth, T.-K. Wee, N. L. Yen, and Z. Zeng (2008). “The COSMIC/FORMOSAT-3 mission: Early results”. *Bull. Amer. Meteor. Soc.* 89.3, pp. 313–333. DOI: 10.1175/BAMS-89-3-313.

Arnone, E., E. Castelli, E. Papandrea, M. Carlotti, and B. M. Dinelli (2012). “Extreme ozone depletion in the 2010–2011 Arctic winter stratosphere as observed by MIPAS/ENVISAT using a 2-D tomographic approach”. *Atmos. Chem. Phys.* 12, pp. 9149–9165. DOI: 10.5194/acp-12-9149-2012.

Bader, J., M. D. Mesquita, K. I. Hodges, N. Keenlyside, S. Østerhus, and M. Miles (2011). “A review on Northern Hemisphere sea-ice, storminess and the North Atlantic Oscillation: Observations and projected changes”. *Atmos. Res.* 101.4, pp. 809–834. DOI: 10.1016/j.atmosres.2011.04.007.

Baldwin, M. P., L. J. Gray, T. J. Dunkerton, K. Hamilton, P. H. Haynes, W. J. Randel, J. R. Holton, M. J. Alexander, I. Hirota, T. Horinouchi, D. B. A. Jones, J. S. Kinnersley, C. Marquardt, K. Sato, and M. Takahashi (2001). “The Quasi-Biennial Oscillation”. *Rev. Geophys.* 39.2, pp. 179–229.

Barnes, E. A. and L. Polvani (2013). “Response of the Midlatitude Jets, and of Their Variability, to Increased Greenhouse Gases in the CMIP5 Models”. *J. Climate* 26.18, pp. 7117–7135. DOI: 10.1175/jcli-d-12-00536.1.

Barnes, E. A. and J. A. Screen (2015). “The impact of Arctic warming on the midlatitude jet-stream: Can it? Has it? Will it?” *WIRes. Clim. Change* 6.3, pp. 277–286. DOI: 10.1002/wcc.337.

Bates, D. R. (1959). “Some Problems concerning the Terrestrial Atmosphere above about the 100 km Level”. *P. Roy. Soc. Lond. A Mat.* 253.1275, pp. 451–462. DOI: 10.1098/rspa.1959.0207.

Bauer, S. and H. Lammer (2004). *Planetary Aeronomy*. 1st ed. Springer-Verlag Berlin Heidelberg. ISBN: 978-3-540-21472-4.

Baum, W. A. and A. D. Code (1953). “A photometric observation of the occultation of $\sigma$ ARIETIS by Jupiter”. *Astronomical Journal* 58, pp. 108–112. DOI: 10.1086/106829.

Bengtsson, L., K. I. Hodges, and N. Keenlyside (2009). “Will Extratropical Storms Intensify in a Warmer Climate?” *J. Climate* 22, pp. 2276–2301. DOI: 10.1175/2008JCLI2678.1.

Bengtsson, L., K. I. Hodges, and E. Roeckner (2005). “Storm Tracks and Climate Change”. *J. Climate* 19.15, pp. 3518–3543. DOI: 10.1175/JCLI3815.1.

Beyerle, G., T. Schmidt, G. Michalak, S. Heise, J. Wickert, and C. Reigber (2005). “GPS radio occultation with GRACE: Atmospheric profiling utilizing the zero difference technique”. *Geophys. Res. Lett.* 32, L13806. DOI: 10.1029/2005GL023109.

Borsche, M. (2008). *Global atmospheric climatologies from radio occultation data and derivation of diagnostic parameters for climate monitoring (Ph.D. Thesis)*. Austria: Wegener Center Verlag Graz.

Brasseur, G. P. and S. Solomon (2005). *Aeronomy of the Middle Atmosphere*. 3rd ed. Springer Netherlands. 646 pp. ISBN: 978-1-4020-3284-4.

Brunner, L., A. K. Steiner, B. Scherllin-Pirscher, and M. W. Jury (2016). “Exploring atmospheric blocking with GPS radio occultation observations”. *Atmos. Chem. Phys.* 16.7, pp. 4593–4604. DOI: 10.5194/acp-16-4593-2016.

Butler, A. H. and L. M. Polvani (2011). “El Niño, La Niña, and stratospheric sudden warmings: A reevaluation in light of the observational record”. *Geophys. Res. Lett.* 38, L13807. DOI: 10.1029/2011GL048084.

Butler, A. H., L. M. Polvani, and C. Deser (2014). “Separating the stratospheric and tropospheric pathways of El Niño–Southern Oscillation teleconnections”. *Environ. Res. Lett.* 9.2. DOI: 10.1088/1748-9326/9/2/024014.

Butler, A. H., J. P. Sjoberg, D. J. Seidel, and K. H. Rosenlof (2017). "A sudden stratospheric warming compendium". *Earth Sys. Sci. Data* 9.1, pp. 63–76. DOI: 10.5194/essd-9-63-2017.

Butler, A. H., D. W. J. Thompson, and R. Heikes (2010). "The steady-state atmospheric circulation response to climate change-like thermal forcings in a simple General circulation model". *J. Climate* 23, pp. 3474–3496. DOI: 10.1175/2010JCLI3228.1.

Capotondi, A. (2015). "Understanding ENSO Diversity". *Bull. Amer. Meteor. Soc.* 96, pp. 921–938. DOI: 10.1175/BAMS-D-13-00117.1.

Catto, J. L., L. C. Shaffrey, and K. I. Hodges (2011). "Northern Hemisphere Extratropical Cyclones in a Warming Climate in the HiGEM High-Resolution Climate Model". *J. Climate* 24.20, pp. 5336–5352. DOI: 10.1175/2011JCLI4181.1.

Chang, E. K. M. (2009). "Diabatic and Orographic Forcing of Northern Winter Stationary Waves and Storm Tracks". *J. Climate* 22.3, pp. 670–688. DOI: 10.1175/2008jcli2403.1.

Chang, E. K. M., S. Lee, and K. L. Swanson (2002). "Storm Track Dynamics". *J. Climate* 15.16, pp. 2163–2183. DOI: 10.1175/1520-0442(2002)015<02163:STD>2.0.CO;2.

Charlton, A. J. and L. M.Polvani (2007). "A New Look at Stratospheric Sudden Warmings. Part I: Climatology and Modeling Benchmarks". *J. Climate* 20.3, pp. 449–469. DOI: 10.1175/JCLI3996.1.

Choi, J., S.-I. An, and S.-W. Yeh (2012). "Decadal amplitude modulation of two types of ENSO and its relationship with the mean state". *Climate Dyn.* 38.11, pp. 2631–2644. DOI: 10.1007/s00382-011-1186-y.

Cohen, J. L., J. C. Furtado, M. Barlow, V. A. Alexeev, and J. E. Cherry (2012). "Asymmetric seasonal temperature trends". *Geophys. Res. Lett.* 39. DOI: 10.1029/2011gl050582.

Cohen, J., J. A. Screen, J. C. Furtado, M. Barlow, D. Whittleston, D. Coumou, J. Francis, K. Dethloff, D. Entekhabi, J. Overland, and J. Jones (2014). "Recent Arctic amplification and extreme mid-latitude weather". *Nature Geoscience* 7.9, pp. 627–637. DOI: 10.1038/ngeo2234.

Dacre, H. F., M. K. Hawcroft, M. A. Stringer, and K. I. Hodges (2012). "An Extratropical Cyclone Atlas: A Tool for Illustrating Cyclone Structure and Evolution Characteristics". *Bull. Amer. Meteor. Soc.* 93.10, pp. 1497–1502. DOI: 10.1175/BAMS-D-11-00164.1.

Dee, D. P., S. M. Uppala, A. J. Simmons, P. Berrisford, P. Poli, S. Kobayashi, U. Andrae, M. A. Balmaseda, G. Balsamo, P. Bauer, P. Bechtold, A. C. M. Beljaars, L. van de Berg, J. Bidlot, N. Bormann, C. Delsol, R. Dragani, M. Fuentes, A. J. Geer, L. Haimberger, S. B. Healy, H. Hersbach, E. V. Hólm, L. Isaksen, P. Kållberg, M. Köhler, M. Matricardi, A. P. McNally, B. M. Monge-Sanz, J.-J. Morcrette, B.-K. Park, C. Peubey, P. de Rosnay, C. Tavolato, J.-N. Thépaut, and F. Vitart (2011). "The ERA-Interim reanalysis: configuration and performance of the data assimilation system". *Quart. J. Roy. Meteor. Soc.* 137.656, pp. 553–597. DOI: 10.1002/qj.828.

Dreyer, J. L. E. (1906). *History of the planetary systems from Thales to Kepler*. Cambridge University Press. 454 pp.

Dunkerton, T. J. and D. P. Delisi (1985). “Climatology of the Equatorial Lower Stratosphere”. *J. Atmos. Sci.* 42.4, pp. 376–396. ISSN: 0022-4928, 1520-0469. DOI: 10.1175/1520-0469(1985)042<0376:COTELS>2.0.CO;2.

Eady, E. T. (1949). “Long Waves and Cyclone Waves”. *Tellus* 1.3, pp. 33–52. DOI: 10.1111/j.2153-3490.1949.tb01265.x.

Elachi, C. and J. van Zyl (2006). *Introduction to the Physics and Techniques of Remote Sensing*. 2nd ed. John Wiley & Sons, Inc. Publication. DOI: 10.1002/0471783390.

Feng, W., B. Kaifler, D. R. Marsh, J. Höffner, U.-P. Hoppe, B. P. Williams, and J. M. Plane (2017). “Impacts of a sudden stratospheric warming on the mesospheric metal layers”. *J. Atmos. Solar-Terr. Phys.* 162, pp. 162–171. DOI: 10.1016/j.jastp.2017.02.004.

Fjeldbo, G., A. J. Kliore, and V. R. Eshleman (1971). “The neutral atmosphere of Venus as studied with the Mariner V radio occultation experiments”. *The Astronomical Journal* 76.2, pp. 123–140. DOI: 10.1086/111096.

Foelsche, U., M. Borsche, A. K. Steiner, A. Gobiet, B. Pirscher, G. Kirchengast, J. Wickert, and T. Schmidt (2008). “Observing upper troposphere-lower stratosphere climate with radio occultation data from the CHAMP satellite”. *Climate Dyn.* 31, pp. 49–65. DOI: 10.1007/s00382-007-0337-7.

Foelsche, U., B. Scherllin-Pirscher, F. Ladstädter, A. K. Steiner, and G. Kirchengast (2011a). “Refractivity and temperature climate records from multiple radio occultation satellites consistent within 0.05 %”. *Atmos. Meas. Tech.* 4, pp. 2007–2018. DOI: 10.5194/amt-4-2007-2011.

Foelsche, U., S. Syndergaard, J. Fritzer, and G. Kirchengast (2011b). “Errors in GNSS radio occultation data: relevance of the measurement geometry and obliquity of profiles”. *Atmos. Meas. Tech.* 4, pp. 189–199. DOI: 10.5194/amt-4-189-2011.

Fox, J. (2002). *Time-Series Regression and Generalized Least Squares Appendix to An R and S-PLUS Companion to Applied Regression*. Sage.

Francis, J. A. and S. J. Vavrus (2015). “Evidence for a wavier jet stream in response to rapid Arctic warming”. *Environ. Res. Lett.* 10.1. DOI: 10.1088/1748-9326/10/1/014005.

Free, M. (2011). “The Seasonal Structure of Temperature Trends in the Tropical Lower Stratosphere”. *J. Climate* 24, pp. 859–866. DOI: 10.1175/2010jcli3841.1.

Genio, A. D. (2011). *Will a Warmer World Be Stormier?* URL: https://www.giss.nasa.gov/research/briefs/delgenio_07/ (visited on 10/10/2018).

Gershenfeld, N. (1999). *The Nature of Mathematical Modeling*. Cambridge University Press. 356 pp.

Gobiet, A. and G. Kirchengast (2004). “Advancements of Global Navigation Satellite System radio occultation retrieval in the upper stratosphere for optimal climate monitoring utility”. *J. Geophys. Res.* 109, D24110. DOI: 10.1029/2004JD005117.

Gorbunov, M. E. (2002). “Canonical transform method for processing radio occultation data in the lower troposphere”. *Radio Sci.* 37.5. DOI: 10.1029/2000RS002592.

Gray, W. M. (1968). “Global view of the origin of tropical disturbances and storms”. *Mon. Wea. Rev.* 96.10, pp. 669–700. DOI: 10.1175/1520-0493(1968)096<0669:GVOTOO>2.0.CO;2.

Grotjahn, R. (2014). “Dynamical Meteorology: Baroclinic Instability”. In: *Encyclopedia of Atmospheric Sciences: Second Edition.* Elsevier Inc., pp. 304–312. ISBN: 9780123822253. DOI: 10.1016/B978-0-12-382225-3.00076-1.

Hajj, G. A., C. O. Ao, B. A. Iijima, D. Kuang, E. R. Kursinski, A. J. Mannucci, T. K. Meehan, L. J. Romans, M. de la Torre Juarez, and T. P. Yunck (2004). “CHAMP and SAC-C atmospheric occultation results and intercomparisons”. *J. Geophys. Res.* 109, D06109. DOI: 10.1029/2003JD003909.

Hansen, J., R. Ruedy, M. Sato, and K. Lo (2010). “Global surface temperature change”. *Rev. Geophys.* 48, RG4004. DOI: 10.1029/2010RG000345.

Hart, R. E. and J. L. Evans (2001). “A Climatology of the Extratropical Transition of Atlantic Tropical Cyclones”. *J. Climate* 14.4, pp. 546–564. DOI: 10.1175/1520-0442(2001)014<0546:ACOTET>2.0.CO;2.

Harvey, B. J., L. C. Shaffrey, and T. J. Woollings (2014). “Equator-to-pole temperature differences and the extra-tropical storm track responses of the CMIP5 climate models”. *Climate Dyn.* 43.5, pp. 1171–1182. DOI: 10.1007/s00382-013-1883-9.

Healy, S. (2007). “Operational assimilation of GPS radio occultation measurements at ECMWF”. *ECMWF Newsletter* 111, pp. 6–11.

Held, I. M., M. Ting, and H. Wang (2002). “Northern Winter Stationary Waves: Theory and Modeling”. *J. Climate* 15.16, pp. 2125–2144. DOI: 10.1175/1520-0442(2002)015<2125:nwswta>2.0.co;2.

Highwood, E. J. and B. J. Hoskins (1998). “The tropical tropopause”. *Quart. J. Roy. Meteor. Soc.* 124.549, pp. 1579–1604. DOI: 10.1002/qj.49712454911.

Hobe, M. von, A. Ulanovsky, C. M. Volk, J. .-.-U. Grooß, S. Tilmes, P. Konopka, G. Günther, A. Werner, N. Spelten, and G. Shur (2006). “Severe ozone depletion in the cold Arctic winter 2004–05”. *Geophys. Res. Lett.* 33. DOI: 10.1029/2006gl026945.

Holton, J. R. and J. Austin (1991). “The Influence of the Equatorial QBO on Sudden Stratospheric Warmings”. *J. Atmos. Sci.* 48, pp. 607–618.

Holton, J. and G. J. Hakim (2013). *An Introduction to Dynamic Meteorology.* 5th ed. Academic Press. ISBN: 978-0-12-384866-6.

Hoskins, B. J. and K. I. Hodges (2002). “New Perspectives on the Northern Hemisphere Winter Storm Tracks”. *J. Atmos. Sci.* 59.6, pp. 1041–1061. DOI: 10.1175/1520-0469(2002)059<1041:NPOTNH>2.0.CO;2.

Hoskins, B. J. and P. J. Valdes (1990). “On the Existence of Storm-Tracks”. *J. Atmos. Sci.* 47.15, pp. 1854–1864. DOI: 10.1175/1520-0469(1990)047<1854:oteost>2.0.co;2.

IPCC (2007). *Climate Change 2007: The Physical Science Basis. Contribution of Working Group I to the Fourth Assessment Report of the Intergovernmental Panel on Climate Change.* Ed. by S. Solomon, D. Qin, M. Manning, Z. Chen, M. Marquis, K. B. Averyt, M. Tignor, and H. L. Miller. Cambridge, United Kingdom and New York, NY, USA: Cambridge University Press.

– (2013). *Climate Change 2013: The Physical Science Basis. Contribution of Working Group I to the Fifth Assessment Report of the Intergovernmental Panel on Climate*

*Change*. Ed. by T. F. Stocker, D. Qin, G.-K. Plattner, M. Tignor, S. K. Allen, J. Boschung, A. Nauels, Y. Xia, V. Bex, and P. M. Midgley. Cambridge, United Kingdom and New York, NY, USA: Cambridge University Press. 1535 pp.

IPCC (2014). *Climate Change 2014: Impacts, Adaptation, and Vulnerability. Part A: Global and Sectoral Aspects. Contribution of Working Group II to the Fifth Assessment Report of the Intergovernmental Panel on Climate Change*. Ed. by C. B. Field, V. R. Barros, D. J. Dokken, K. J. Mach, M. D. Mastrandrea, T. E. Bilir, M. Chatterjee, K. L. Ebi, Y. O. Estrada, R. C. Genova, B. Girma, E. S. Kissel, A. N. Levy, S. MacCracken, P. R. Mastrandrea, and L. L. White. Cambridge, United Kingdom and New York, NY, USA: Cambridge University Press. 1132 pp.

– (2018). “Summary for Policymakers”. In: *Global warming of 1.5 °C – An IPCC special report on the impacts of global warming of 1.5 °C above pre - industrial levels and related global greenhouse gas emission pathways, in the context of strengthening the global response to the threat of climate change, sustainable development, and efforts to eradicate poverty*. Ed. by N. Ellis, T. Guillen, D. Huppmann, K. de Kleijne, R. Millar, and C. Singh. Cambridge, UK, and New York, NY, USA: Cambridge University Press, pp. 1–33.

Jakowski, N., S. Heise, A. Wehrenpfennig, S. Schlüter, and R. Reimer (2002). “GPS/GLONASS-based TEC measurements as a contributor for space weather forecast”. *J. Atmos. Solar-Terr. Phys.* 64, pp. 729–735.

Jin, F.-F., S. T. Kim, and L. Bejarano (2006). “A coupled-stability index for ENSO”. *Geophys. Res. Lett.* 33. DOI: 10.1029/2006GL027221.

Kidston, J., A. A. Scaife, S. C. Hardiman, D. M. Mitchell, N. Butchart, M. P. Baldwin, and L. J. Gray (2015). “Stratospheric influence on tropospheric jet streams, storm tracks and surface weather”. *Nature Geoscience* 8, pp. 433–440. DOI: 10.1038/ngeo2424.

Kishore, P., I. Velicogna, M. V. Ratnam, J. Jiang, and G. N. Madhavi (2012). “Planetary waves in the upper stratosphere and lower mesosphere during 2009 Arctic major stratospheric warming”. *Ann. Geophys.* 30, pp. 1529–1538. DOI: 10.5194/angeo-30-1529-2012.

Kretschmer, M., D. Coumou, J. F. Donges, and J. Runge (2016). “Using Causal Effect Networks to Analyze Different Arctic Drivers of Midlatitude Winter Circulation”. *J. Climate* 29.11, pp. 4069–4081. DOI: 10.1175/jcli-d-15-0654.1.

Kuo, Y.-H., S. Sokolovskiy, R. A. Anthes, and F. Vandenberghe (2000). “Assimilation of GPS radio occultation data for numerical weather prediction”. *Terr. Atmos. Ocean. Sci.* 11.1, pp. 157–186.

Kursinski, E. R., G. A. Hajj, J. T. Schofield, R. P. Linfield, and K. R. Hardy (1997). “Observing Earth’s atmosphere with radio occultation measurements using the Global Positioning System”. *J. Geophys. Res.* 102.D19, pp. 23429–23465. DOI: 10.1029/97JD01569.

Labitzke, K., M. Kunze, and S. Brönnimann (2006). “Sunspots, the QBO, and the Stratosphere in the North Polar Region – 20 Years later”. *Met. Z.* 15, pp. 355–363. DOI: 10.1127/0941-2948/2006/0136.

Ladstädter, F., A. K. Steiner, U. Foelsche, L. Haimberger, C. Tavolato, and G. Kirchengast (2011). "An assessment of differences in lower stratospheric temperature records from (A)MSU, radiosondes, and GPS radio occultation". *Atmos. Meas. Tech.* 4, pp. 1965–1977. DOI: 10.5194/amt-4-1965-2011.

Ladstädter, F., A. K. Steiner, M. Schwärz, and G. Kirchengast (2015). "Climate intercomparison of GPS radio occultation, RS90/92 radiosondes and GRUAN from 2002 to 2013". *Atmos. Meas. Tech.* 8, pp. 1819–1834. DOI: 10.5194/amt-8-1819-2015.

Lambert, S. J. and J. C. Fyfe (2006). "Changes in winter cyclone frequencies and strengths simulated in enhanced greenhouse warming experiments: results from the models participating in the IPCC diagnostic exercise". *Climate Dyn.* 26.7, pp. 713–728. DOI: 10.1007/s00382-006-0110-3.

Lehmann, J., D. Coumou, K. Frieler, A. V. Eliseev, and A. Levermann (2014). "Future changes in extratropical storm tracks and baroclinicity under climate change". *Environ. Res. Lett.* 9.8, p. 84002. DOI: 10.1088/1748-9326/9/8/084002.

Liberato, M. L. R., J. G. Pinto, I. F. Trigo, and R. M. Trigo (2011). "Klaus – an exceptional winter storm over northern Iberia and southern France". *Weather* 66.12, pp. 330–334. DOI: 10.1002/wea.755.

Lin, P., D. Paynter, Y. Ming, and V. Ramaswamy (2017). "Changes of the Tropical Tropopause Layer under Global Warming". *J. Climate* 30.4, pp. 1245–1258. DOI: 10.1175/JCLI-D-16-0457.1.

Liu, C.-L., G. Kirchengast, K. Zhang, R. Norman, Y. Li, S. C. Zhang, B. Carter, J. Fritzer, M. Schwaerz, S. L. Choy, S. Q. Wu, and Z. X. Tan (2013). "Characterisation of residual ionospheric errors in bending angles using GNSS RO end-to-end simulations". *Adv. Space Res.* 52.5, pp. 821–836. DOI: 10.1016/j.asr.2013.05.021.

Loiselet, M., N. Stricker, Y. Menard, and J.-P. Luntama (2000). "GRAS—MetOp's GPS-based atmospheric sounder". *ESA Bulletin* 102, pp. 38–44.

Ludwig, P., J. G. Pinto, M. Reyers, and S. L. Gray (2014). "The role of anomalous SST and surface fluxes over the southeastern North Atlantic in the explosive development of windstorm Xynthia". *Quart. J. Roy. Meteor. Soc.* 140.682, pp. 1729–1741. DOI: 10.1002/qj.2253.

Luntama, J.-P., G. Kirchengast, M. Borsche, U. Foelsche, A. Steiner, S. B. Healy, A. von Engeln, E. O'Clerigh, and C. Marquardt (2008). "Prospects of the EPS GRAS mission for operational atmospheric applications". *Bull. Amer. Meteor. Soc.* 89, pp. 1863–1875. DOI: 10.1175/2008BAMS2399.1.

Lynch, A. H. and J. J. Cassano (2006). *Atmospheric Dynamics.* John Wiley & Sons Ltd. ISBN: 978-0470861738.

Marshall, A. G. and A. A. Scaife (2009). "Impact of the QBO on surface winter climate". *J. Geophys. Res.* 114. DOI: 10.1029/2009JD011737.

Marshall, J. and R. A. Plumb (2008). *Atmosphere, Ocean, and Climate Dynamics: An Introductory Text.* Elsevier Academic Press.

Matsuno, T. (1971). "A Dynamical Model of the Stratospheric Sudden Warming". *J. Atmos. Sci.* 28.8, pp. 1479–1494. DOI: 10.1175/1520âĂŘ0469(1971)028<1479:ADMOTS>2.0.CO;2.

Mbengue, C. and T. Schneider (2017). “Storm-Track Shifts under Climate Change: Toward a Mechanistic Understanding Using Baroclinic Mean Available Potential Energy”. *J. Atmos. Sci.* 74.1, pp. 93–110. DOI: 10.1175/jas-d-15-0267.1.

McInturff, R. M. (1978). *Stratospheric warmings: synoptic, dynamic and general-circulation aspects.* 1st ed. National Aeronautics, Space Administration, Scientific, and Technical Information Office. ISBN: 0815622821.

Merrill, R. T. (1984). “A Comparison of Large and Small Tropical Cyclones”. *Mon. Wea. Rev.* 112.7, pp. 1408–1418. DOI: 10.1175/1520-0493(1984)112<1408:ACOLAS>2.0.CO;2.

Mohanakumar, K. (2008). *Stratosphere Troposphere Interactions.* India: Springer.

Naujokat, B. (1986). “An Update of the Observed Quasi-Biennial Oscillation of the Stratospheric Winds over the Tropics”. *J. Atmos. Sci.* 43.17, pp. 1873–1877. DOI: 10.1175/1520-0469(1986)043<1873:AUOTOQ>2.0.CO;2.

Newman, P. A., L. Coy, S. Pawson, and L. R. Lait (2016). “The anomalous change in the QBO in 2015–2016”. *Geophys. Res. Lett.* 43.16, 2016GL070373. ISSN: 1944-8007. DOI: 10.1002/2016GL070373.

O’Gorman, P. A. (2010). “Understanding the varied response of the extratropical storm tracks to climate change”. *PNAS* 107.45, pp. 19176–19180. DOI: 10.1073/pnas.1011547107.

Orsolini, Y. J., J. Urban, D. P. Murtagh, S. Lossow, and V. Limpasuvan (2010). “Descent from the polar mesosphere and anomalously high stratopause observed in 8 years of water vapor and temperature satellite observations by the Odin Sub-Millimeter Radiometer”. *J. Geophys. Res.* 115. DOI: 10.1029/2009jd013501.

Palmeiro, F. M., D. Barriopedro, R. García-Herrera, and N. Calvo (2015). “Comparing Sudden Stratospheric Warming Definitions in Reanalysis Data”. *J. Climate* 28, pp. 6823–6840. DOI: 10.1175/JCLI-D-15-0004.1.

Papritz, L. and T. Spengler (2015). “Analysis of the slope of isentropic surfaces and its tendencies over the North Atlantic”. *QJRMS* 141, pp. 3226–3238. DOI: 10.1002/qj.2605.

Perlwitz, J., M. Hoerling, and R. Dole (2015). “Arctic Tropospheric Warming: Causes and Linkages to Lower Latitudes”. *J. Climate* 28.6, pp. 2154–2167. DOI: 10.1175/JCLI-D-14-00095.1.

Pinto, J. G., U. Ulbrich, G. Leckebusch, T. Spangehl, M. Reyers, and S. Zacharias (2007). “Changes in storm track and cyclone activity in three SRES ensemble experiments with the ECHAM5/MPI-OM1 GCM”. *Climate Dyn.* 29, pp. 195–210. DOI: 10.1007/s00382-007-0230-4.

Pirscher, B. (2010). *Multi-satellite climatologies of fundamental atmospheric variables from radio occultation and their validation (Ph.D. thesis).* Sci. Rep. 33-2010. Austria: Wegener Center Verlag Graz. ISBN: 978-3-9502940-3-3.

Pirscher, B., U. Foelsche, B. C. Lackner, and G. Kirchengast (2007). “Local time influence in single-satellite radio occultation climatologies from Sun-synchronous and non-Sun-synchronous satellites”. *J. Geophys. Res.* 112, D11119. DOI: 10.1029/2006JD007934.

Plane, J. M. C. (2003). “Atmospheric Chemistry of Meteoric Metals”. *Chem Rev* 103.12, pp. 4963–4984. DOI: 10.1021/cr0205309.

Poli, P., S. B. Healy, and D. P. Dee (2010). “Assimilation of Global Positioning System radio occultation data in the ECMWF ERA-Interim reanalysis”. *Quart. J. Roy. Meteor. Soc.* 136.653, pp. 1972–1990. DOI: 10.1002/qj.722.

Rahmstorf, S., J. E. Box, G. Feulner, M. E. Mann, A. Robinson, S. Rutherford, and E. J. Schaffernicht (2015). “Exceptional twentieth-century slowdown in Atlantic Ocean overturning circulation”. *Nature Climate Change* 5.5, pp. 475–480. DOI: 10.1038/nclimate2554.

Randel, W. J., R. R. Garcia, N. Calvo, and D. Marsh (2009). “ENSO influence on zonal mean temperature and ozone in the tropical lower stratosphere”. *J. Geophys. Res.* 36, L15822. DOI: 10.1029/2009GL039343.

Randel, W. J. and F. Wu (2005). “Kelvin wave variability near the equatorial tropopause observed in GPS radio occultation measurements”. *J. Geophys. Res.* 110, D03102. DOI: 10.1029/2004JD005006.

Randel, W. J., F. Wu, R. Swinbank, J. Nash, and A. O’Neill (1999). “Global QBO circulation derived from UKMO stratospheric analyses”. *J. Atmos. Sci.* 56.4, pp. 457–474.

Rawlings, J. O., S. G. Pantula, and D. A. Dickey (1998). *Applied Regression Analysis: A Research Tool.* 2nd ed. Springer. 660 pp.

Richardson, D. (2005). “Changes to the operational forecasting system”. *ECMWF Newsletter* 106, pp. 1–2.

Rind, D. (2008). “The Consequences of Not Knowing Low- and High-Latitude Climate Sensitivity”. *Bull. Amer. Meteor. Soc.* 89, pp. 855–864. DOI: 10.1175/2007BAMS2520.1.

Scaife, A. A., N. Butchart, C. D. Warner, D. Stainforth, W. Norton, and J. Austin (2000). “Realistic quasi-biennial oscillations in a simulation of the global climate”. *Geophys. Res. Lett.* 27.21, pp. 3481–3484. DOI: 10.1029/2000GL011625.

Schemm, S. and M. Sprenger (2015). “Frontal-wave cyclogenesis in the North Atlantic –a climatological characterisation”. *Quart. J. Roy. Meteor. Soc.* 141.693, pp. 2989–3005. DOI: 10.1002/qj.2584.

Scherllin-Pirscher, B., G. Kirchengast, A. K. Steiner, Y.-H. Kuo, and U. Foelsche (2011a). “Quantifying uncertainty in climatological fields from GPS radio occultation: an empirical-analytical error model”. *Atmos. Meas. Tech.* 4, pp. 2019–2034. DOI: 10.5194/amt-4-2019-2011.

Scherllin-Pirscher, B., A. K. Steiner, G. Kirchengast, Y.-H. Kuo, and U. Foelsche (2011b). “Empirical analysis and modeling of errors of atmospheric profiles from GPS radio occultation”. *Atmos. Meas. Tech.* 4, pp. 1875–1890. DOI: 10.5194/amt-4-1875-2011.

Scherllin-Pirscher, B., A. K. Steiner, G. Kirchengast, M. Schwaerz, and S. S. Leroy (2017). “The power of vertical geolocation of atmospheric profiles from GNSS radio occultation”. *J. Geophys. Res.: Atmos* 122, pp. 1595–1616. DOI: 10.1002/2016JD025902.

Schimanke, S., J. Körper, T. Spangehl, and U. Cubasch (2011). “Multi-decadal variability of sudden stratospheric warmings in an AOGCM”. *Geophys. Res. Lett.* 38. DOI: 10.1029/2010GL045756.

Schneider, T., P. A. O’Gorman, and X. J. Levine (2010). “Water vapor and the dynamics of climate changes”. *Rev. Geophys.* 48. DOI: 10.1029/2009RG000302.

Schoeberl, M. and P. Newman (2014). “Middle Atmosphere: Polar Vortex”. In: *Encyclopedia of Atmospheric Sciences: Second Edition*, pp. 12–17. DOI: 10.1016/B978-0-12-382225-3.00228-0.

Schreiner, W. S., S. V. Sokolovskiy, C. Rocken, and D. C. Hunt (1999). “Analysis and validation of GPS/MET radio occultation data in the ionosphere”. *Radio Sci.* 34.4, pp. 949–966.

Schreiner, W., C. Rocken, S. Sokolovskiy, S. Syndergaard, and D. Hunt (2007). “Estimates of the precision of GPS radio occultations from the COSMIC/FORMOSAT-3 mission”. *Geophys. Res. Lett.* 34, L04808. DOI: 10.1029/2006GL027557.

Schwärz, M., B. Scherllin-Pirscher, G. Kirchengast, J. Schwarz, F. Ladstädter, J. Fritzer, and J. Ramsauer (2013). *Multi-Mission Validation by Satellite Radio Occultation.* Final report for ESA/ESRIN No. 01/2013. University of Graz, Austria: WEGC. 187 pp.

Screen, J. A. and I. Simmonds (2010). “The central role of diminishing sea ice in recent Arctic temperature amplification”. *Nature* 464, pp. 1334–1337. DOI: 10.1038/nature09051.

Seierstad, I. A. and J. Bader (2008). “Impact of a projected future Arctic Sea Ice reduction on extratropical storminess and the NAO”. *Climate Dyn.* 33, pp. 937–943. DOI: 10.1007/s00382-008-0463-x.

Serreze, M. C. and R. G. Barry (2011). “Processes and impacts of Arctic amplification: A research synthesis”. *Global Planet Change* 77, pp. 85–96. DOI: 10.1016/j.gloplacha.2011.03.004.

Sévellec, F., A. V. Fedorov, and W. Liu (2017). “Arctic sea-ice decline weakens the Atlantic Meridional Overturning Circulation”. *Nature Climate Change* 7.8, pp. 604–610. DOI: 10.1038/nclimate3353.

Shaw, T. A., M. Baldwin, E. Barnes, R. Caballero, C. I. Garfinkel, Y.-T. Hwang, C. Li, P. A. O’Gorman, G. Riviére, I. Simpson, and A. Voigt (2016). “Storm track processes and the opposing influences of climate change”. *Nature Geoscience* 9, pp. 656–664. DOI: 10.1038/NGEO2783.

Shepherd, T. G. (2014). “Atmospheric circulation as a source of uncertaintyin climate change projections”. *Nature Geoscience* 7.10, pp. 703–708. DOI: 10.1038/ngeo2253.

Simmons, A. J., P. Poli, D. P. Dee, P. Berrisford, H. Hersbach, S. Kobayashi, and C. Peubey (2014). “Estimating low-frequency variability and trends in atmospheric temperature using ERA-Interim”. *Quart. J. Roy. Meteor. Soc.* 140.679, pp. 329–353. DOI: 10.1002/qj.2317.

Simmons, A., S. Uppala, D. Dee, and S. Kobayashi (2007). “ERA-Interim: New ECMWF reanalysis products from 1989 onwards”. *ECMWF Newsletter* 110, pp. 25–35. DOI: 10.21957/pocnex23c6.

Smith, E. and S. Weintraub (1953). “The constants in the equation for atmospheric refractive index at radio frequencies”. *Proc. IRE* 41, pp. 1035–1037.

Steiner, A. K. (1998). “High resolution sounding of key climate variables using the radio occultation technique”. PhD thesis. University of Graz, Austria: IGAM.

Steiner, A. K., D. Hunt, S.-P. Ho, G. Kirchengast, A. J. Mannucci, B. Scherllin-Pirscher, H. Gleisner, A. von Engeln, T. Schmidt, C. Ao, S. S. Leroy, E. R. Kursinski, U. Foelsche, M. Gorbunov, S. Heise, Y.-H. Kuo, K. B. Lauritsen, C. Marquardt, C. Rocken, W. Schreiner, S. Sokolovskiy, S. Syndergaard, and J. Wickert (2013). “Quantification of structural uncertainty in climate data records from GPS radio occultation”. *Atmos. Chem. Phys.* 13, pp. 1469–1484. DOI: 10.5194/acp-13-1469-2013.

Steiner, A. K., G. Kirchengast, U. Foelsche, L. Kornblueh, E. Manzini, and L. Bengtsson (2001). “GNSS occultation sounding for climate monitoring”. *Phys. Chem. Earth A* 26.3, D09102, pp. 113–124. DOI: 10.1016/S1464-1895(01)00034-5.

Stewart, R. W. (1968). “Radiative terms in the thermal conduction equation for planetary atmospheres”. *J. Atmos. Sci.* 25, pp. 744–749. DOI: 10.1175/1520-0469(1968)025<0744:RTITTC>2.0.CO;2.

Stroeve, J. C., T. Markus, L. Boisvert, J. Miller, and A. Barrett (2014). “Changes in Arctic melt season and implications for sea ice loss”. *Geophys. Res. Lett.* 41.4, pp. 1216–1225. DOI: 10.1002/2013GL058951.

Timmermann, A. et al. (2018). “El Niño–Southern Oscillation complexity”. *Nature* 559, pp. 535–545. DOI: 10.1038/s41586-018-0252-6.

Trenberth, K. E., J. M. Caron, D. P. Stepaniak, and S. Worley (2002). “Evolution of El Niño–Southern Oscillation and global atmospheric surface temperatures”. *J. Geophys. Res.* 107.D8. DOI: 10.1029/2000JD000298.

Trenberth, K. E. and D. P. Stepaniak (2003). “Seamless Poleward Atmospheric Energy Transports and Implications for the Hadley Circulation”. *J. Climate Appl. Meteor.* 16.22, pp. 3706–3722. DOI: 10.1175/1520-0442(2003)016<3706:SPAETA>2.0.CO;2.

Tziperman, E. and L. Yu (2007). “Quantifying the Dependence of Westerly Wind Bursts on the Large-Scale Tropical Pacific SST”. *J. Climate* 20, pp. 2760–2768. DOI: 10.1175/JCLI4138a.1.

Ulbrich, U., G. C. Leckebusch, and J. G. Pinto (2009). “Extra-tropical cyclones in the present and future climate: a review”. *Theor. Appl. Climatol.* 96.1, pp. 117–131. DOI: 10.1007/s00704-008-0083-8.

Ulbrich, U., G. C. Leckebusch, J. Grieger, M. Schuster, M. Akperov, M. Y. Bardin, Y. Feng, S. Gulev, M. Inatsu, K. Keay, S. F. Kew, M. L. Liberato, P. Lionello, I. I. Mokhov, U. Neu, J. G. Pinto, C. C. Raible, M. Reale, I. Rudeva, I. Simmonds, N. D. Tilinina, I. F. Trigo, S. Ulbrich, and Wang (2013). “Are Greenhouse Gas Signals of Northern Hemisphere winter extra-tropical cyclone activity dependent on the identification and tracking algorithm?” *Met. Z* 22.1, pp. 61–68. DOI: 10.1127/0941-2948/2013/0420.

Vallis, G. K. and E. P. Gerber (2008). “Local and hemispheric dynamics of the North Atlantic Oscillation, annular patterns and the zonal index”. *Dynam atmos oceans* 44, pp. 184–212. DOI: 10.1016/j.dynatmoce.2007.04.003.

Voigt, C., A. Dörnbrack, M. Wirth, S. M. Groß, M. C. Pitts, L. R. Poole, R. Baumann, B. Ehard, B.-M. Sinnhuber, and W. Woiwode (2018). "Widespread polar stratospheric ice clouds in the 2015–2016 Arctic winter – implications for ice nucleation". *Atmos. Chem. Phys.* 18, pp. 15623–15641. DOI: 10.5194/acp-18-15623-2018.

Wernli, H. and C. Schwierz (2006). "Surface Cyclones in the ERA-40 Dataset (1958–2001). Part I: Novel Identification Method and Global Climatology". *J. Atmos. Sci.* 63.10, pp. 2486–2507. DOI: 10.1175/JAS3766.1.

Wickert, J., G. Beyerle, R. König, S. Heise, L. Grunwaldt, G. Michalak, C. Reigber, and T. Schmidt (2005). "GPS radio occultation with CHAMP and GRACE: A first look at a new and promising satellite configuration for global atmospheric sounding". *Ann. Geophys.* 23, pp. 653–658.

Wickert, J., T. Schmidt, G. Beyerle, R. König, C. Reigber, and N. Jakowski (2004). "The radio occultation experiment aboard CHAMP: Operational data analysis and validation of vertical atmospheric profiles". *J. Meteor. Soc. Japan* 82, pp. 381–395.

Wickert, J., T. Schmidt, G. Michalak, S. Heise, C. Arras, G. Beyerle, C. Falck, R. König, D. Pingel, and M. Rothacher (2009). "GPS radio occultation with CHAMP, GRACE-A, SAC-C, TerraSAR-X, and FORMOSAT-3/COSMIC: Brief review of results from GFZ". In: *New Horizons in Occultation Research: Studies in Atmosphere and Climate.* Ed. by A. K. Steiner, B. Pirscher, U. Foelsche, and G. Kirchengast. Berlin, Heidelberg: Springer-Verlag, pp. 3–16.

Wilhelmsen, H., F. Ladstädter, B. Scherllin-Pirscher, and A. K. Steiner (2018). "Atmospheric QBO and ENSO indices with high vertical resolution from GNSS radio occultation temperature measurements". *Atmos. Meas. Tech.* 11.3, pp. 1333–1346. DOI: 10.5194/amt-11-1333-2018.

Woollings, T., B. Harvey, and G. Masato (2014). "Arctic warming, atmospheric blocking and cold European winters in CMIP5 models". *Environ. Res. Lett.* 9.1, p. 014002. DOI: 10.1088/1748-9326/9/1/014002.

Woollings, T. (2010). "Dynamical influences on European climate: an uncertain future". *Phil. Trans. R. Soc. A* 368.1924, pp. 3733–3756. DOI: 10.1098/rsta.2010.0040.

– (2016). "Storm tracks, blocking, and climate change: a review". In: *Dynamics and Predictability of Large-Scale, High-Impact Weather and Climate Events.* Ed. by J. Li, R. Swinbank, R. Grotjahn, and H. Volkert. Special Publications of the International Union of Geodesy and Geophysics. Cambridge University Press, pp. 113–121. DOI: 10.1017/CBO9781107775541.009.

Woollings, T., J. M. Gregory, J. G. Pinto, M. Reyers, and D. J. Brayshaw (2012). "Response of the North Atlantic storm track to climate change shaped by ocean-atmosphere coupling". *Nature Geoscience* 5.5, pp. 313–317. DOI: 10.1038/ngeo1438.

Woollings, T., L. Papritz, C. Mbengue, and T. Spengler (2016). "Diabatic heating and jet stream shifts: A case study of the 2010 negative North Atlantic Oscillation winter". *Geophys. Res. Lett.* 43, pp. 9994–10002. DOI: 10.1002/2016GL070146.

Yeh, S.-W. and B. P. Kirtman (2009). "Internal Atmospheric Variability and Interannual–to– Decadal ENSO Variability in a CGCM". *J. Climate* 22.9, pp. 2335–2355. DOI: 10.1175/2008JCLI2240.1.

Yin, J. H. (2005). "A consistent poleward shift of the storm tracks in simulations of 21st century climate". *Geophys. Res. Lett.* 32.18. DOI: 10.1029/2005GL023684.

Zappa, G., L. Shaffrey, K. Hodges, P. G. Sansom, and D. B. Stephenson (2013). "A Multimodel Assessment of Future Projections of North Atlantic and European Extratropical Cyclones in the CMIP5 Climate Models". *J. Climate* 26, pp. 5846–5862. DOI: 10.1175/JCLI-D-12-00573.1.

# A. Temperature anomaly differences for ECMWF and ERAI

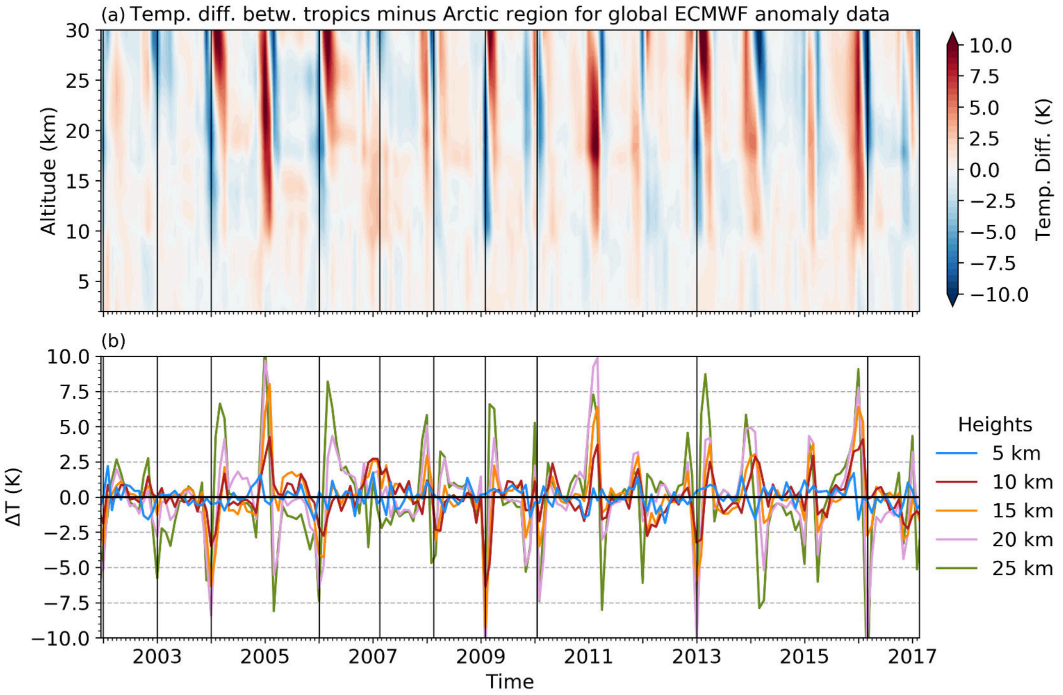

**Figure A.1.:** (a) Temperature difference between the tropics (30° S to 30° N) minus the Arctic (60° N to 85° N) based on ECMWF temperature anomaly fields. (b) Same data used as in (a), trend plotted for specific heights. The black lines indicate SSW events.

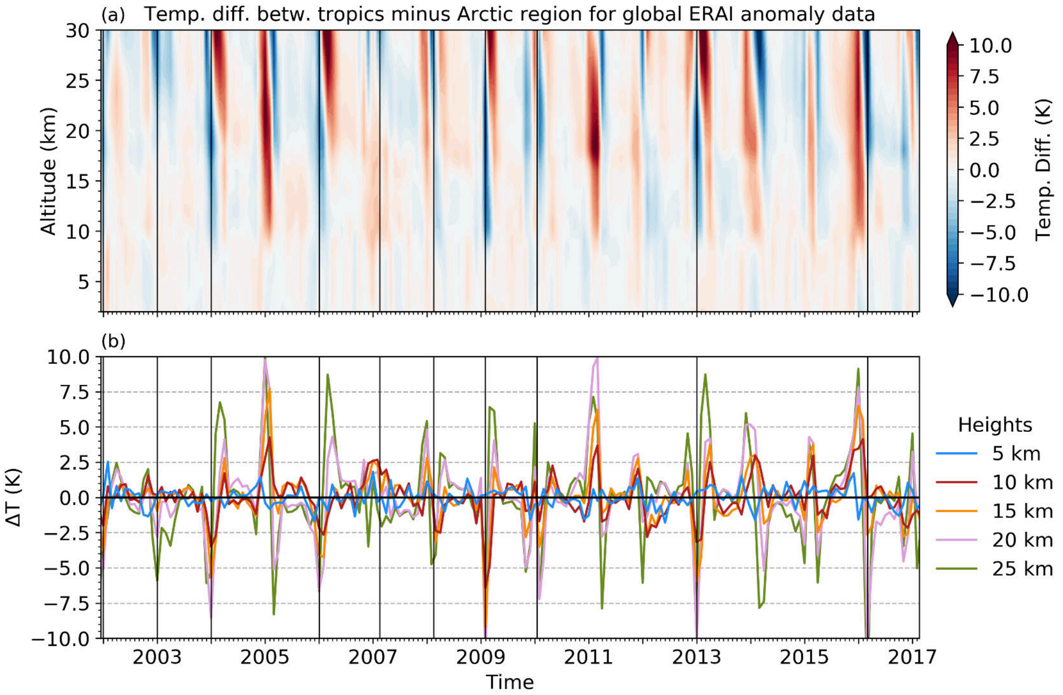

**Figure A.2.:** Same as Fig.A.1, but for the ERAI data set

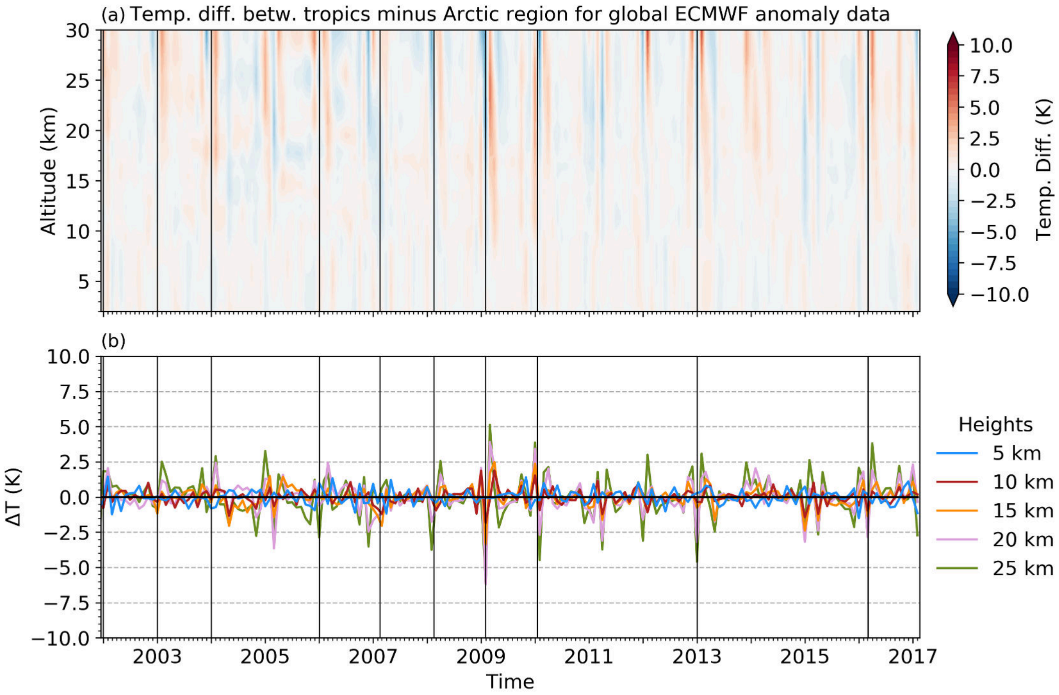

**Figure A.3.:** Same as Fig. A.1, but regressed onto a vertically resolved atmospheric variability index after Wilhelmsen et al. (2018) accounting for tropical QBO/ENSO and polar SSW events.

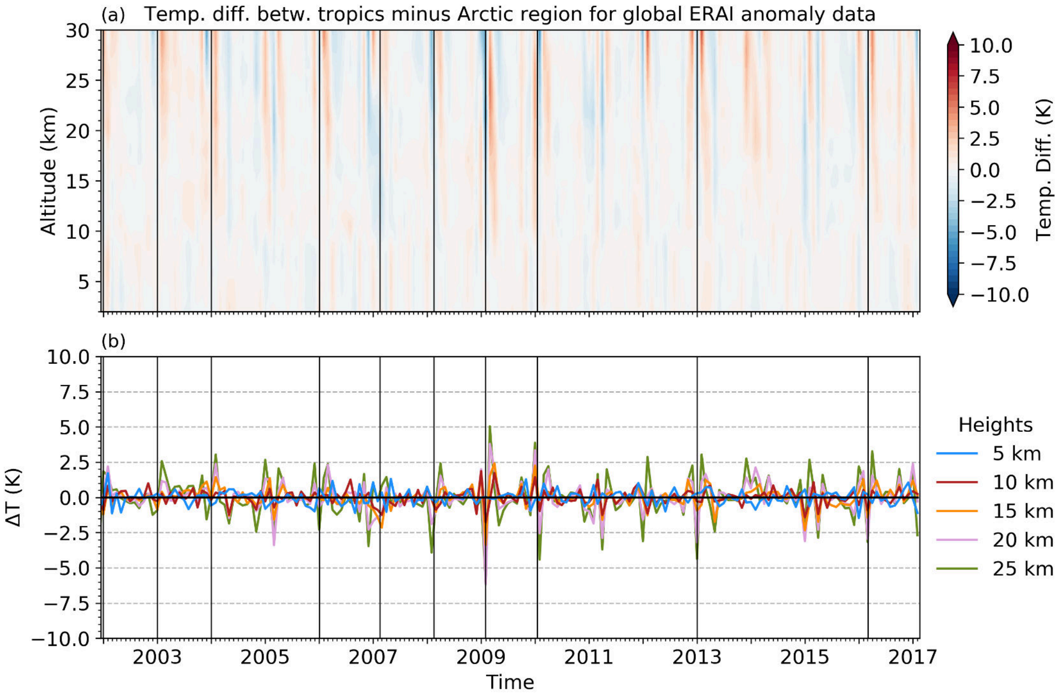

**Figure A.4.:** Same as Fig.A.3, but for the ERAI data set.

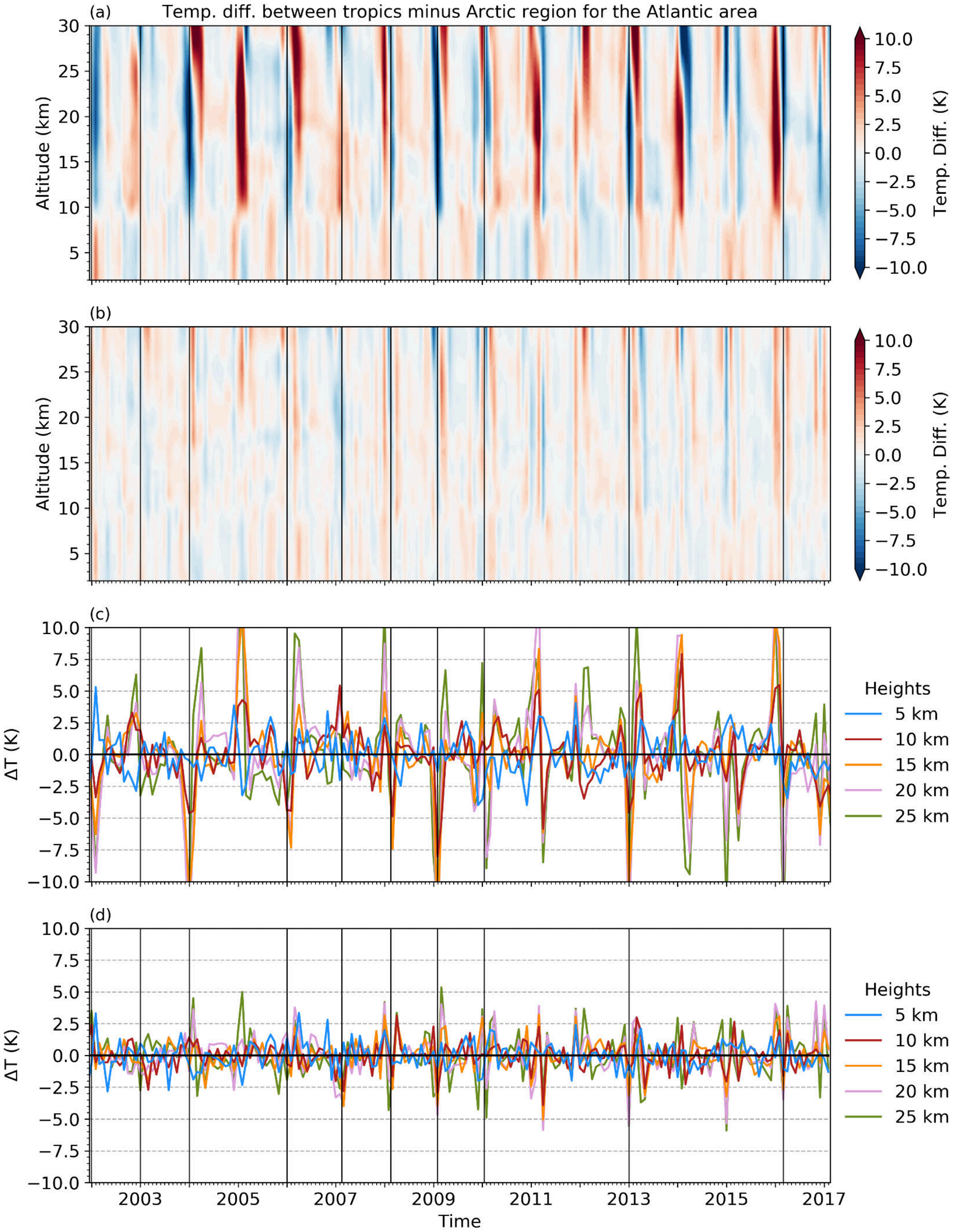

**Figure A.5.:** (a) Temperature difference between the tropics (30° S to 30° N) and the Arctic (60° N to 85° N) for the Atlantic region based on ECMWF temperature anomaly fields. The anomalies are relative to the time period between December 2001 to February 2017. (b) The data is regressed onto a vertically resolved atmospheric variability index accounting for tropical QBO/ENSO and polar SSW events. For (c) and (d) the same data as in (a) and (b) are used and the temporal evolution was plotted for specific heights only. The black lines represent Sudden Stratospheric Warming events for the same time period.

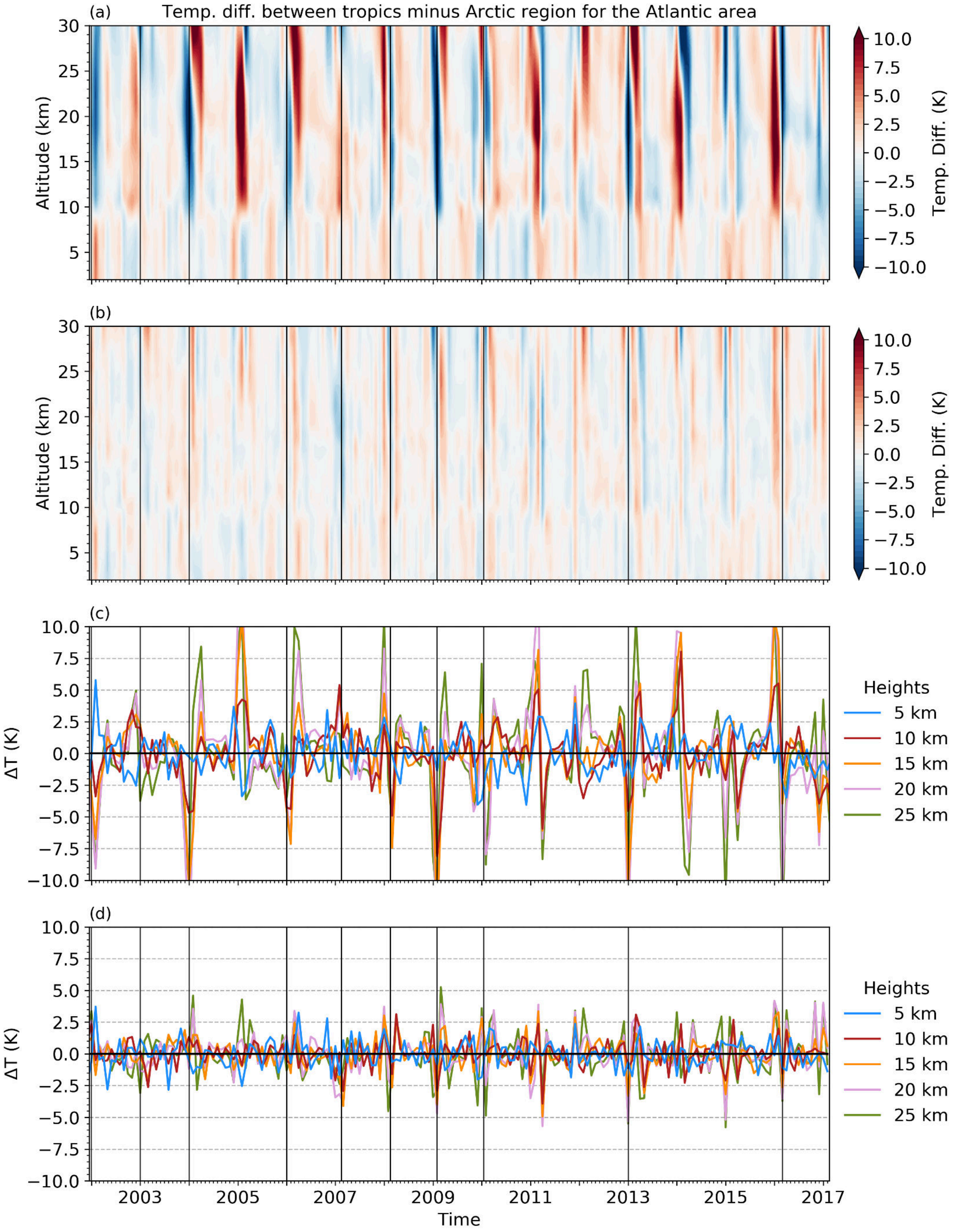

**Figure A.6.:** Same as Fig.A.5, but for the ERAI data set.

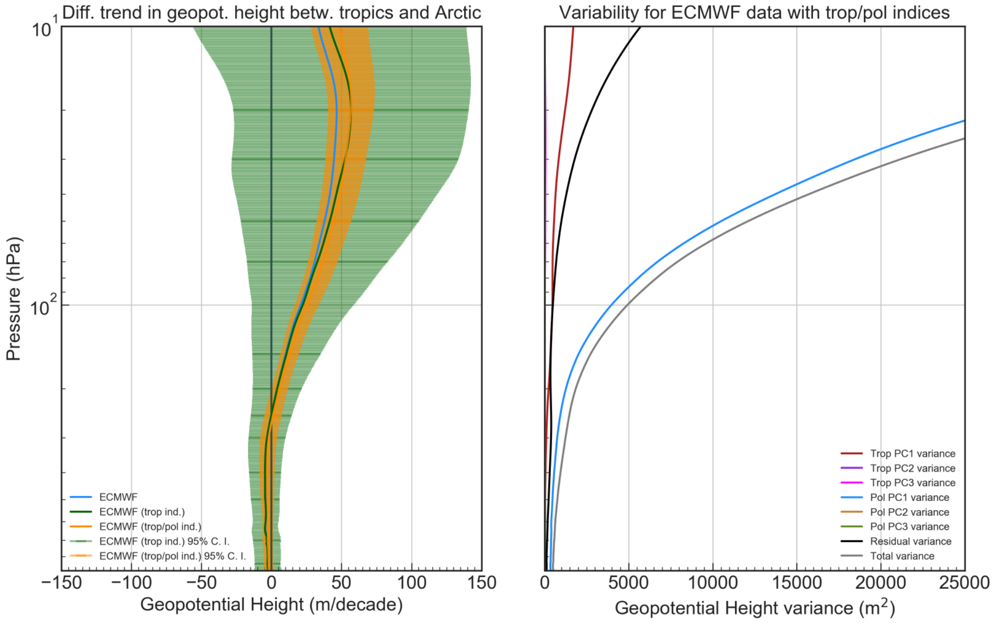

(a) Zonal mean

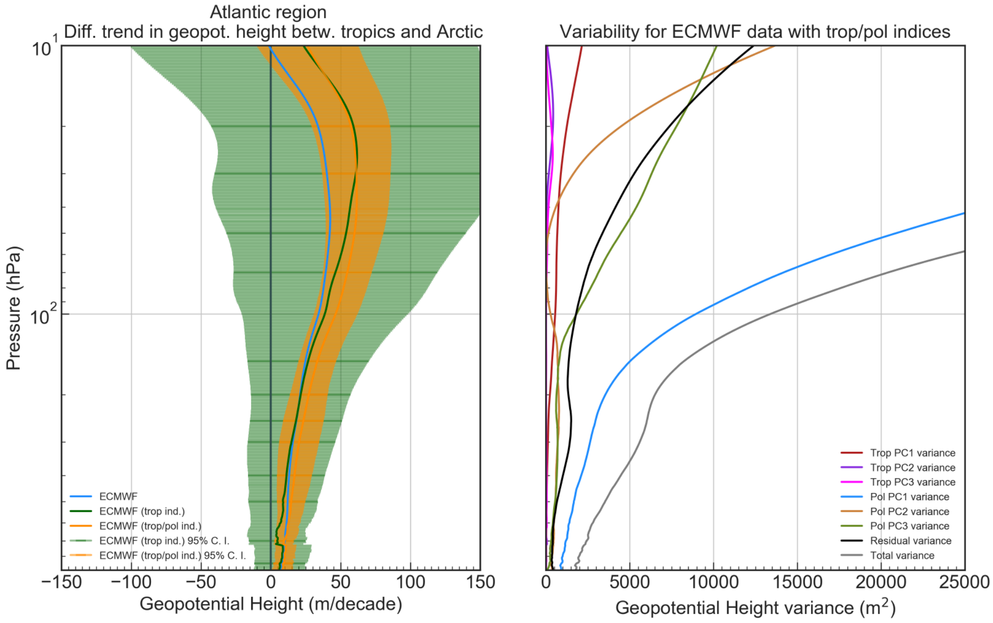

(b) Atlantic region

**Figure A.7.:** Same as 5.19 but for ECMWF data.

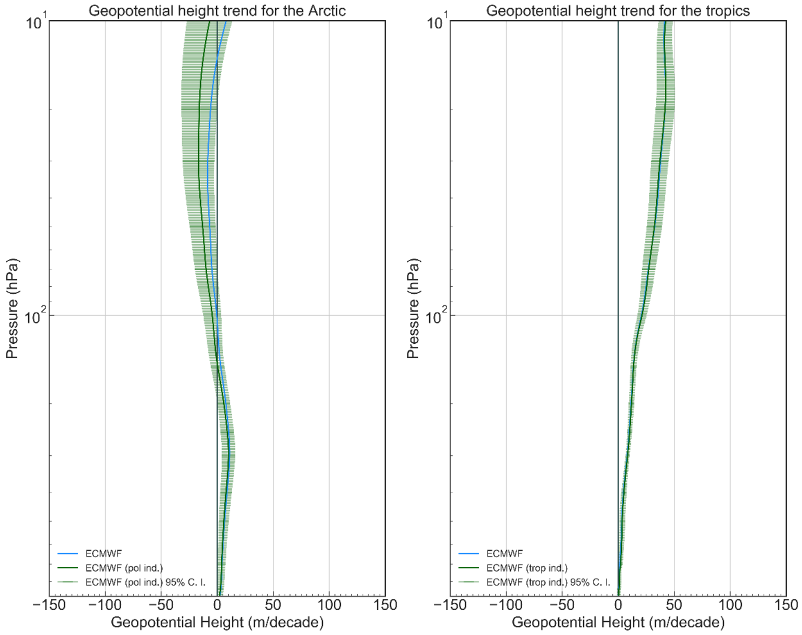

(a) Arctic (b) Tropics

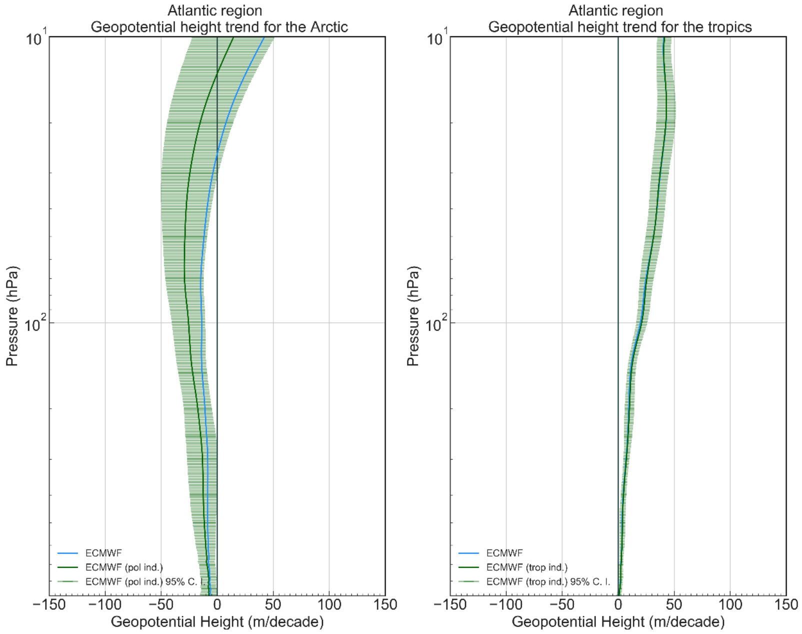

(c) Atlantic, Arctic (d) Atlantic, Tropics

**Figure A.8.:** Same as 5.20 but for ECMWF data.

# B. Error analysis

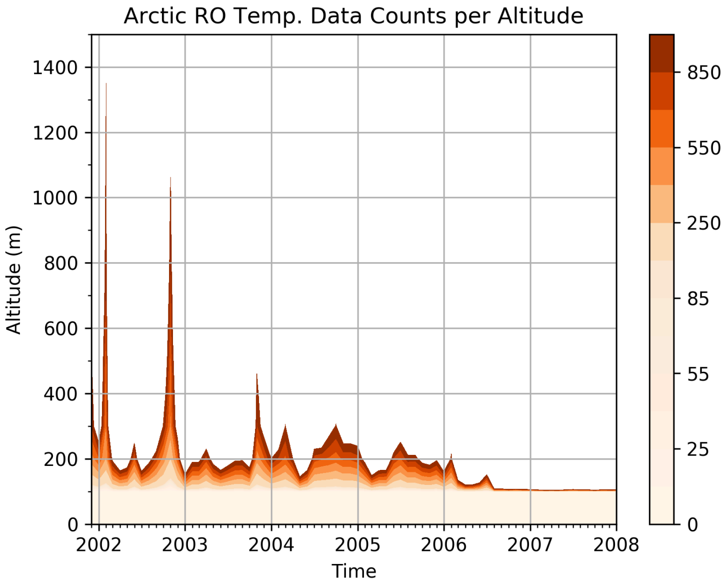

(a)

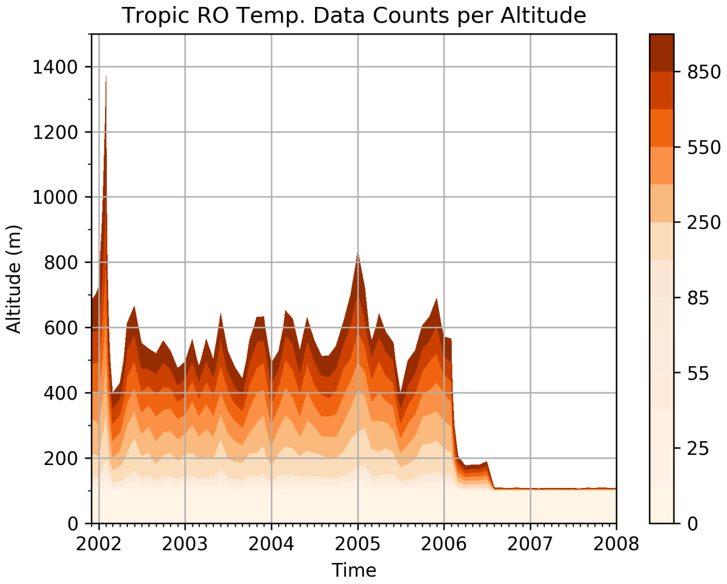

(b)

**Figure B.1.:** Measurement points for the Arctic (a) and the tropical region (b) between 2002 and 2017 from the surface to 5 km height. In color all points with less than 1000 counts, the white area contains more than 1000 counts.

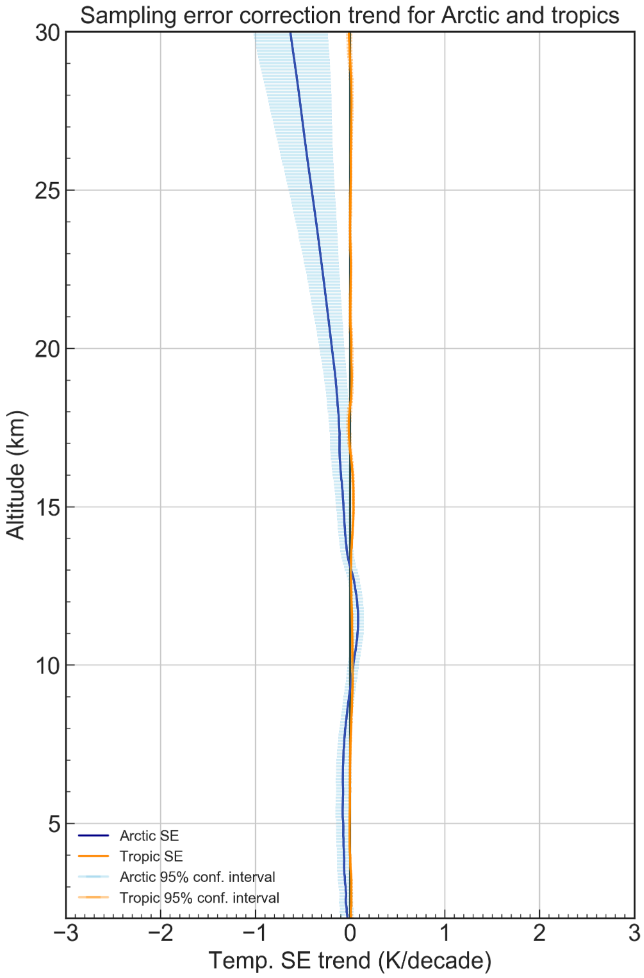

**Figure B.2.:** Tropical (30° S to 30° N) (orange) and Arctic (60° N to 85° N) (blue) Sampling Error (SE) trends for RO temperature data.

Before the RO data is regressed, the SE is corrected. In Fig. B.2 the SE correction trend for the tropics (30° S to 30° N) and the Arctic region (60° N to 85° N) is shown.

For the tropics, the SE correction is generally very small ($< 0.01\,\mathrm{K/decade}$). At higher latitudes, the atmospheric variability increases, resulting in a strong negative SE correction trend up to 0.8 K/decade in the lower stratosphere (Fig. B.2). Due to this correction, the Arctic temperature trend becomes more positive in the lower stratosphere while the tropical trend is not influenced.

As visible in Fig. B.3, strong SE corrections in the northern hemisphere are mostly needed between 62.5° N and 82.5° N above 20 km. With more climate satellite mission launched, the SE correction gets reduced. When analyzing the SE for each month separately (Fig. B.4 to Fig. B.18), a stronger SE correction at higher latitudes in the winter months is visible, especially during SSW events.

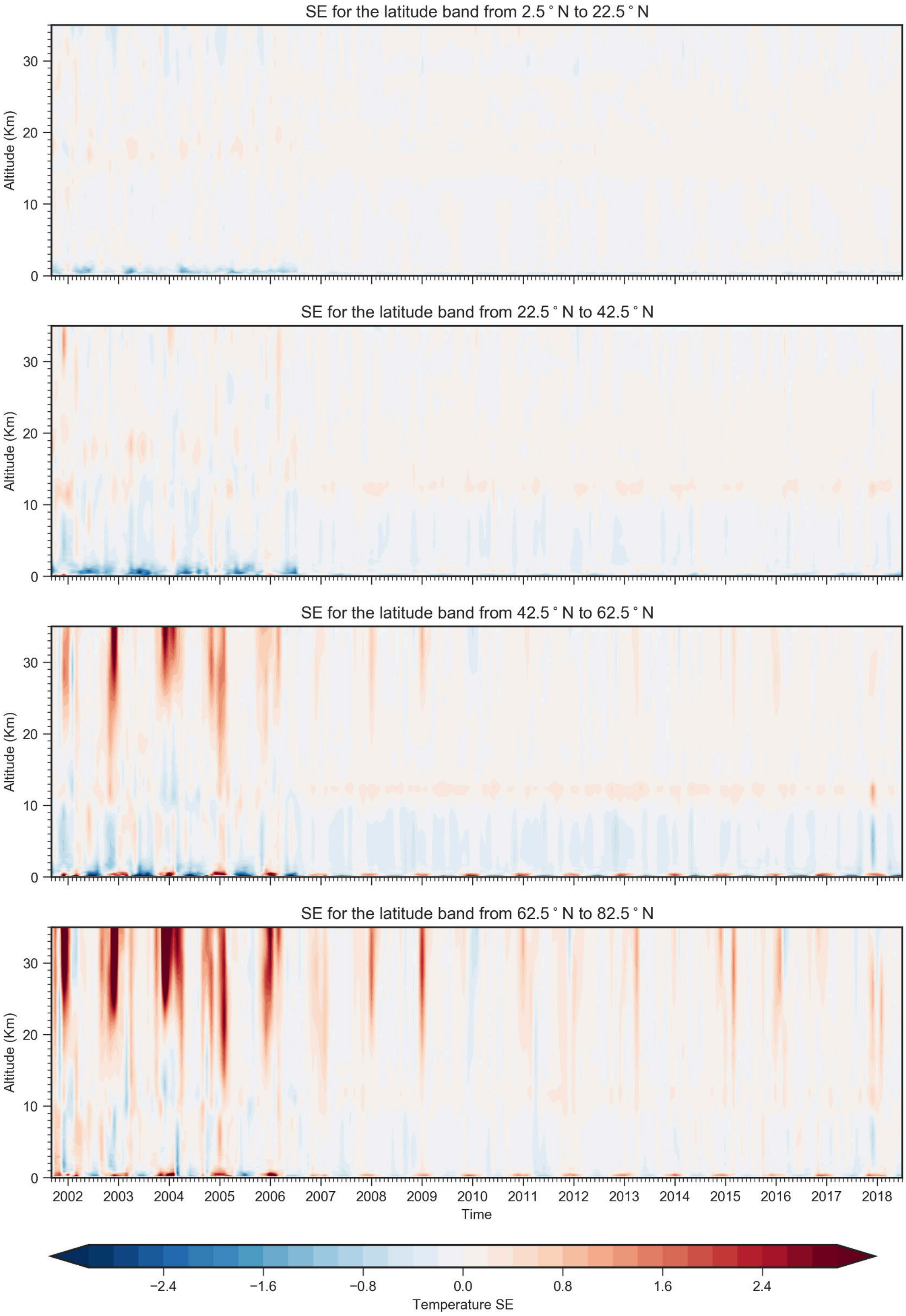

**Figure B.3.:** Sampling error for the RO temperature anomaly data on the northern hemisphere for different latitude bands

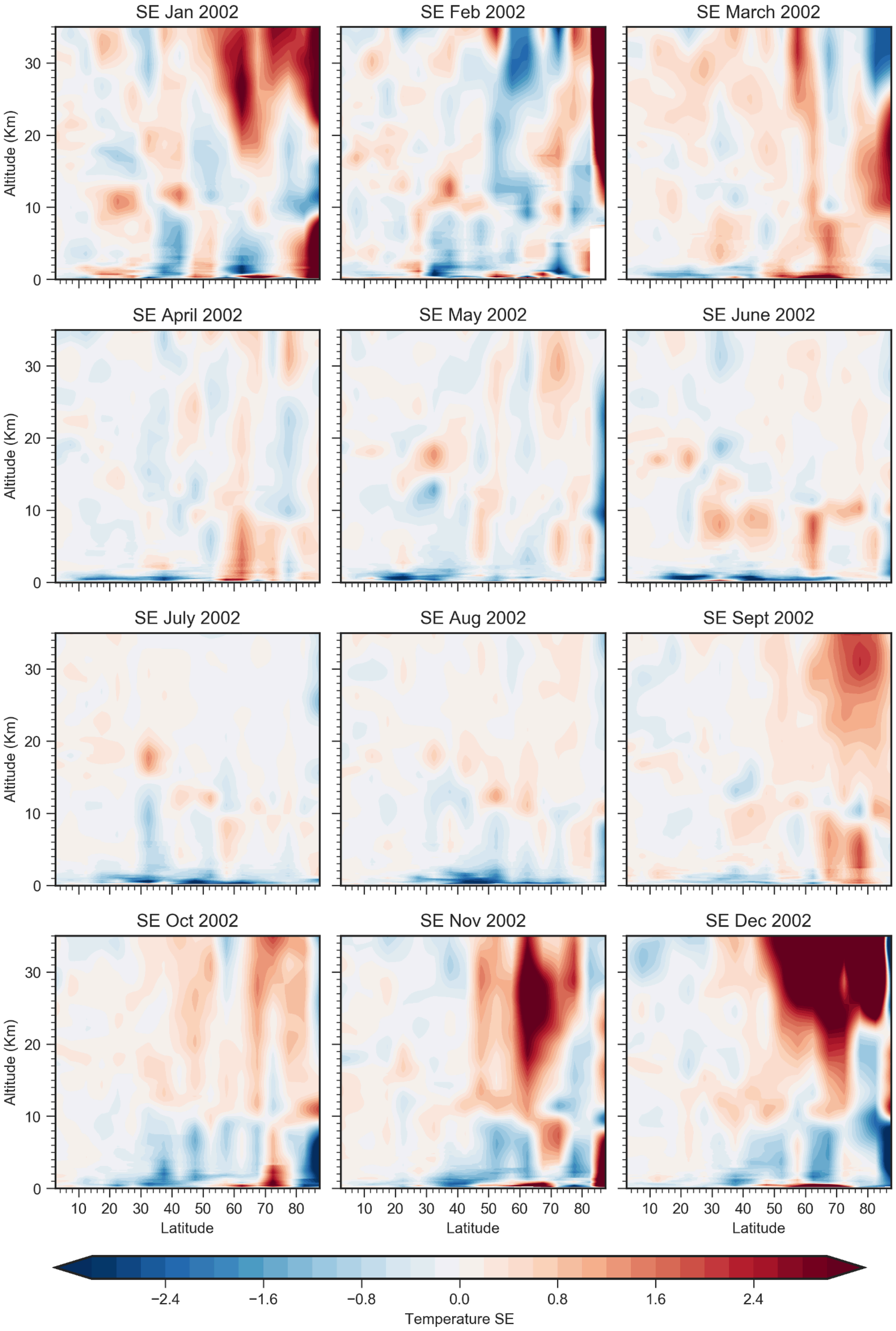

**Figure B.4.:** Sampling Error for the RO temperature anomaly data on the northern hemisphere for all months in 2002

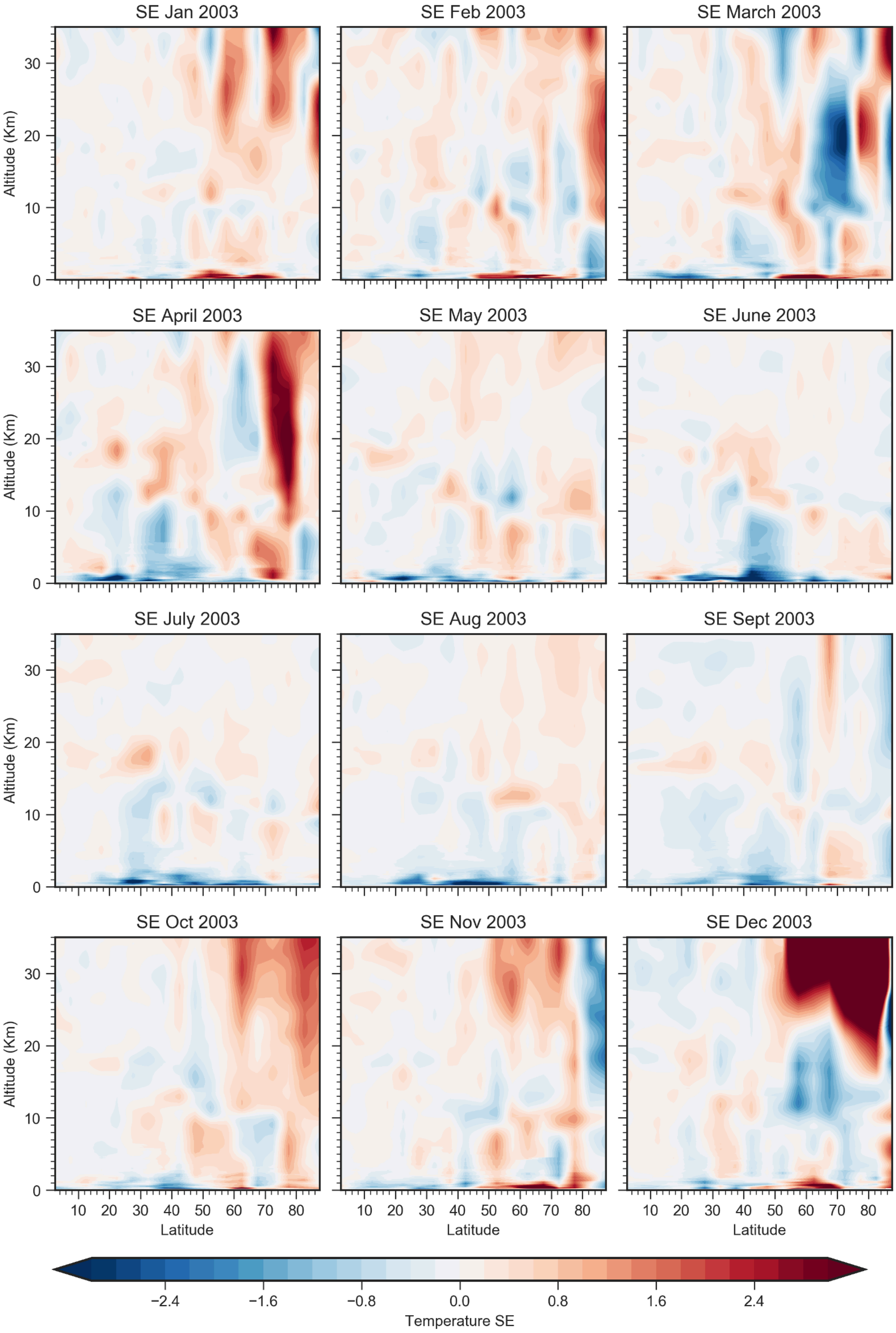

**Figure B.5.:** Sampling Error for the RO temperature anomaly data on the northern hemisphere for all months in 2003

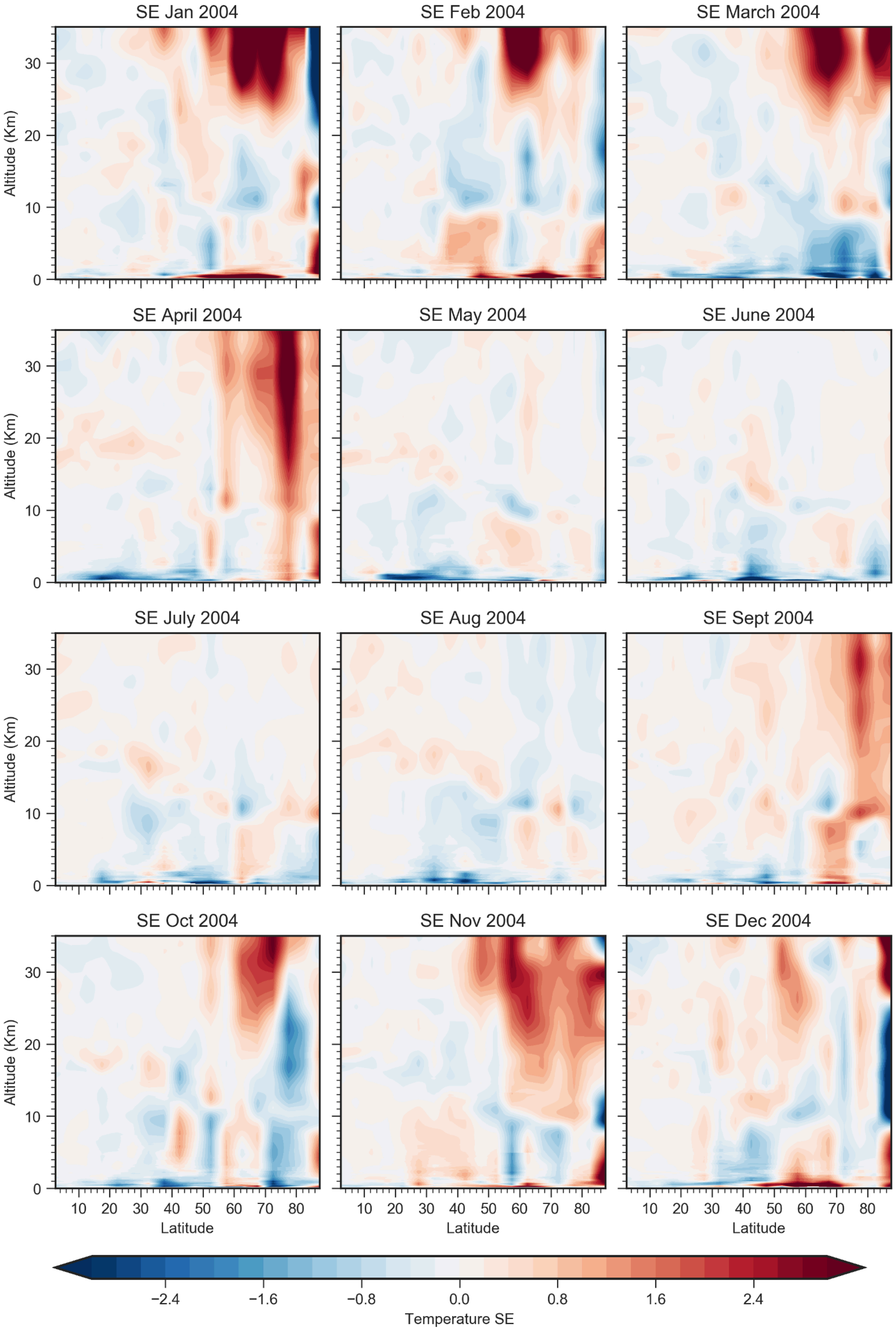

**Figure B.6.:** Sampling Error for the RO temperature anomaly data on the northern hemisphere for all months in 2004

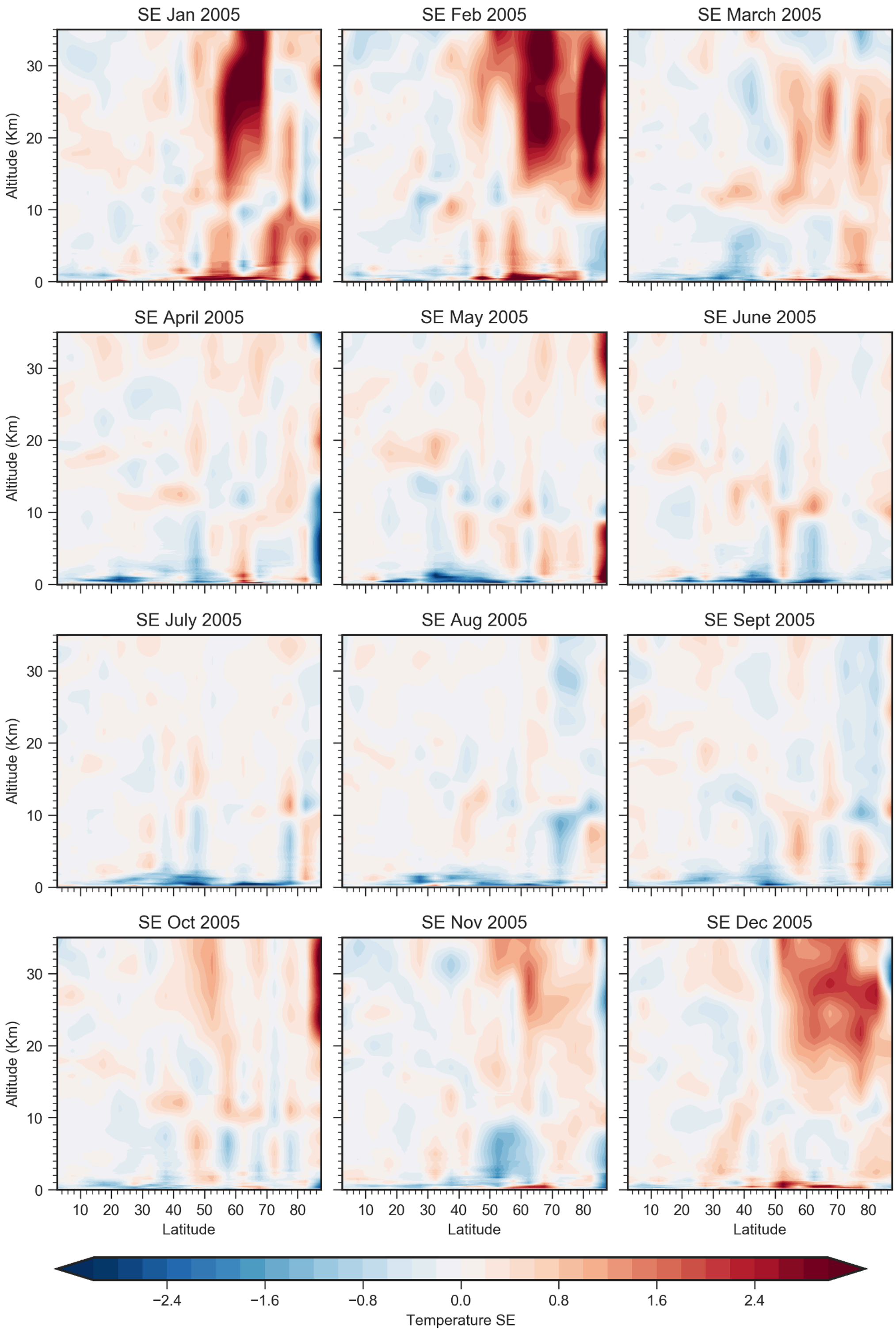

**Figure B.7.:** Sampling Error for the RO temperature anomaly data on the northern hemisphere for all months in 2005

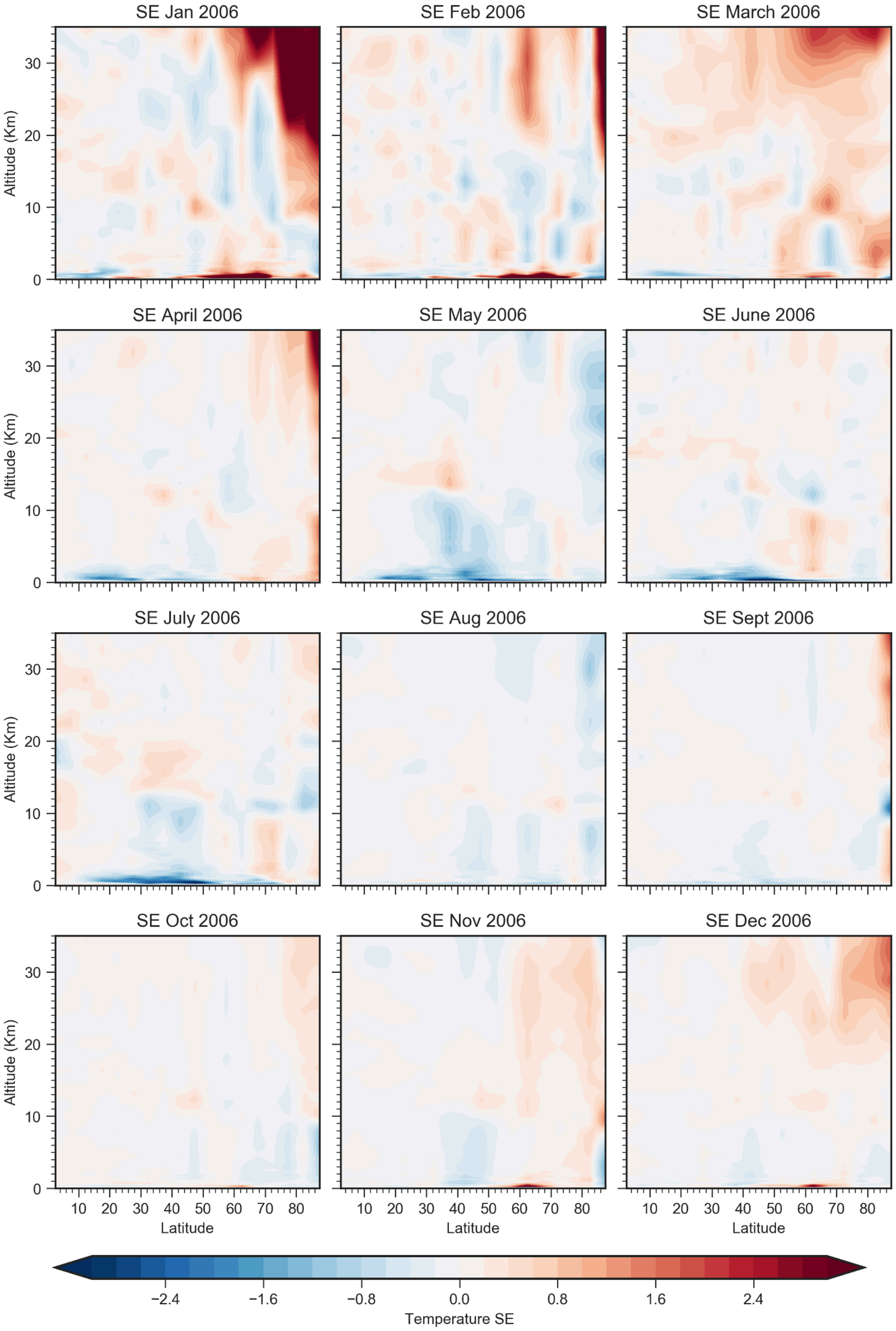

**Figure B.8.:** Sampling Error for the RO temperature anomaly data on the northern hemisphere for all months in 2006

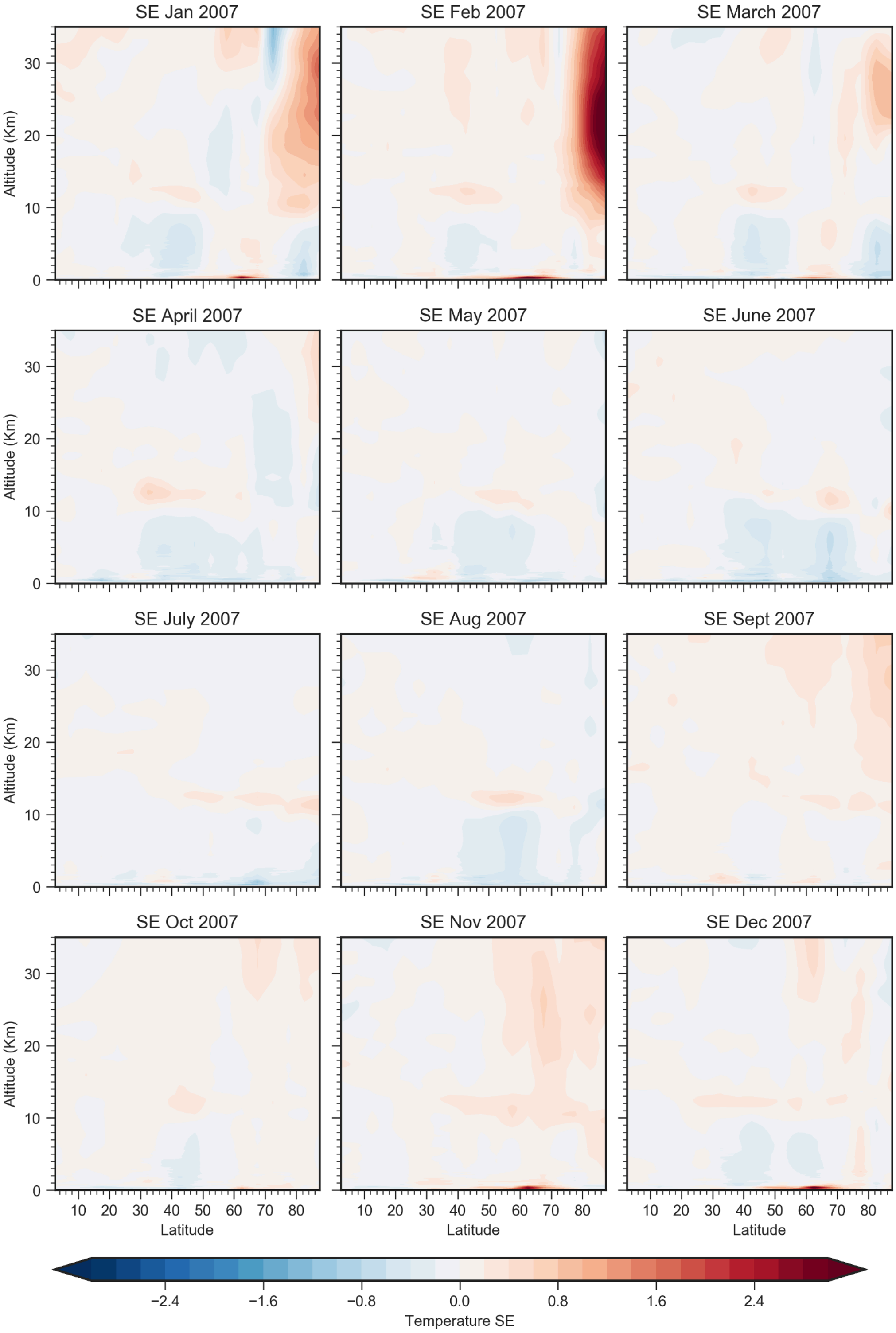

**Figure B.9.:** Sampling Error for the RO temperature anomaly data on the northern hemisphere for all months in 2007

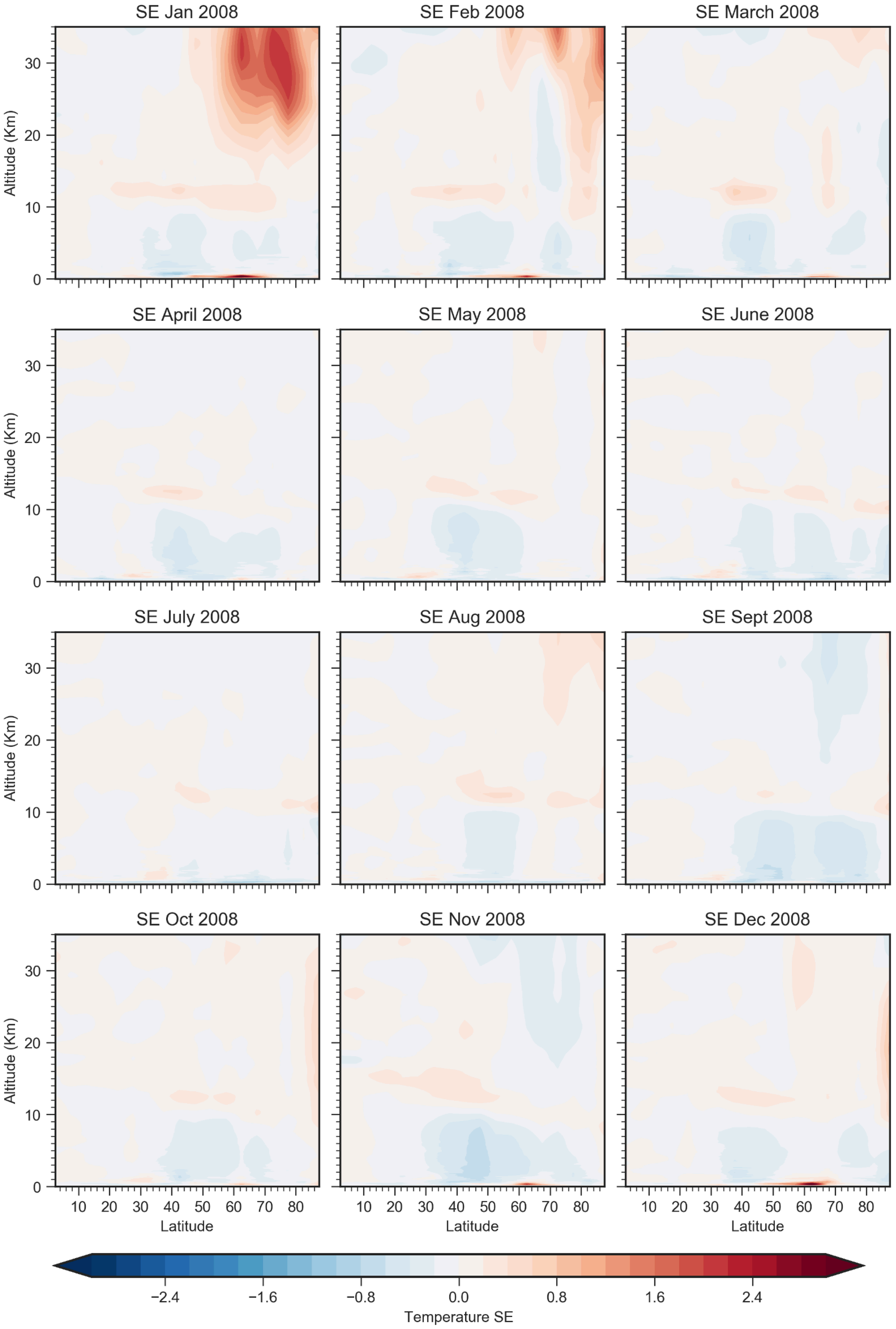

**Figure B.10.:** Sampling Error for the RO temperature anomaly data on the northern hemisphere for all months in 2008

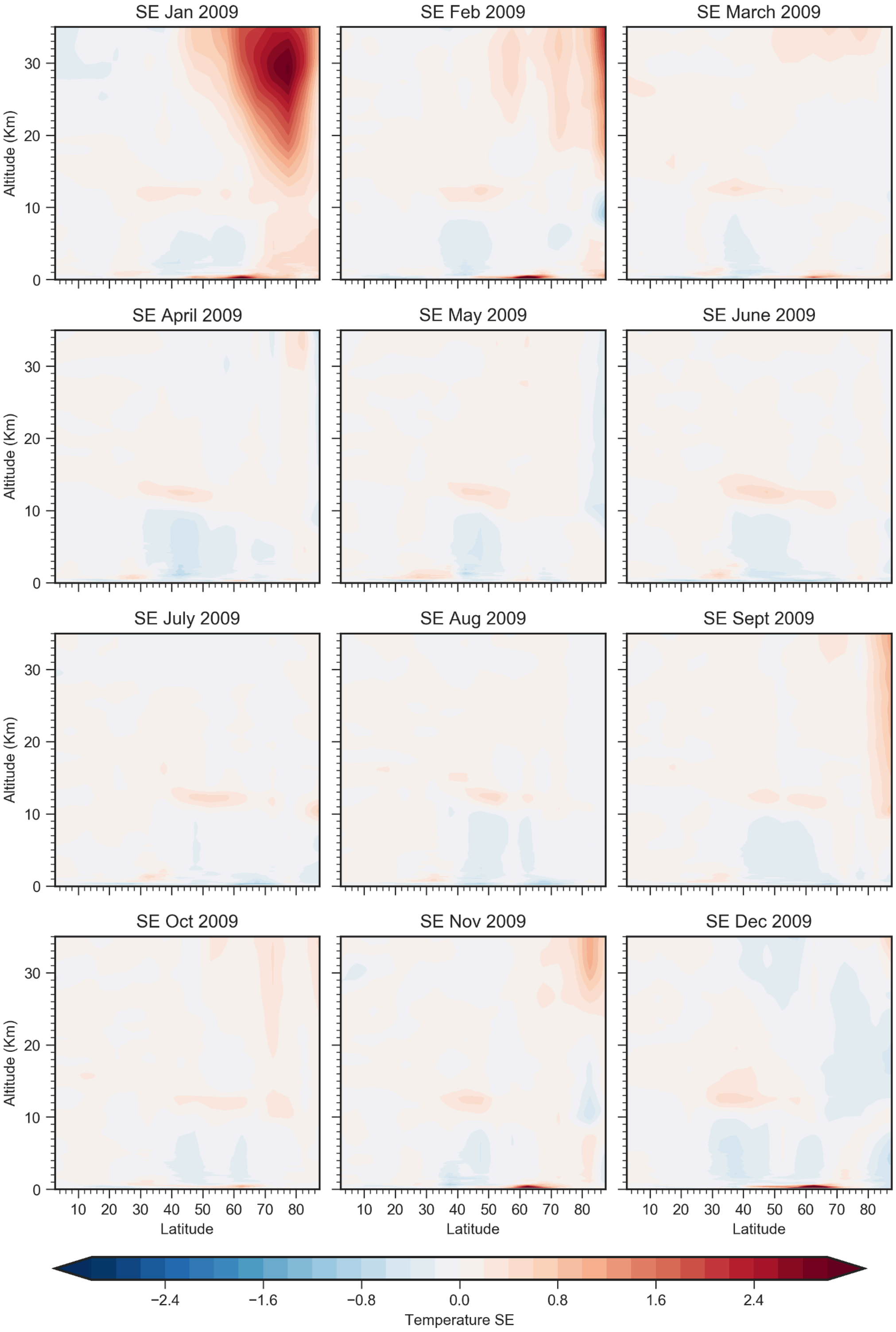

**Figure B.11.:** Sampling Error for the RO temperature anomaly data on the northern hemisphere for all months in 2009

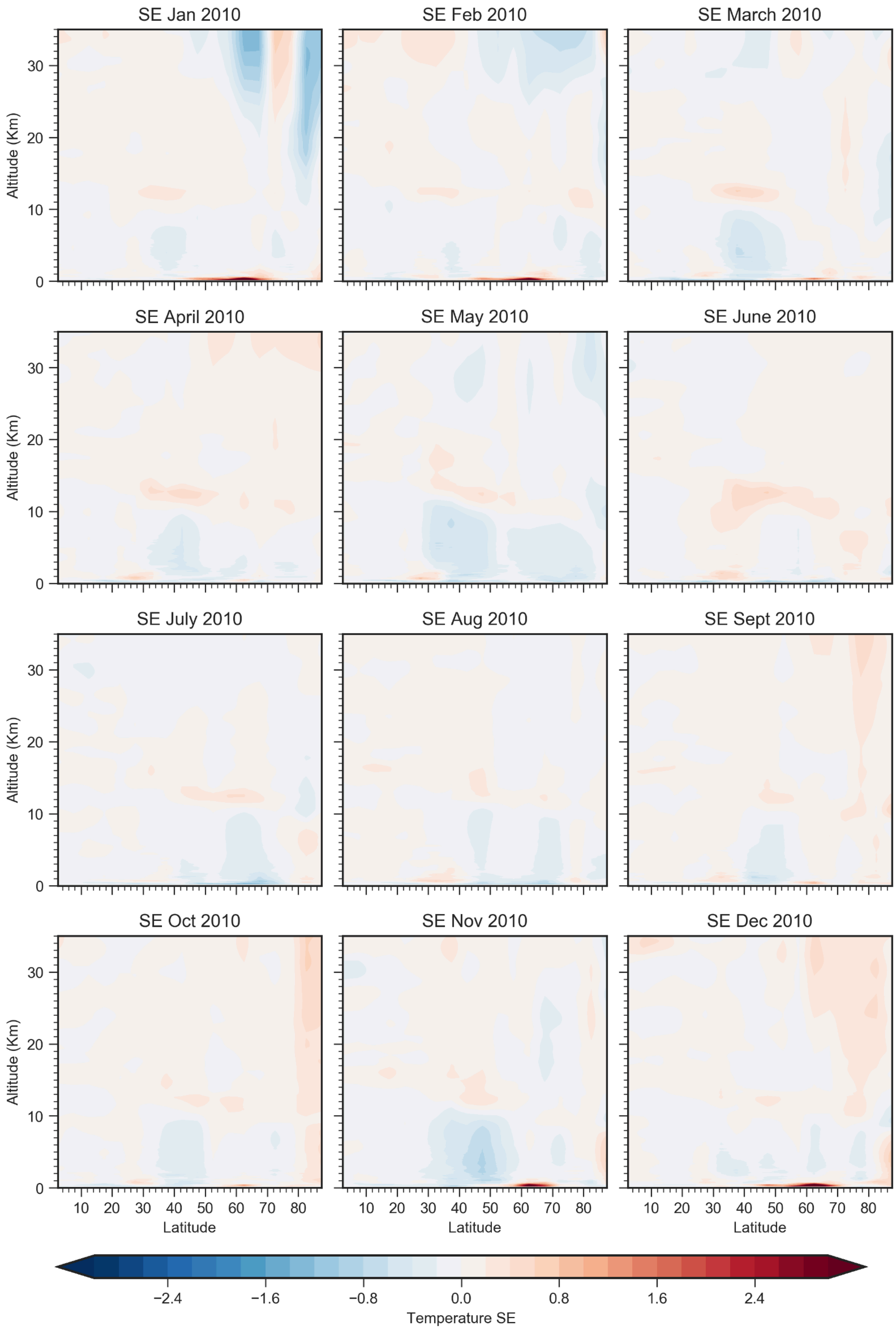

**Figure B.12.:** Sampling Error for the RO temperature anomaly data on the northern hemisphere for all months in 2010

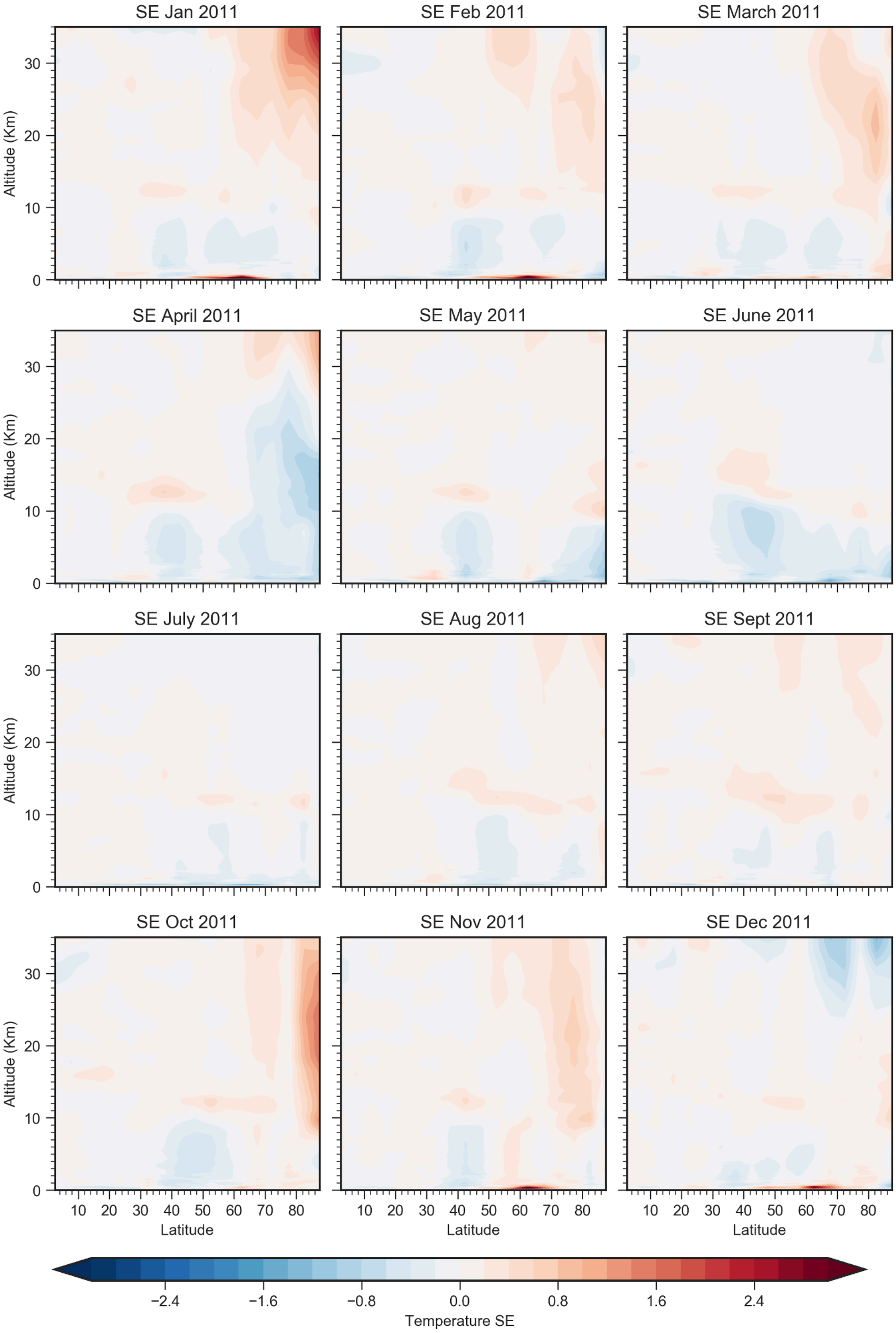

**Figure B.13.:** Sampling Error for the RO temperature anomaly data on the northern hemisphere for all months in 2011

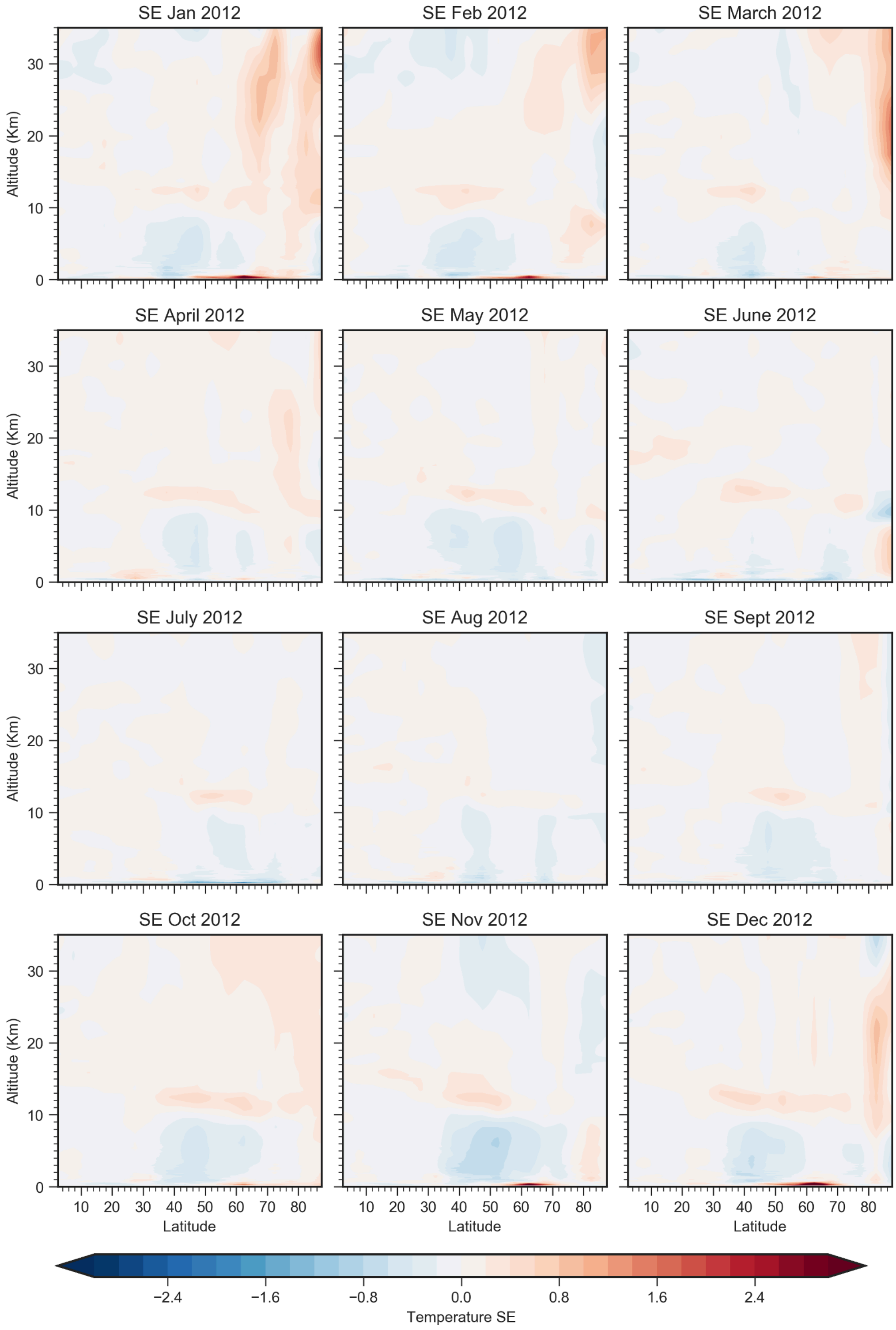

**Figure B.14.:** Sampling Error for the RO temperature anomaly data on the northern hemisphere for all months in 2012

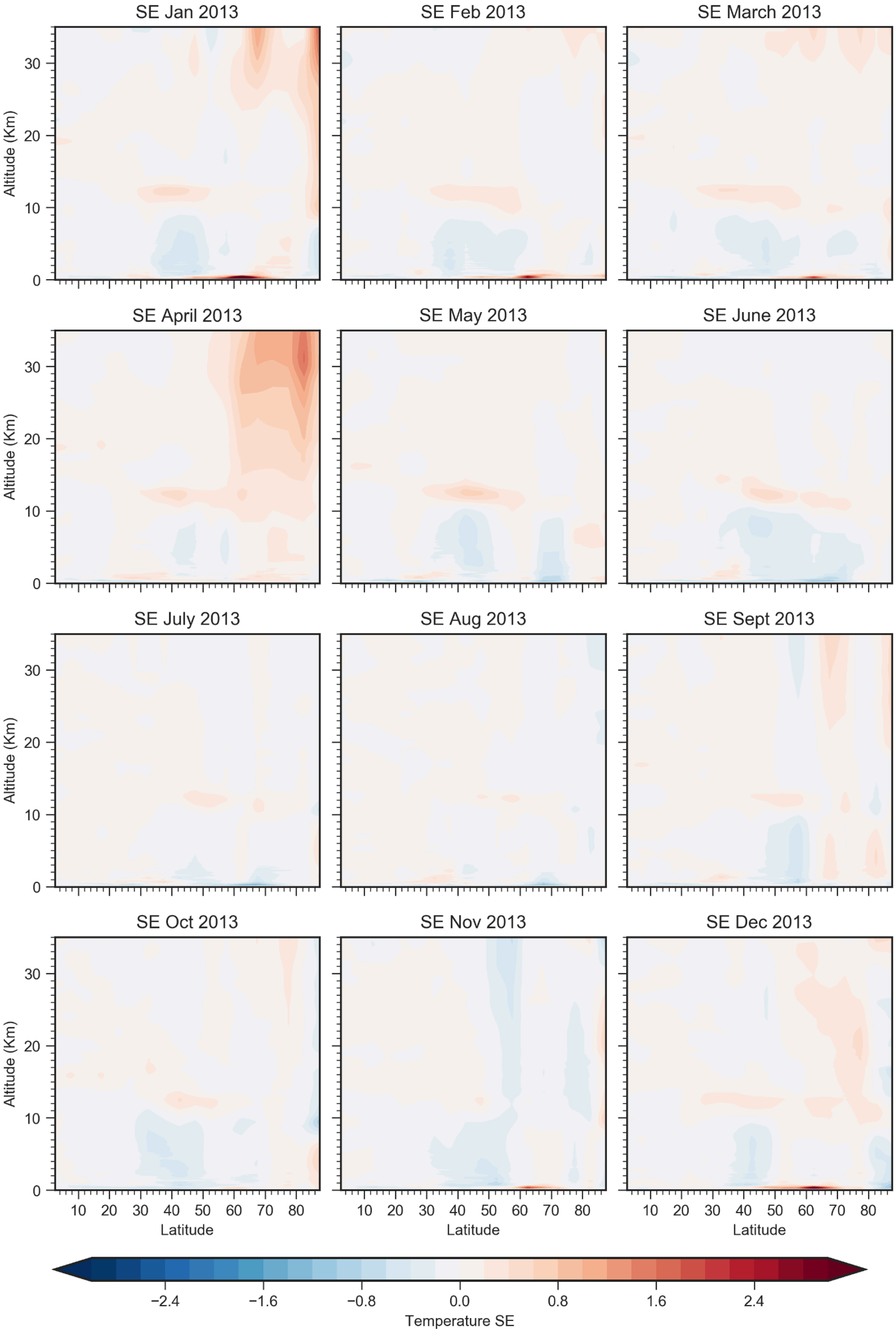

**Figure B.15.:** Sampling Error for the RO temperature anomaly data on the northern hemisphere for all months in 2013

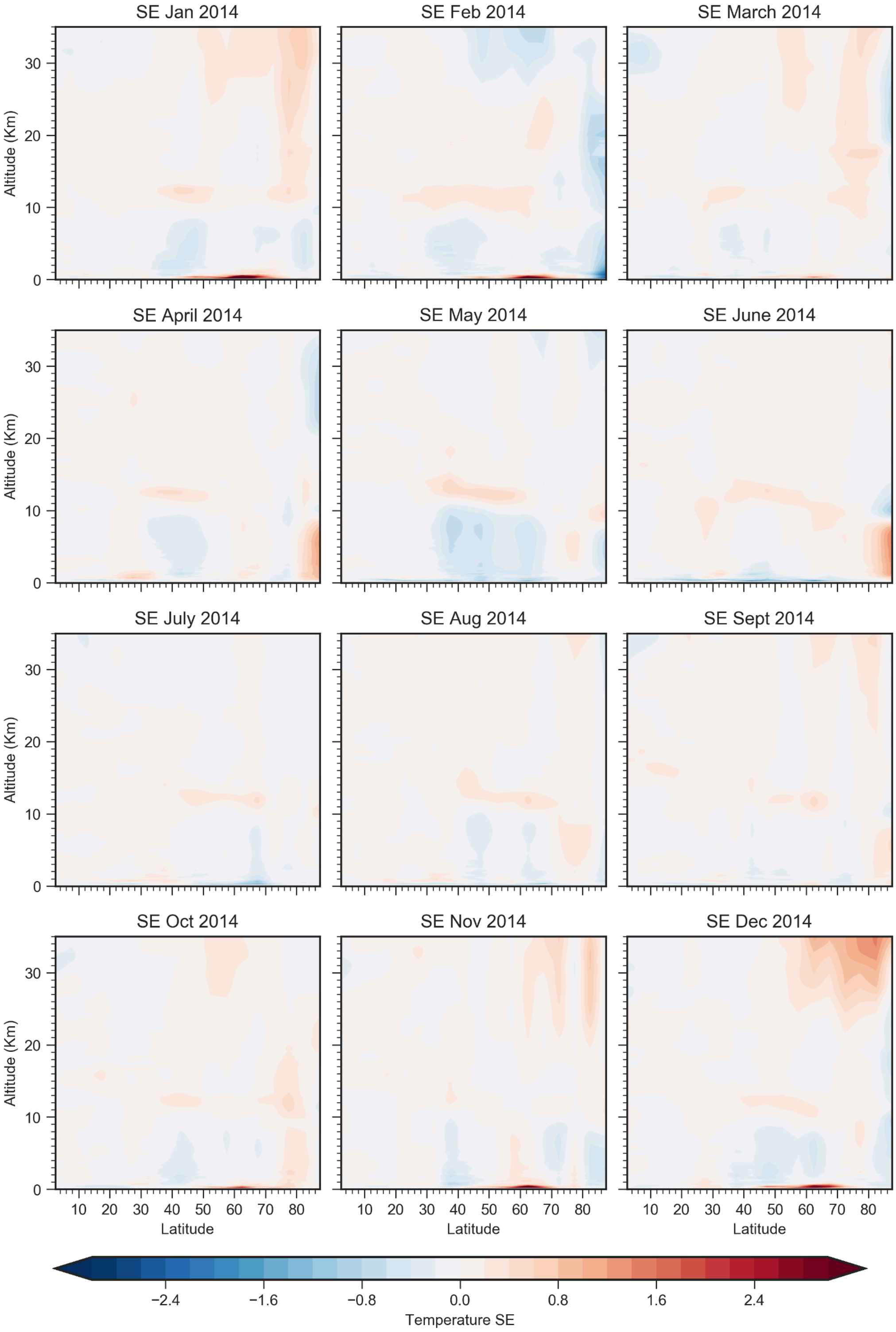

**Figure B.16.:** Sampling Error for the RO temperature anomaly data on the northern hemisphere for all months in 2014

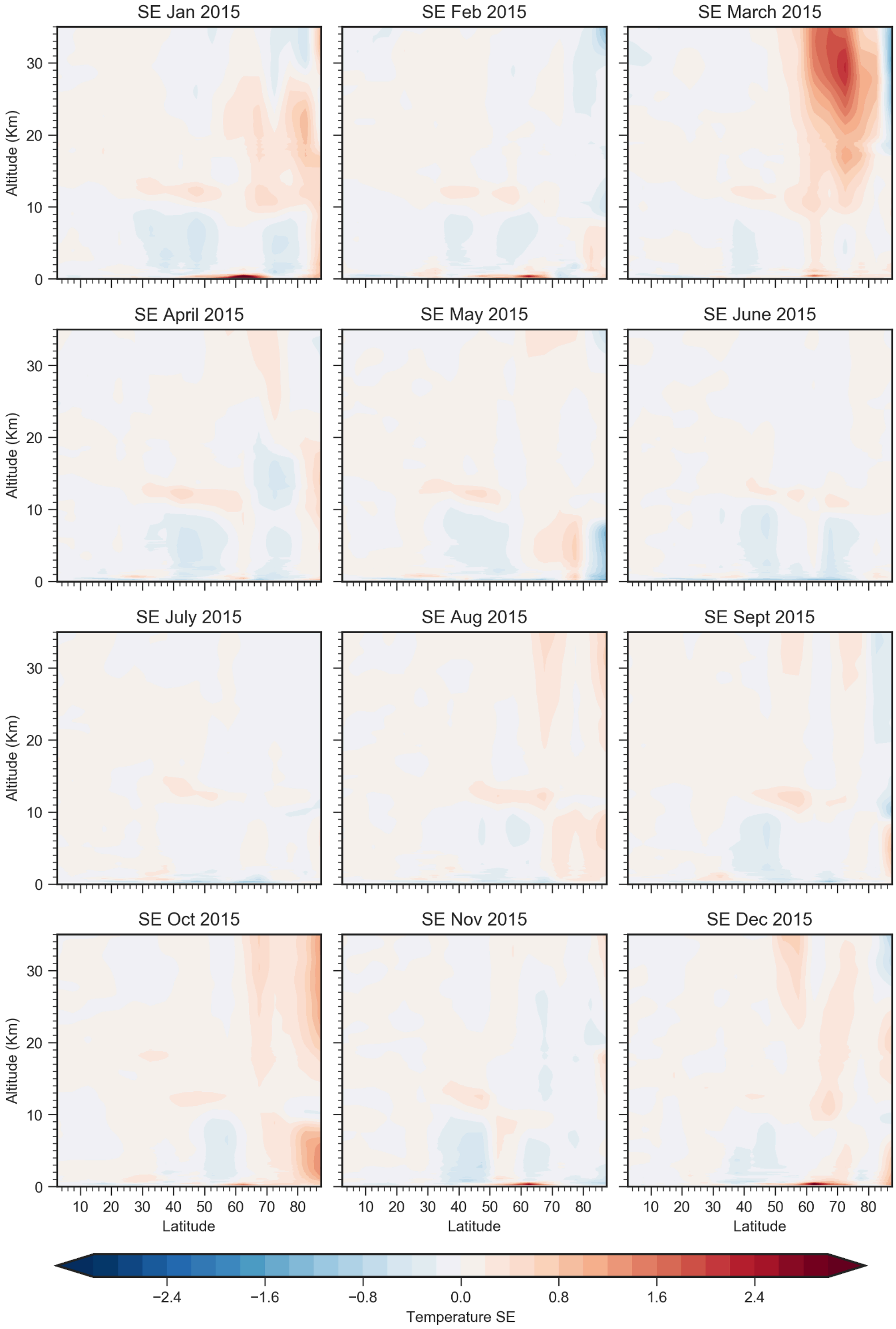

**Figure B.17.:** Sampling Error for the RO temperature anomaly data on the northern hemisphere for all months in 2015

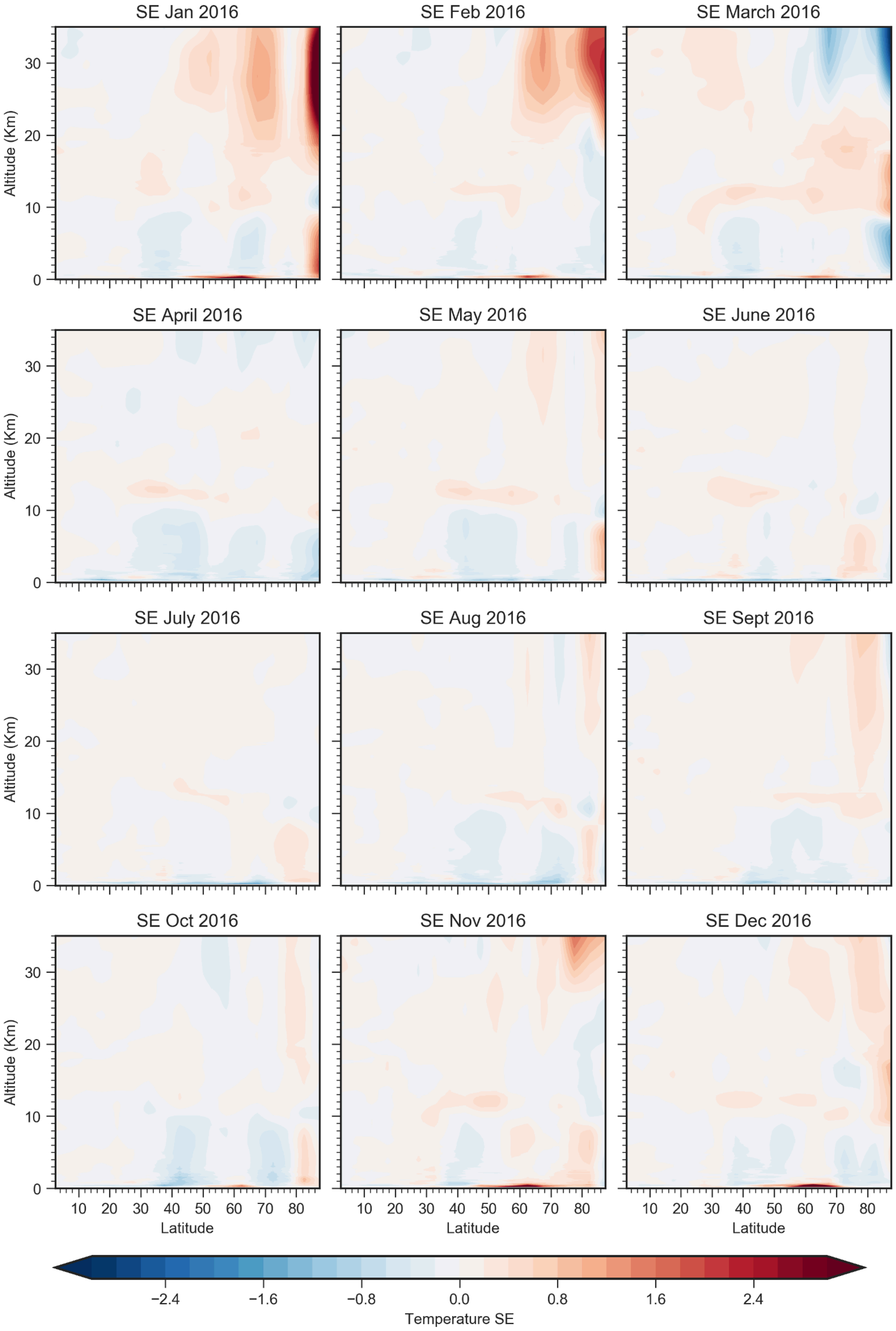

**Figure B.18.:** Sampling Error for the RO temperature anomaly data on the northern hemisphere for all months in 2016

# C. Storm tracks in ECMWF analyses in 6-hourly resolution

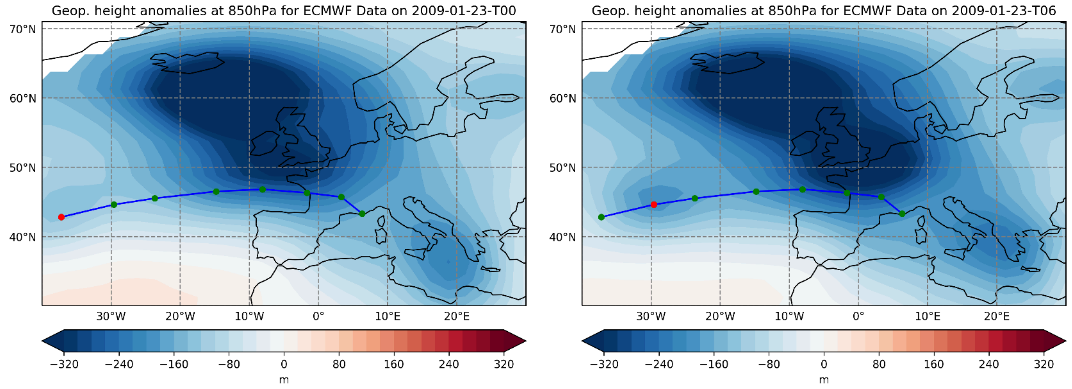
Geop. height anomalies at 850hPa for ECMWF Data on 2009-01-23-T00
Geop. height anomalies at 850hPa for ECMWF Data on 2009-01-23-T06
70°N
60°N
50°N
40°N
30°W
20°W
10°W
0°
10°E
20°E
−320
−240
−160
−80
0
80
160
240
320
m

(a) 01-23 T00 850 hPa

(b) 01-23 T06 850 hPa

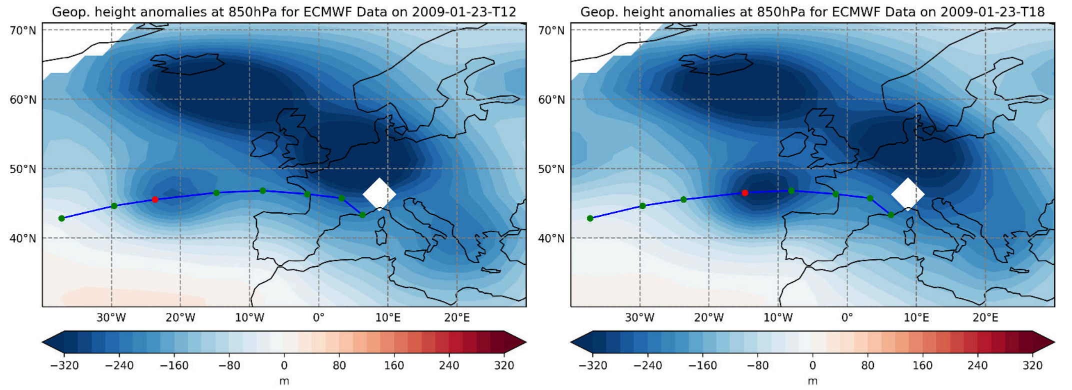
Geop. height anomalies at 850hPa for ECMWF Data on 2009-01-23-T12
Geop. height anomalies at 850hPa for ECMWF Data on 2009-01-23-T18
70°N
60°N
50°N
40°N
30°W
20°W
10°W
0°
10°E
20°E
−320
−240
−160
−80
0
80
160
240
320
m

(c) 01-23 T12 850 hPa

(d) 01-23 T18 850 hPa

**Figure C.1.:** Geopotential height anomalies at 850 hPa for ECMWF data. Difference between the six-hourly interval data and the monthly average geopotential height for all January months from 2006 to 2016. The blue line indicates the surface track of Storm Klaus for the time period between 0000UTC 23 January 2009 and 18UTC 24 January 2009. The position of the storm is marked with a filled red circle (Coordinates taken from Liberato et al. (2011)).

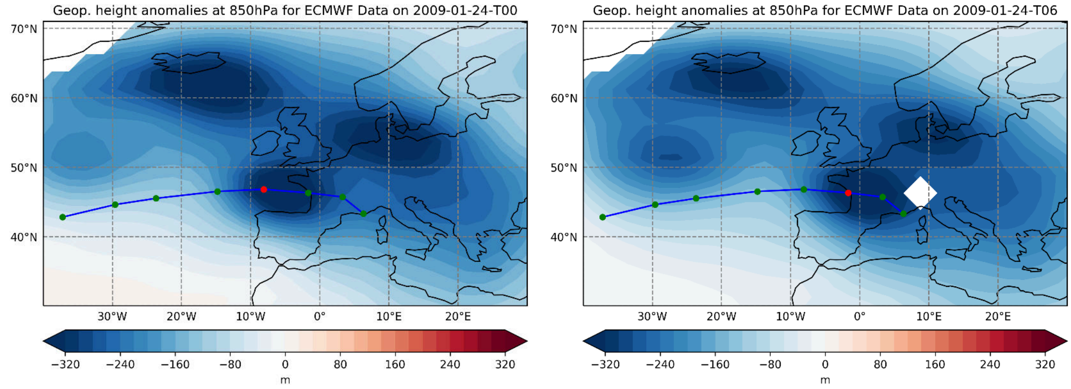
Geop. height anomalies at 850hPa for ECMWF Data on 2009-01-24-T00
Geop. height anomalies at 850hPa for ECMWF Data on 2009-01-24-T06
70°N
60°N
50°N
40°N
30°W
20°W
10°W
0°
10°E
20°E
−320
−240
−160
−80
0
80
160
240
320
m

(a) 01-24 T00 850 hPa (b) 01-24 T06 850 hPa

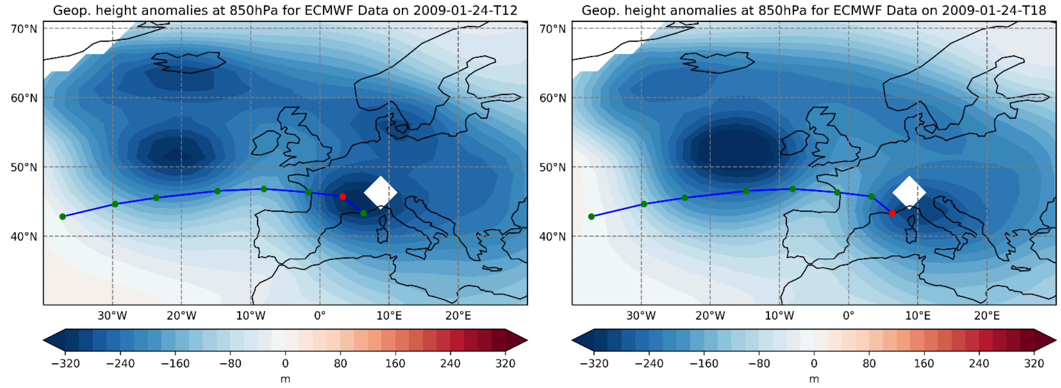
Geop. height anomalies at 850hPa for ECMWF Data on 2009-01-24-T12
Geop. height anomalies at 850hPa for ECMWF Data on 2009-01-24-T18
70°N
60°N
50°N
40°N
30°W
20°W
10°W
0°
10°E
20°E
−320
−240
−160
−80
0
80
160
240
320
m

(c) 01-24 T12 850 hPa (d) 01-24 T18 850 hPa

**Figure C.2.:** Same as Fig. C.1, but for the following day.

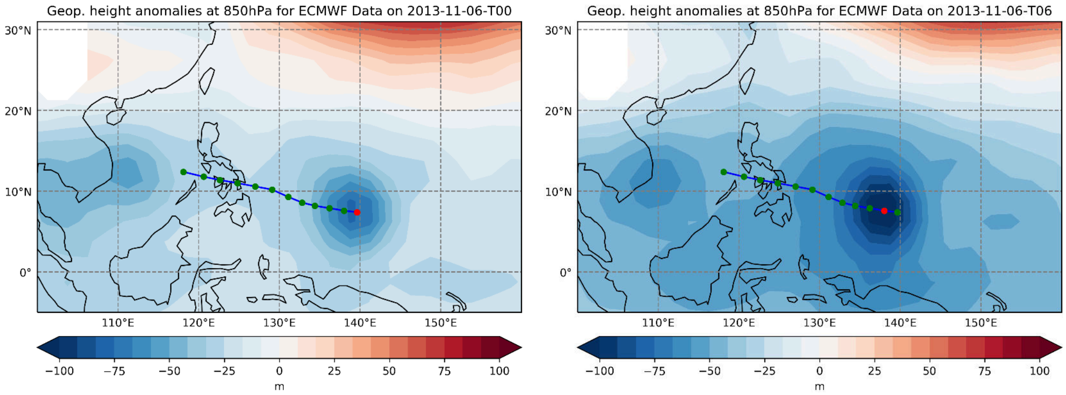
Geop. height anomalies at 850hPa for ECMWF Data on 2013-11-06-T00
Geop. height anomalies at 850hPa for ECMWF Data on 2013-11-06-T06
30°N
20°N
10°N
0°
110°E
120°E
130°E
140°E
150°E
−100
−75
−50
−25
0
25
50
75
100
m

(a) 11-06 T00 850 hPa

(b) 11-06 T06 850 hPa

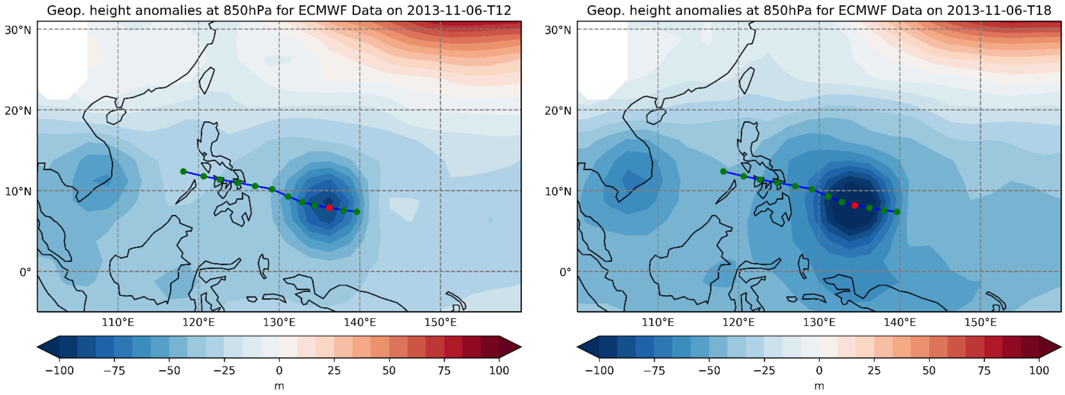
Geop. height anomalies at 850hPa for ECMWF Data on 2013-11-06-T12
Geop. height anomalies at 850hPa for ECMWF Data on 2013-11-06-T18
30°N
20°N
10°N
0°
110°E
120°E
130°E
140°E
150°E
−100
−75
−50
−25
0
25
50
75
100
m

(c) 11-06 T12 850 hPa

(d) 11-06 T18 850 hPa

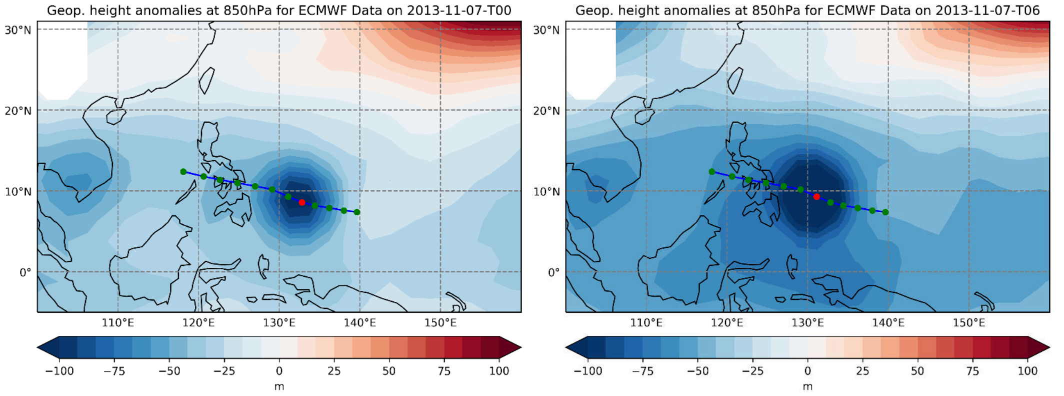
Geop. height anomalies at 850hPa for ECMWF Data on 2013-11-07-T00
Geop. height anomalies at 850hPa for ECMWF Data on 2013-11-07-T06
30°N
20°N
10°N
0°
110°E
120°E
130°E
140°E
150°E
−100
−75
−50
−25
0
25
50
75
100
m

(e) 11-07 T00 850 hPa

(f) 11-07 T06 850 hPa

**Figure C.3.:** Geopotential height anomaly at 850 hPa for ECMWF data. Difference between the six-hourly interval data and the monthly average geopotential height for all November months from 2006 to 2016. The blue line indicates the surface track of Storm Haiyan for the time period between 0000UTC 06 November 2013 and 1800UTC 08 November 2013. The position of the storm is marked with a filled red circle.(retrieved from the hurricane and tropical cyclones archive www.wunderground.com/hurricane/hurrarchive.asp, last visit on Sep 21, 2018).

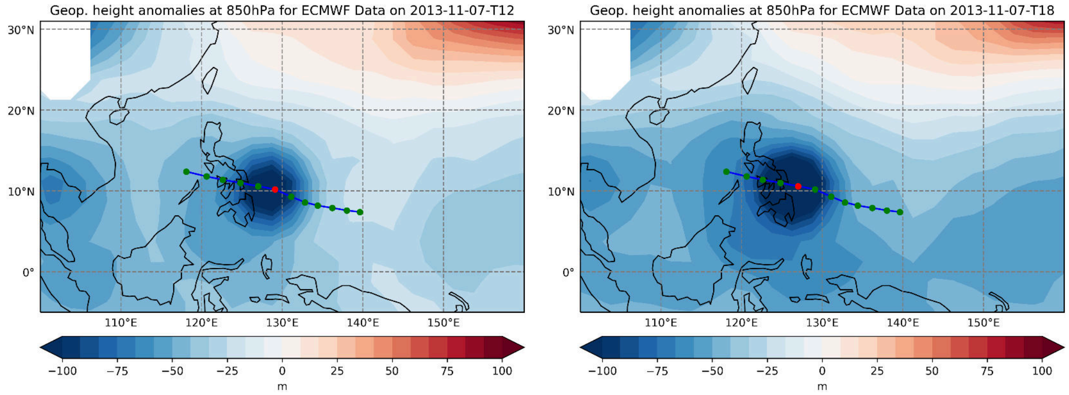
Geop. height anomalies at 850hPa for ECMWF Data on 2013-11-07-T12
Geop. height anomalies at 850hPa for ECMWF Data on 2013-11-07-T18
30°N
20°N
10°N
0°
110°E
120°E
130°E
140°E
150°E
−100
−75
−50
−25
0
25
50
75
100
m

(a) 11-07 T12 850 hPa (b) 11-07 T18 850 hPa

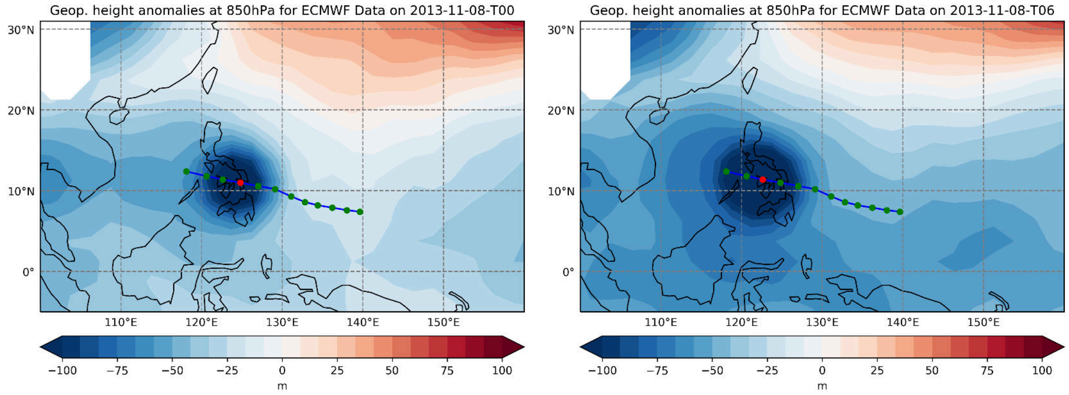
Geop. height anomalies at 850hPa for ECMWF Data on 2013-11-08-T00
Geop. height anomalies at 850hPa for ECMWF Data on 2013-11-08-T06
30°N
20°N
10°N
0°
110°E
120°E
130°E
140°E
150°E
−100
−75
−50
−25
0
25
50
75
100
m

(c) 11-08 T00 850 hPa (d) 11-08 T06 850 hPa

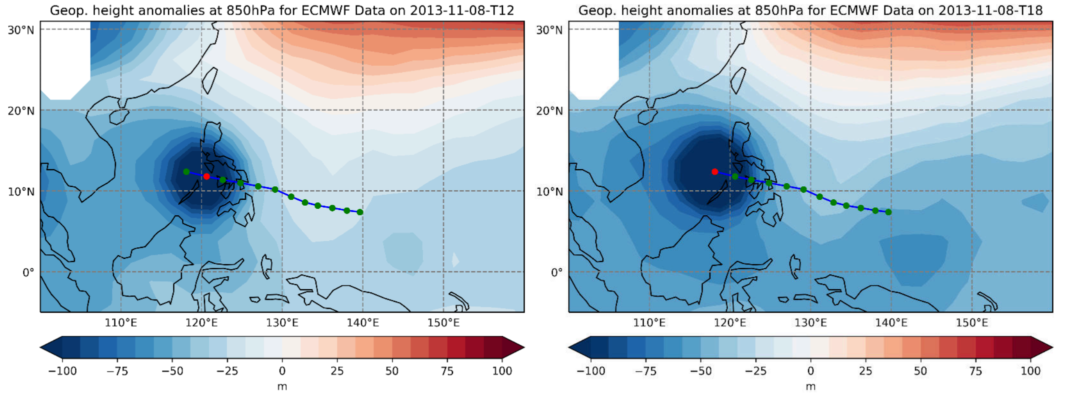
Geop. height anomalies at 850hPa for ECMWF Data on 2013-11-08-T12
Geop. height anomalies at 850hPa for ECMWF Data on 2013-11-08-T18
30°N
20°N
10°N
0°
110°E
120°E
130°E
140°E
150°E
−100
−75
−50
−25
0
25
50
75
100
m

(e) 11-08 T12 850 hPa (f) 11-08 T18 850 hPa

**Figure C.4.:** Same as for Fig. C.3, but for the following day.

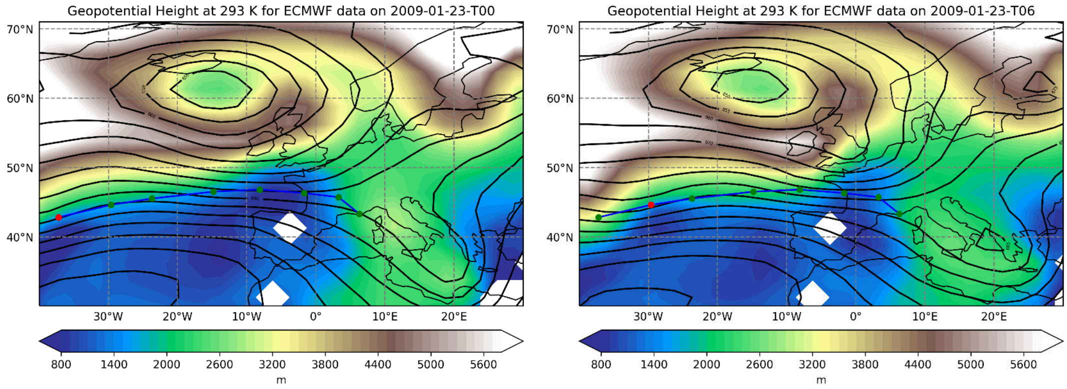
Geopotential Height at 293 K for ECMWF data on 2009-01-23-T00
Geopotential Height at 293 K for ECMWF data on 2009-01-23-T06
70°N
60°N
50°N
40°N
30°W
20°W
10°W
0°
10°E
20°E
800
1400
2000
2600
3200
3800
4400
5000
5600
m

(a) 01-23 T00 293 K (b) 01-23 T06 293 K

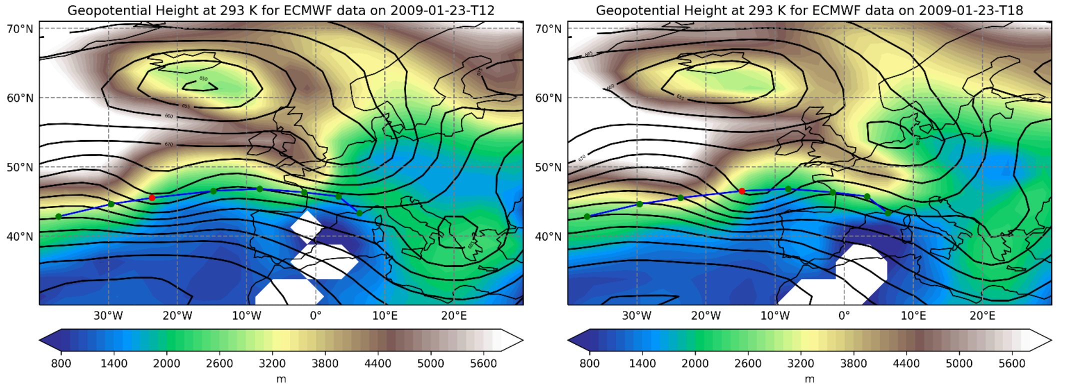
Geopotential Height at 293 K for ECMWF data on 2009-01-23-T12
Geopotential Height at 293 K for ECMWF data on 2009-01-23-T18
70°N
60°N
50°N
40°N
30°W
20°W
10°W
0°
10°E
20°E
800
1400
2000
2600
3200
3800
4400
5000
5600
m

(c) 01-23 T12 293 K (d) 01-23 T18 293 K

**Figure C.5.:** Geopotential height at a 293 K isentropic surface, six-hourly interval ECMWF data used. The blue line indicates the surface track of Storm Klaus for the time period between 0000UTC 23 January 2009 and 18UTC 24 January 2009. The position of the storm is marked with red dots. The green dots indicate the storm path (Coordinates taken from Liberato et al. (2011)).

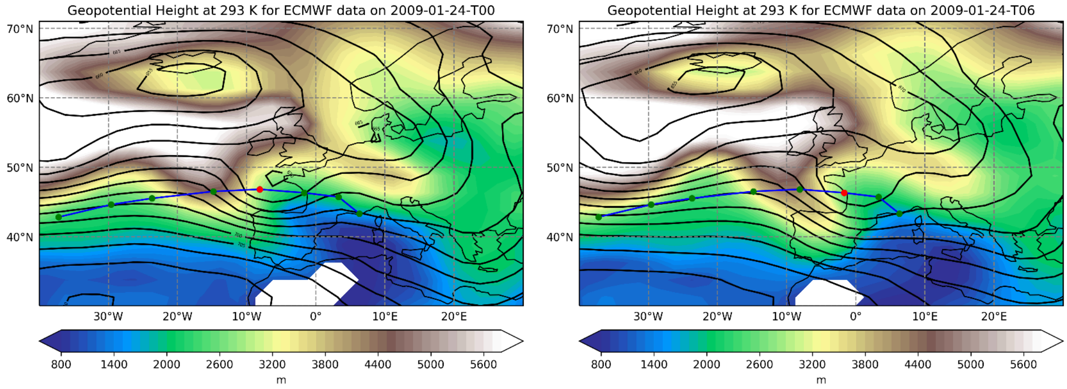
Geopotential Height at 293 K for ECMWF data on 2009-01-24-T00
Geopotential Height at 293 K for ECMWF data on 2009-01-24-T06
70°N
60°N
50°N
40°N
30°W
20°W
10°W
0°
10°E
20°E
800
1400
2000
2600
3200
3800
4400
5000
5600
m

(a) 01-24 T00 293 K

(b) 01-24 T06 293 K

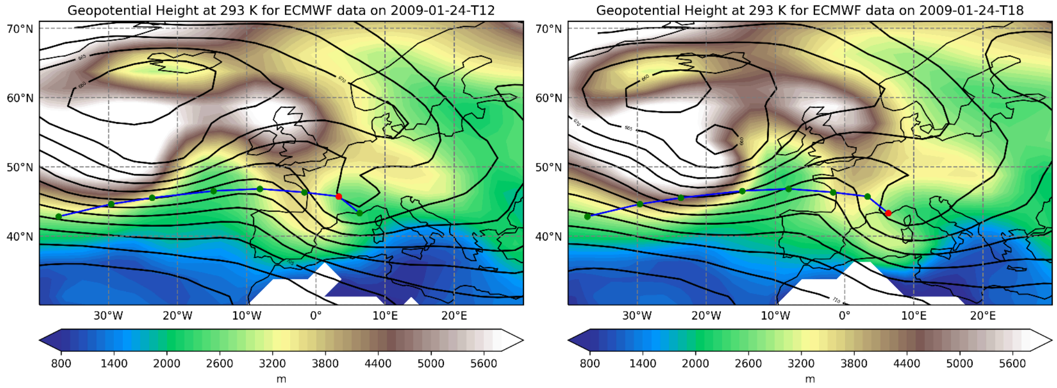
Geopotential Height at 293 K for ECMWF data on 2009-01-24-T12
Geopotential Height at 293 K for ECMWF data on 2009-01-24-T18
70°N
60°N
50°N
40°N
30°W
20°W
10°W
0°
10°E
20°E
800
1400
2000
2600
3200
3800
4400
5000
5600
m

(c) 01-24 T12 293 K

(d) 01-24 T18 293 K

**Figure C.6.:** Same as Fig. C.5, but for the following day

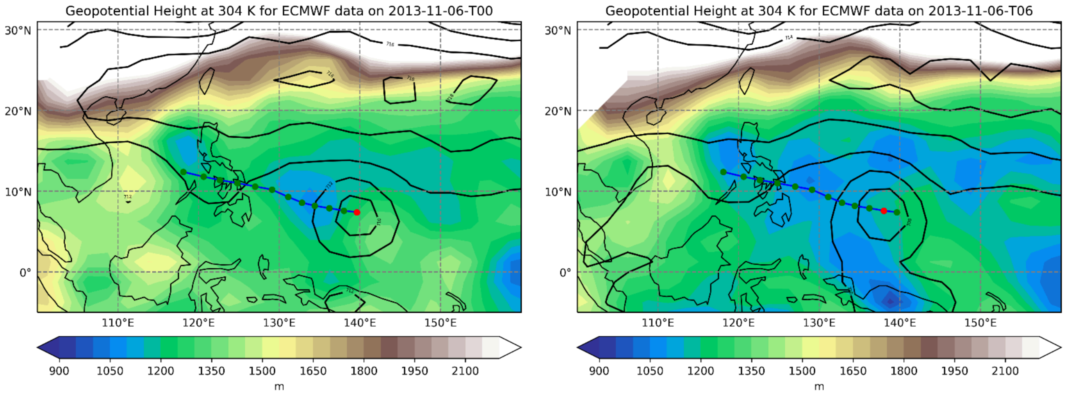
Geopotential Height at 304 K for ECMWF data on 2013-11-06-T00
Geopotential Height at 304 K for ECMWF data on 2013-11-06-T06
30°N
20°N
10°N
0°
110°E
120°E
130°E
140°E
150°E
900
1050
1200
1350
1500
1650
1800
1950
2100
m

(a) 11-06 T00 304 K

(b) 11-06 T06 304 K

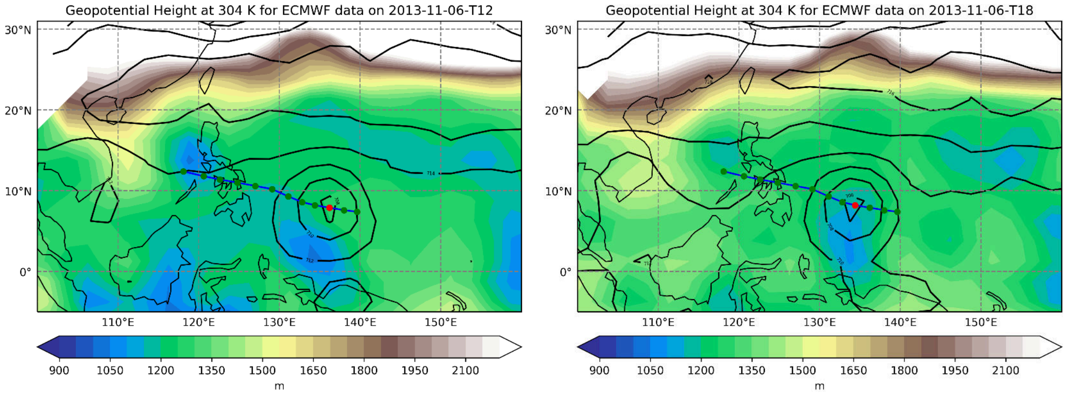
Geopotential Height at 304 K for ECMWF data on 2013-11-06-T12
Geopotential Height at 304 K for ECMWF data on 2013-11-06-T18
30°N
20°N
10°N
0°
110°E
120°E
130°E
140°E
150°E
900
1050
1200
1350
1500
1650
1800
1950
2100
m

(c) 11-06 T12 304 K

(d) 11-06 T18 304 K

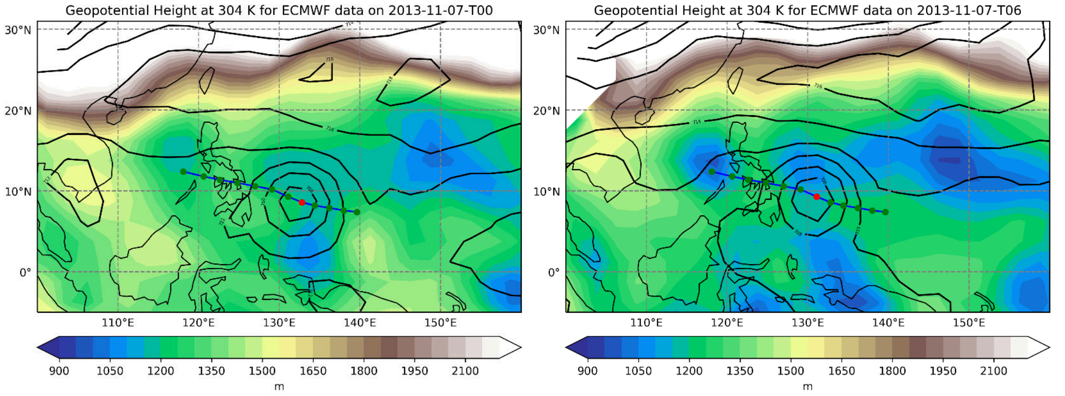
Geopotential Height at 304 K for ECMWF data on 2013-11-07-T00
Geopotential Height at 304 K for ECMWF data on 2013-11-07-T06
30°N
20°N
10°N
0°
110°E
120°E
130°E
140°E
150°E
900
1050
1200
1350
1500
1650
1800
1950
2100
m

(e) 11-07 T00 304 K

(f) 11-07 T06 304 K

**Figure C.7.:** Geopotential height at a 304 K isentropic surface for ECMWF data. The blue line indicates the surface track of the typhoon Haiyan for the time period between 0000UTC 06 November 2013 and 1800UTC 08 November 2013 (bottom). The position of the storm is marked withred dots. The green dots indicates the storm path (retrieved from the hurricane and tropical cyclones archive www.wunderground.com/hurricane/hurrarchive.asp, last visit on Sep 21, 2018).

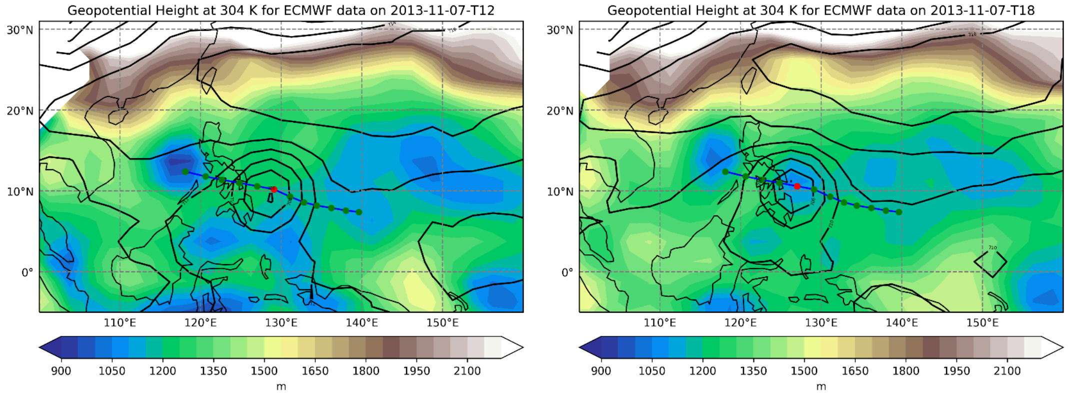
Geopotential Height at 304 K for ECMWF data on 2013-11-07-T12

Geopotential Height at 304 K for ECMWF data on 2013-11-07-T18

30°N
20°N
10°N
0°
110°E
120°E
130°E
140°E
150°E
900
1050
1200
1350
1500
1650
1800
1950
2100
m

(a) 11-07 T12 304 K (b) 11-07 T18 304 K

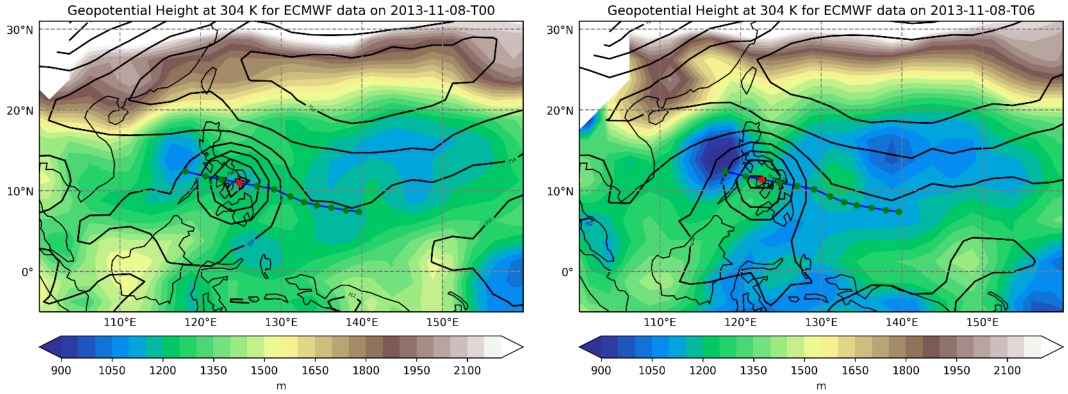
Geopotential Height at 304 K for ECMWF data on 2013-11-08-T00

Geopotential Height at 304 K for ECMWF data on 2013-11-08-T06

30°N
20°N
10°N
0°
110°E
120°E
130°E
140°E
150°E
900
1050
1200
1350
1500
1650
1800
1950
2100
m

(c) 11-08 T00 304 K (d) 11-08 T06 304 K

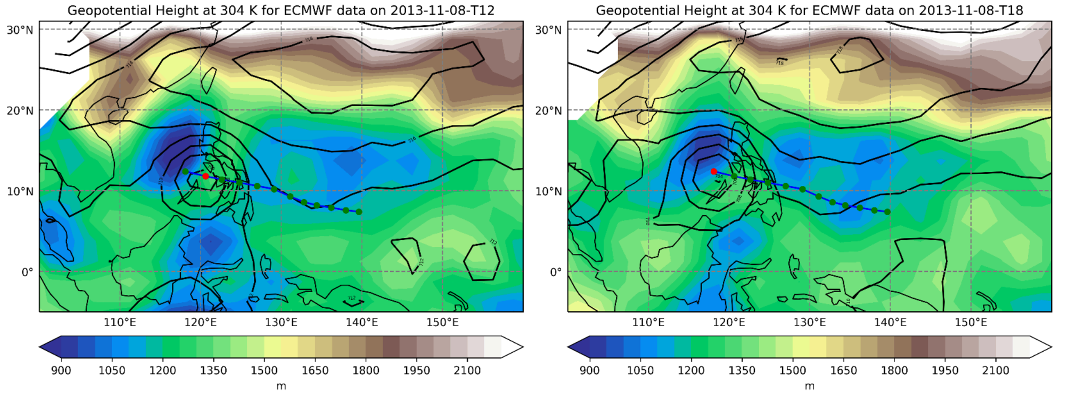
Geopotential Height at 304 K for ECMWF data on 2013-11-08-T12

Geopotential Height at 304 K for ECMWF data on 2013-11-08-T18

30°N
20°N
10°N
0°
110°E
120°E
130°E
140°E
150°E
900
1050
1200
1350
1500
1650
1800
1950
2100
m

(e) 11-08 T12 304 K (f) 11-08 T18 304 K

**Figure C.8.:** Same as Fig. C.7, but for the following day.

*Abstract:*

Temperature changes in the Arctic region are crucial for the Earth's climate system. They affect the temperature gradient between the Equator and the Arctic region and subsequently influence the cyclone paths in the middle latitudes. This has a strong impact on the weather conditions in Europe and North America and could lead to more extreme weather events across the northern hemisphere.

To investigate these temperature changes and their consequences, Equator-to-pole temperature gradients as well as temperature differences and trends between the tropical area and the Arctic region are evaluated. In addition, two exemplary storm cases are explored. All results are based on atmospheric profiles from GPS Radio Occultation observations from 2001 to 2017. Atmospheric analyses and reanalyses are used for comparison. The high vertical resolution of the RO data offers a great advantage, as it allows the representation of vertical resolved trends from the troposphere up to the mid stratosphere. In the lower troposphere, the temperature difference between the tropics and the Arctic decreases up to −0.5 K per decade, while it increases above by up to 1 K per decade near 12 km altitude. In the lower stratosphere the temperature difference decreases up to −0.4 K per decade at about 25 km.

With the current RO satellite constellations, it is found challenging to detect storm paths of small, fast moving storm systems. However, for large storm systems requiring less spatial-temporal resolution, the precise vertical geolocation with RO can provide additional information on the storm track on isentropic surfaces.

*Zum Inhalt:*

Temperaturänderungen in der Arktis sind für das Klimasystem der Erde von entscheidender Bedeutung. Sie beeinflussen den Temperaturunterschied zwischen der Arktis und dem Äquator und haben in weiterer Folge auch einen Einfluss auf die Stürme in mittleren Breiten. Eine Veränderung der Sturmbahnen wiederum kann Auswirkungen auf das Klima in Europa und Nordamerika haben und zu Wetterextremen in der Nordhemisphäre führen.

Um diese Temperaturänderungen und ihre Folgen besser beurteilen zu können, werden sowohl Temperaturgradienten vom Äquator zu den Polen als auch die Temperaturunterschiede und Trends zwischen der tropischen und der arktischen Region genauer untersucht. Weiters werden zwei Sturmereignisse explizit betrachtet. Alle Ergebnisse basieren auf atmosphärischen Profilen von GPS Radio Okkultationsbeobachtungen zwischen 2001 und 2017. Zum Vergleich werden atmosphärische Analysen und Reanalysen verwendet. Die hohe vertikale Auflösung der Radio Okkultationsdaten ist von großem Vorteil, da sie die Darstellung vertikal aufgelöster Trends von der Troposphäre bis zur mittleren Stratosphäre ermöglicht. In der unteren Troposphäre nimmt der Temperaturunterschied zwischen den Tropen und der Arktis um bis zu −0.5 K pro Dekade ab, während er in der Nähe von 12 km bis zu 1 K pro Dekade ansteigt. In der unteren Stratosphäre bei etwa 25 km Höhe nimmt die Temperaturdifferenz mit ungefähr −0.4 K pro Dekade ab.

Mit den derzeitigen RO-Satellitenkonstellationen ist es schwierig, Sturmbahnen von kleinen, sich schnell bewegenden Sturmsystemen zu erkennen. Bei großen Sturmsystemen, die eine geringere zeitliche und räumliche Auflösung erfordern, kann die genaue vertikale Geolokalisierung mit RO zusätzliche Informationen über den Sturmverlauf auf isentropischen Oberflächen liefern.

Wegener Center for Climate and Global Change
University of Graz
Brandhofgasse 5
A-8010 Graz, Austria
www.wegcenter.at
ISBN 978-3-9504717-1-7